SIMULATION OF DETECTOR PHYSICS PROCESSES IN RESISTIVE PLATE CHAMBERS

THESIS

SUBMITTED FOR THE AWARD OF THE DEGREE OF

Doctor of Philosophy

IN

PHYSICS

BY

MOHAMMED SALIM M

Supervisor

Prof. Rashid Hasan

Co-supervisor

Dr. B. Satyanarayana

DEPARTMENT OF PHYSICS
ALIGARH MUSLIM UNIVERSITY
ALIGARH-202002 (INDIA)

2014

CERTIFICATE

This is to certify that the work presented in the PhD thesis entitled **"Simulation of Detector Physics Processes in Resistive Plate Chambers"** submitted by **Mr. Mohammed Salim M** has been carried out and completed under our supervision. This work is an original contribution to the existing knowledge of the subject.

Prof. Rashid Hasan
(Supervisor)
Department of Physics
Aligarh Muslim University
Aligarh (UP) -202002

Dr. B. Satyanarayana
(Co-Supervisor)
Scientific Officer (G)
Department of High Energy Physics
Tata Institute of Fundamental Research
Mumbai- 400005

ACKNOWLEDGMENTS

First of all, I am highly grateful to the Almighty God for giving me blessings and courage to complete my research work. I must offer my profoundest gratitude and deep respect to my supervisor, Prof. Rashid Hasan for his patience, motivation, enthusiasm and immense knowledge. He has been a source of encouragement and inspiration throughout my life.

I would like to express my special appreciation and sincere thanks to my co-supervisor, Dr. B. Satyanarayana, you have been a tremendous mentor for me. He has always made himself available to clarify my doubts despite his busy schedules and I take this opportunity to record my sincere thanks for his valuable guidance and consistent encouragement that I received throughout my research work.

The thesis would not have come to a successful completion, without the help I received from our collaborators, Prof. S. Mukhopadhayay and Prof. Nayana Majumdar of the Saha Institute of Nuclear Physics, Kolkata. They have given their valuable time, advice, criticism and correction to the thesis from the beginning up to the end of the writings. I express my deepest thanks to them. I also thank Prof. Sudeb Bhattacharya of SINP.

I thank Prof. Rahimullah Khan, Chairman of our department, for the academic support and the facilities provided for me to carry out research work at department of physics, AMU.

My sincere thanks also goes to Prof. Naba. K. Mondal, TIFR, Mumbai, for offering me the opportunities to work in the INO detector lab at TIFR and guiding me to work on the fascinating world of detectors.

Completion of this thesis was possible with the support of several people, who have been very kind enough to extend their help during various phases of my research whenever I approach them and I would like to acknowledge them all. I thank Prof. Gobinda Majumdar, EHEP, TIFR, for his valuable comments and suggestions. I also thank Prof. L. M. Pant, BARC, who taught us the course on detector physics. I thankfully remember Prof. Amol Dighe, TIFR for teaching us the course

on Neutrino physics.

I thank my fellow lab-mates at TIFR. Special mention goes to Piyush Verma, Nagaraj Panyam, Ravindra Shinde, Manas Bhuyan, Shekhar Lahamge, Mandar Saraf, Asmita Redij, Deepak Samuel, Sudeshna Dasgupta, Ravindra Karanam, Sumanta Pal, Darshana Koli. I owe a lot to my INO colleagues and graduate students, who helped during various stages of my research. Furthermore, I have to offer my special thanks to my colleagues at SINP, Kolkata, especially, Abhik Jash and Purba Bhattacharya.

I wish to express my sincere thanks to many experts in the field, like Prof. Paulo Fonte, Prof. Werner Riegler, Prof. Horst Wenninger, Dr. Crispin Williams, Prof. Stephen Biagi, Prof. Rob Veenhof and Dr. Stefan Guindon, interactions with them through email and during various Conferences and Workshops was very helpful in completing my research work.

I am grateful to my friends, Sasi devan, Rishad, Rajiv, Rafi Alam, Jane Alam, Abdul Salih, Shafeeq Rahman Thottoli, Abdussalam, Haris Kunari, Nisar, Aslam and Haseeb for their good support and help.

Finally, I am deeply indebted to my parents and family for their constant help and prayers. My heartfelt thanks goes to my wife, Jasla, whose love and encouragement helped me to achieve my goal.

Salim

Mohammed Salim M

SIMULATION OF DETECTOR PHYSICS PROCESSES IN RESISTIVE PLATE CHAMBERS

ABSTRACT
OF THE
THESIS
SUBMITTED FOR THE AWARD OF THE DEGREE OF
Doctor of Philosophy
IN
PHYSICS
BY
MOHAMMED ASALIM M

Supervisor
Prof. Rashid Hasan

Co-supervisor
Dr. B. Satyanarayana

DEPARTMENT OF PHYSICS
ALIGARH MUSLIM UNIVERSITY
ALIGARH-202002 (INDIA)

2014

SIMULATION OF DETECTOR PHYSICS PROCESSES IN RESISTIVE PLATE CHAMBERS

SUBMITTED FOR THE AWARD OF THE DEGREE OF

DOCTOR OF PHILOSOPHY

IN

PHYSICS

BY

MOHAMMED SALIM M

Supervisor

Prof. Nasim Akhtar

Co-Supervisor

Dr. B. Bhatnagar

DEPARTMENT OF PHYSICS
ALIGARH MUSLIM UNIVERSITY
ALIGARH-202002 (INDIA)

2014

ABSTRACT

Ever since the existence of neutrino was first postulated by Pauli in 1930 to explain the continuous electron energy distribution in the nuclear beta decay, many neutrino experiments have been conducted world wide using different sources and detectors to explain the various properties of this tiny, electrically neutral, weakly interacting truly fundamental particle called *neutrino*. All flavors of neutrinos were discovered in different experiments in the course of time. Among these experiments, India's contribution to the neutrino physics was also historic. The first atmospheric neutrino was detected in the Kolar Gold Field (KGF) in India in 1965. The recent results from many neutrino experiments like Super-kamiokande in Japan, SNO etc throw light into the fact that neutrinos not only have mass, but also undergo flavor mixing *oscillations*, this is a clear evidence for the physics beyond the Standard Model. The efforts of the Indian physicists in the neutrino physics are still continuing through the Mega-Science project, India-based Neutrino Observatory (INO). INO is a multi-institutional collaboration which will build an underground laboratory at Pottipuram in Bodi West hills of Theni District of Tamil Nadu. The INO project aims to study the properties of atmospheric neutrinos using a 50 kiloton magnetized iron Calorimeter (ICAL) detector in its first phase of operation. The detector will also act as a far detector for neutrino factory beam in the future long-baseline experiment. The ICAL detector can distinguish between neutrino and anti-neutrino events. This is possible by applying uniform magnetic field of 1–1.4 Tesla on the iron layers of detector that allowing for charge discrimination of muons. The iron layers will be sandwiched with the active detector elements called Resistive Plate Chambers (RPC). ICAL will use 28,800 glass Resistive Plate Chambers (RPCs) of 2 m X 2 m in size to be operated in the avalanche mode. The thesis discusses the experimental and simulation studies of ICAL RPCs.

Resistive Plate Chambers (RPCs) are gaseous parallel plate detectors with excellent spatial and time resolutions. RPCs were first developed by R. Santanico and R. Cardarelli and are based on the same principle of spark chamber developed by Pestov and Fedotovich. These detectors have been successfully used in many particle physics experiments for trigger and TOF applications. The main features of this detectors are that they are cheaper, easy to fabricate and give very good

spatial and time resolution. Recent developments report that timing resolution of RPCs for minimum ionizing particles (MIPs) came down to 50 ps. An RPC consists of two parallel plate electrodes with high bulk resistivity of about 10^{12} Ωcm which are usually made of glass or Bakelite (phenol formaldehyde resin). The back surface of the plates are coated with a suitable semi-conductive coating like graphite having resistivity of the order 10^6 $\Omega/\Box$. A gas gap is maintained in between parallel electrodes to produce primary ionization clusters and proper gas gain. The charge signal from the RPC depends on the gas gap. Spacers are placed to keep the uniformity of the gas gap throughout the volume of the detector otherwise due to electrostatic attraction the electrode plates may come close together. The signal readout is taken from both X and Y pick-up panels which are placed orthogonal to each other on either side of the gas gap. The metallic strips of the pick-up panels are separated from the graphite coating by thin insulating layers.

An incoming charged particle that passes through the detector gas gap will transform some or all of its energy to the gas molecules in the active volume. The particle interaction, with various physics processes happening inside the the gas gap, creates both positive and negative charged particles. The high voltage applied on the resistive plates causes an electric field to develop in the RPC. Under the influence of electric field, accelerated charged particle undergo secondary ionization by colliding with the nearby gas molecules. This process continues and the avalanche developed proceeds towards the corresponding electrodes. This process induce signals on both the x and y pick-up strips. Finally this electric signal from the detector is processed and stored.

RPC can be operated either in avalanche mode or streamer mode. In avalanche mode operation of an RPC, the gas amplification is decreased by a reduced electric field across the gas gap. By suitable selection of gas mixtures the avalanche growth can be controlled. The electron attachment and photon absorption are the two processes by which avalanche signal reduction occurs in an RPC. In streamer mode of operation, the electric filed inside the gas gap is intense enough to generate localized discharges. Larger signals are observed in streamer mode. This mode of operation is suitable for low rate applications like cosmic ray experiments.

RPCs used for triggering muon detector system are termed as Trigger RPCs. The single/double gap RPCs with gas gap 2 mm and operating voltage around 10 kV are used for triggering. They give very good detection efficiency (around 98%) and time resolution (around 1 ns). RPCs with multi-gap configurations with gas

and time resolution (around 1 ns). RPCs with multi-gap configurations with gas gap 0.2 to 0.3 mm are used in TOF applications. They work in avalanche mode and give around 99% efficiency and very good time resolution, below 50 ps.

ICAL RPCs are 2 mm gap trigger RPCs operated in avalanche mode and use a gas mixture, Freon ($C_2H_2F_4$/R-134a), isobutane (iso-C_4H_{10}) and Sulfur hexaflouride (SF_6) normally in the proportion 95.2/4.5/0.3.

Different factors are considered while selecting a proper RPC gas mixture. They include high gas gain, high rate capability, low working voltage and good proportionality. Working mode of the RPC i.e either avalanche or streamer mode is selected by the gas mixture. In streamer mode operation, usually a mixture of isobutane (iso-C_4H_{10}), Freon ($C_2H_2F_4$/R-134a) and Argon is used. While in avalanche mode, $C_2H_2F_4$, isobutane and Sulfur hexaflouride (SF_6) gas mixture is used. Freon has high electron affinity and reduces the streamer size from spreading transversely due to electron capture. Freon gas is safe, inflammable and non-ozone depleting. It has high density i.e high primary ionization and low operating voltage. But the global warming potential of Freon is 1300 times greater than CO_2 gas. Also it produces radicals like HF that damages the electrode surface. Isobutane prevents a secondary streamer by absorbing efficiently UV photons emitted by the de-excited molecules. Argon provides high charge multiplication. Even very small concentration of highly electronegative SF_6 reduces the charge signal by capturing electrons. A sophisticated gas mixing and distribution system has been developed for INO ICAL RPCs having four input gases. This gas system utilizes Mass Flow Controllers (MFCs) for properly mixing the input gases in the desired proportions. The gas is distributed to the all the 12 RPCs in a prototype detector stack which is used to conduct the experiments discussed in the thesis.

We have performed simulation studies of the Resistive Plate Chamber (RPC) in detail in the thesis. Simulation is a very essential tool to optimize the detector design and to calibrate the performance of the detector. The RPC simulation involves the interaction of the particle in the sensitive gas medium of the detector, numerical calculation of electric field of the RPC configuration, Monte Carlo simulation of electron transport parameters and the simulation of signal development on the RPC pick-up electrodes. In order to carry out simulation for these processes, we have used various simulation tools. We used simulation packages like HEED and Geant4 for calculating primary ionization. The nearly exact Boundary Element Method (neBEM) and COMSOL Multiphysics (A commercial Finite

Element package) to find the electric field configuration and MAGBOLTZ for computing electron transport parameters. The thesis contains five chapters which are organized as follows,

Chapter 1 of the thesis begins with an introduction of neutrinos, standard model of particle physics, neutrinos beyond standard model and neutrino oscillations. After this, we briefly discuss different neutrino experiments and also recent results from these experiments. We then discuss the India-based Neutrino (INO) experiment and the various physics goals of INO with ICAL detector.

In Chapter 2, we discuss mainly the interactions of particle with matter, particle detectors and specifically about Resistive Plate Chamber (RPC). We also discuss different modes of operation of RPCs, application of RPCs as trigger and timing RPCs. We end this chapter by summarizing different RPCs used in the past and on-going experiments.

The Chapter 3 is devoted mainly to the RPC development and instrumentation. This chapter discusses the different procedure that we have adopted in the fabrication of RPCs, the prototype detector stack where we have performed our experiment, electronics and data acquisition system and the gas mixing and distribution system. Then we discuss the detailed experimental setup and the results of the experiment obtained for various RPC gas mixtures.

The chapter 4 of the thesis deals with the RPC simulation. In this chapter we discuss the different simulation tools which we used to make the simulation framework for the RPC. We begin with a brief discussion on primary ionization, energy loss of a minimum ionizing particle and the simulation with HEED package. Then we also carry out simulation of primary ionization in the RPC using Geant4 package. Here we compare the simulation results with both HEED and Geant4. After this, we discuss the different methods for solving electric field configuration of the Resistive Plate Chamber. In this part, we mainly focus on the Finite Element Method (FEM) and the nearly exact Boundary Element Method (neBEM). Then we compare the electric field calculated with neBEM and COMSOL Multyphysics. We also calculate the electron transport parameters with MAGBOLTZ.

The Chapter 5 of the thesis contains the comparison of experimental results with the simulation data for various RPC parameters such as timing, efficiency and charge spectra. In this chapter we discuss in detail about the possibilities of

improving the simulation results by considering various factors and also including the circuit simulation to complete the simulation framework as our future plan.

CONTENTS

LIST OF FIGURES

LIST OF TABLES

CHAPTER 1

INO AND NEUTRINO PHYSICS

1.1 Introduction

The main motivation of particle physics experiments is to study and understand the secret behind the fundamental interactions, particles and symmetries of nature. The particle detectors help us to track the new particles which are produced by the collision/decay of some other particles in the laboratories or in the upper atmosphere (cosmic rays). The four fundamental interactions and their properties are given in Table. 1.1. A particle may not necessarily be subject to all the four interactions. Neutrinos, for example, experience only the weak interaction. Particles are classified according to their spin as fermions and bosons. Fermions obey the Fermi-Dirac statistics and have half-integer spin whereas bosons obey the Bose-Einstein statistics and have integer spin. Particles can also be classified according to their interactions as leptons and hadrons. The leptons are the particles which interact via the weak interactions and hadrons are those particles which interact mainly via the strong nuclear interaction. The elementary particles are classified as shown in Fig. 1.1. Neutrinos are special among the leptons since they are electrically neutral and interact through the weak interactions only.

Table 1.1: The Fundamental Interactions

Interaction	Relative Strength	Range	Mediating Particle
Strong	1	10^{-15} m	Gluons
Electromagnetic	10^{-2}	∞	Photons
Weak	10^{-6}	10^{-18} m	W^+,W^-, Z bosons
Gravitation	10^{-43}	∞	Graviton

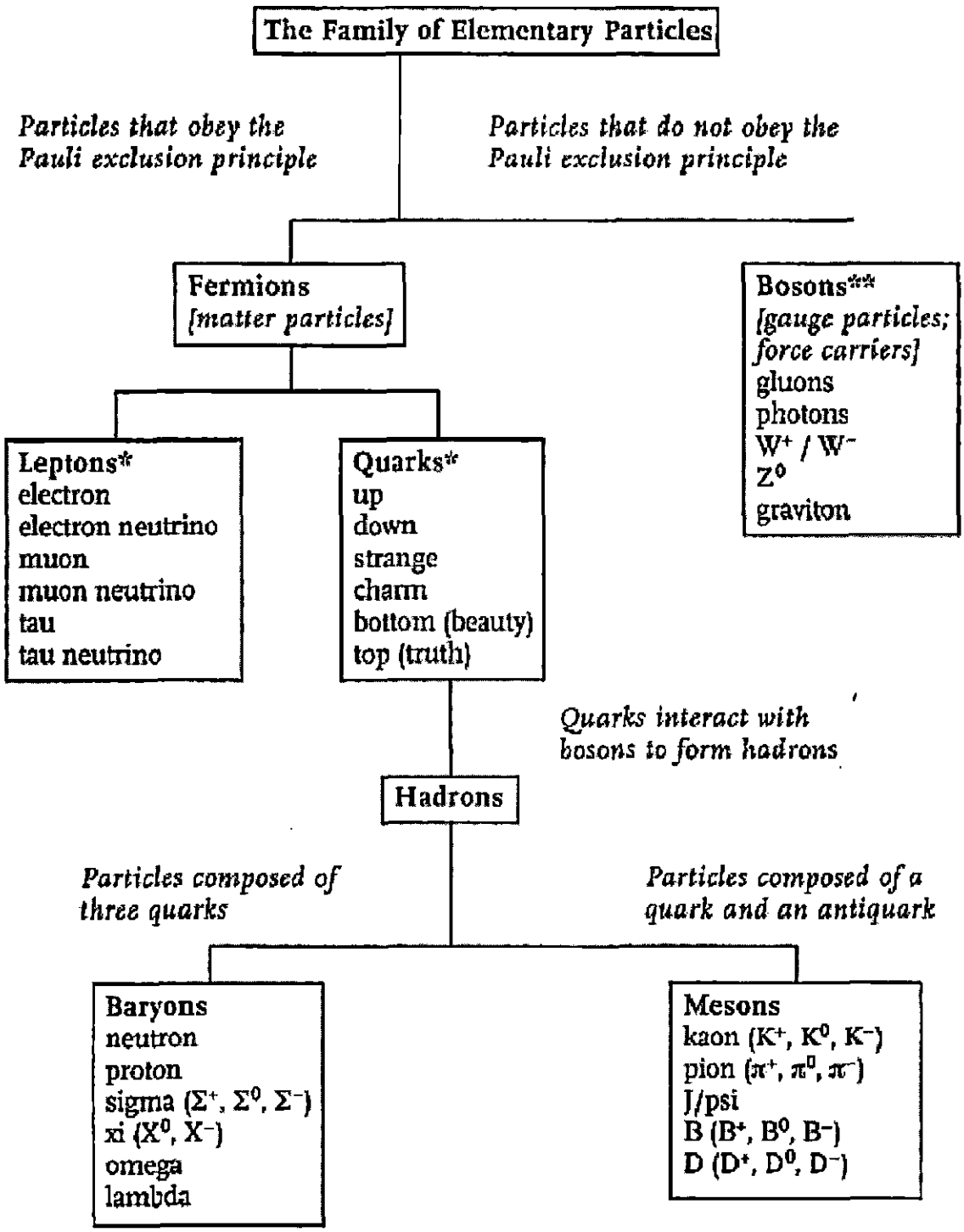

Figure 1.1: Classification of elementary Particles

1.2 Brief History of Neutrino

In 1930, Wolfgang Pauli proposed a hypothetical unseen, neutral particle that could be responsible for the energy-momentum conservation in certain radioactive decays. Later in 1931, Fermi named this particle as neutrino in his famous theory of beta decay [1]. The first experimental observation of neutrinos was by Reines and Cowan [2, 3] in 1956. They used two tanks of water with a total mass of 200 kg with 40 kg of $CdCl_2$. The tanks were sand-wiched between three layers of scintillators. The positrons produced from the reaction

$$\bar{\nu}_e + p \longrightarrow n + e^+ \tag{1.1}$$

annihilated with electrons in the scintillation counters giving two 0.5 MeV photons. The neutrons were absorbed by $CdCl_2$ dissolved in water which released photons. The coincidence of these two kinds of photons confirmed the above reaction, and hence the presence of $\bar{\nu}_e$. The muon neutrino was discovered at Brookhaven National Laboratory in 1962 [4] and the first detection of the tau neutrino was in 2000 by the DONUT collaboration at Fermilab [5]. Neutrinos are the second most abundant particles in the universe and come from several sources. Geo-neutrinos come from the earth's crust, solar neutrinos from the sun, reactor neutrinos as byproducts of nuclear reactors, supernovae neutrinos from stellar collapse and atmospheric neutrinos from the cosmic rays. Neutrinos provide information about the earth's interior, supernovae core and they are the best particles for probing the astrophysical sources because they are barely attenuated by the interstellar medium during their travel.

1.3 Standard Model Neutrino

In the Standard Model, the elementary particles i.e. six quarks and six leptons are grouped into three families or generations (Fig. 1.2). This theory explains the four fundamental interactions of these fundamental particles in terms of the Quantum Field Theory. The members of the first (lightest) generation, up (u) and down (d) quarks form the nucleons which along with the electrons make up the normal matter. The muon and tau are the particles in the second and third generations, analogous to the electron in the first generation. Corresponding to these particles and their antiparticles, there are three flavors of neutrinos (ν_e, ν_μ, ν_τ) and their antiparticles ($\bar{\nu}_e, \bar{\nu}_\mu, \bar{\nu}_\tau$).

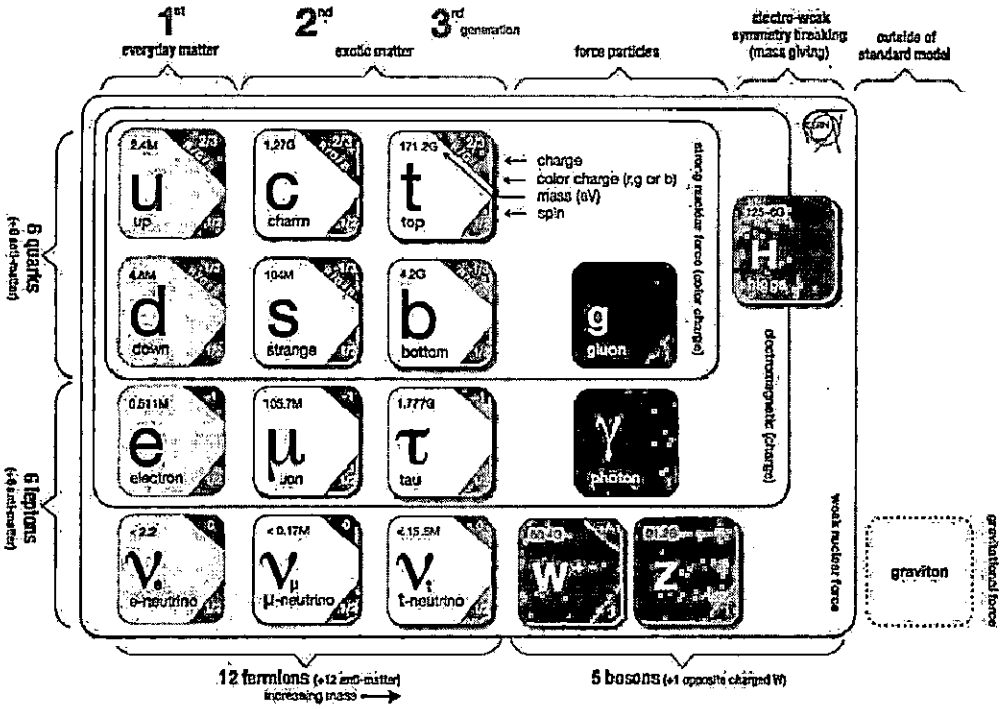

Figure 1.2: Standard Model

In the Standard Model,

- The three flavors of neutrinos are massless.
- Neutrinos and anti-neutrinos are distinct.
- All neutrinos have left handed helicity and all anti-neutrinos have right handed helicity.

1.4 Neutrinos beyond Standard Model

1.4.0.1 Solar Neutrino Problem

Solar neutrinos were first detected in 1970 at Homestake Solar Neutrino Experiment in the Homestake Gold Mine in South Dakota. It is the first experiment that found that there was a discrepancy between the predicted and measured neutrino flux coming from the sun. Solar energy production is due to the thermonuclear fusion of hydrogen into helium that takes place inside Sun's core. The thermonuclear

processes are mainly two chain reactions, so called *pp chain* and *CNO cycle.* All these nuclear processes lead to the production of electron neutrinos, ν_e but mostly by pp chain and a small fraction through CNO cycle (Figs. 1.3(a) and 1.3(b)).

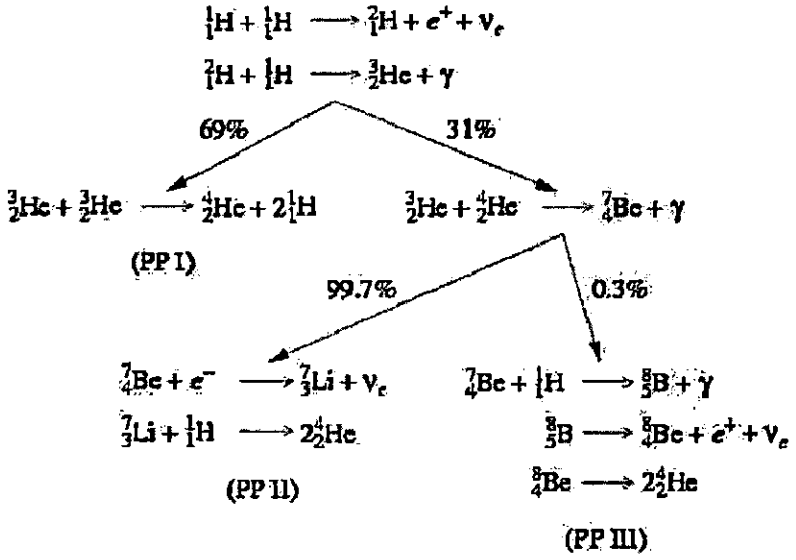

(a) pp chain

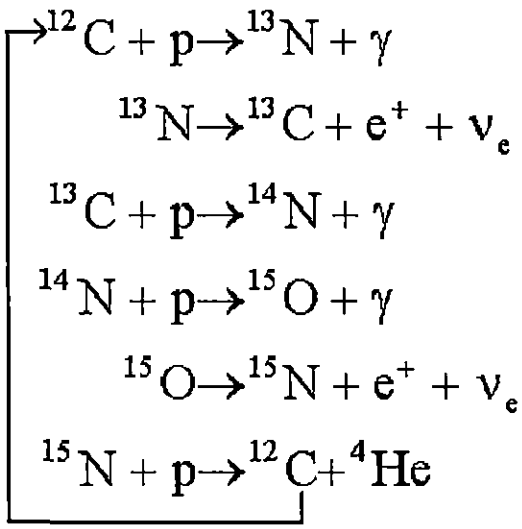

(b) CNO cycle

Figure 1.3: Thermonuclear fusion reactions (a) pp chain and (b) CNO cycle

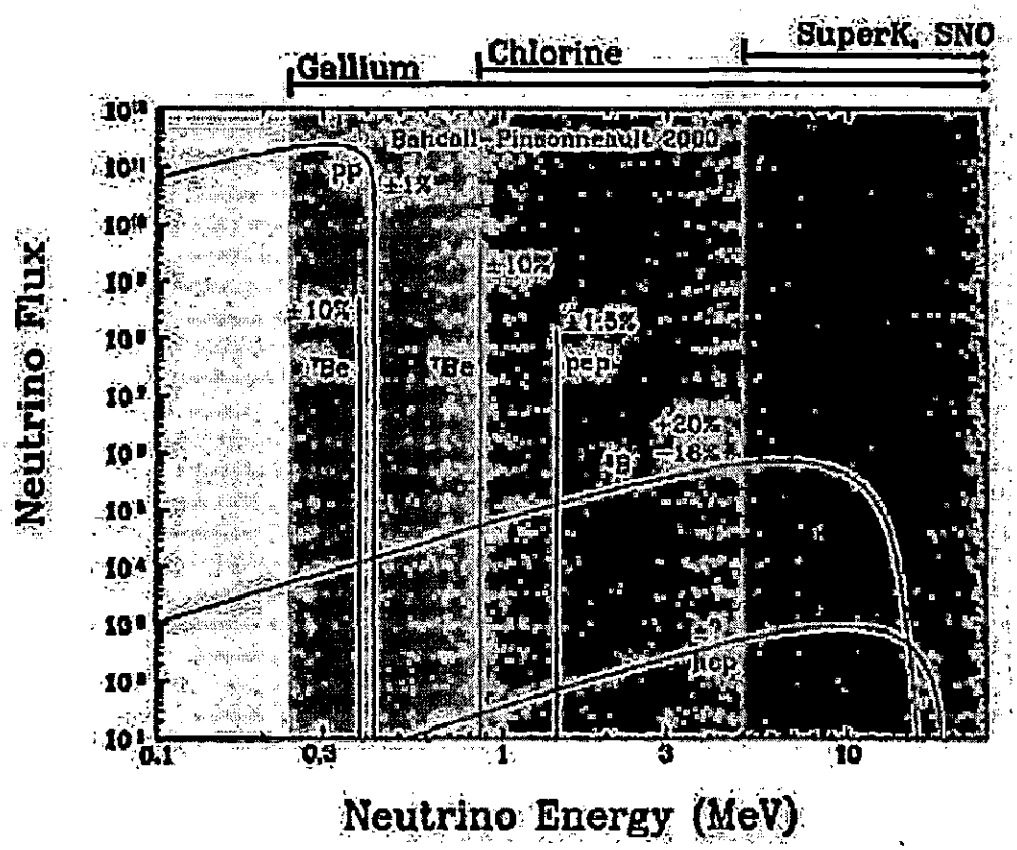

Figure 1.4: The solar neutrino fluxes predicted in the SSM

The neutrino energy spectrum from the pp chain of interactions in the Sun, as predicted by the standard solar model is shown Fig. 1.4. The neutrinos emitted in different steps of the pp cycle are classified as pp, pep, ^7Be, ^8B and hep neutrinos, according to the respective production reaction. The different solar neutrino experiments are sensitive to different neutrino energy ranges. The Gallium solar Neutrino Observatory detectors are sensitive mainly to pp-neutrinos and a small contribution from ^7Be, ^8B and pep neutrinos. In this experiment, Gallium is used to absorb ν_e and radioactive ^{71}Ge nuclei produced in the reaction,

$$^{71}Ga + \nu_e \longrightarrow ^{71} Ge + e^- \tag{1.2}$$

are counted which give the total flux of ν_e with a threshold 233 keV from the sun. The Homestake experiment used chlorine to absorb ν_e through the reaction,

$$^{37}Cl + \nu_e \longrightarrow ^{37} Ar + e^- \tag{1.3}$$

The threshold energy of the neutrinos in this reaction is 814 keV. The Superkamiokande and the Sudbury Neutrino Observatory (SNO) detector are most sensitive to electron neutrinos coming from the ^8B reaction. The solar neutrino experiments like

Kamiokande, GALLEX, SAGE ,GNO and SNO observed that the ν_e flux from the sun is only one third of the prediction by the Standard Solar Model [6,7]. The reason for the missing neutrino flux may be the electron type neutrinos (ν_e) produced in the solar core are turning into the other flavors with some probability on their journey to the earth.

1.4.0.2 Atmospheric Neutrino Problem

Atmospheric neutrinos are produced by the decay of particles produced as a result of collisions of cosmic rays with nuclei in the atmosphere. The interaction of cosmic rays, which are mostly protons, with other nuclei in the atmosphere produces hadron shower consisting mainly pions. The pions decay into muons and muon neutrinos,

$$\pi^{\pm} \longrightarrow \mu^{\pm} + \nu_{\mu}(\bar{\nu_{\mu}}) \tag{1.4}$$

The muon then decays into electrons, muon neutrinos and electron neutrinos.

$$\mu^{\pm} \longrightarrow e^{\pm} + \nu_{e}(\bar{\nu_{e}}) + \bar{\nu_{\mu}}(\nu_{\mu}) \tag{1.5}$$

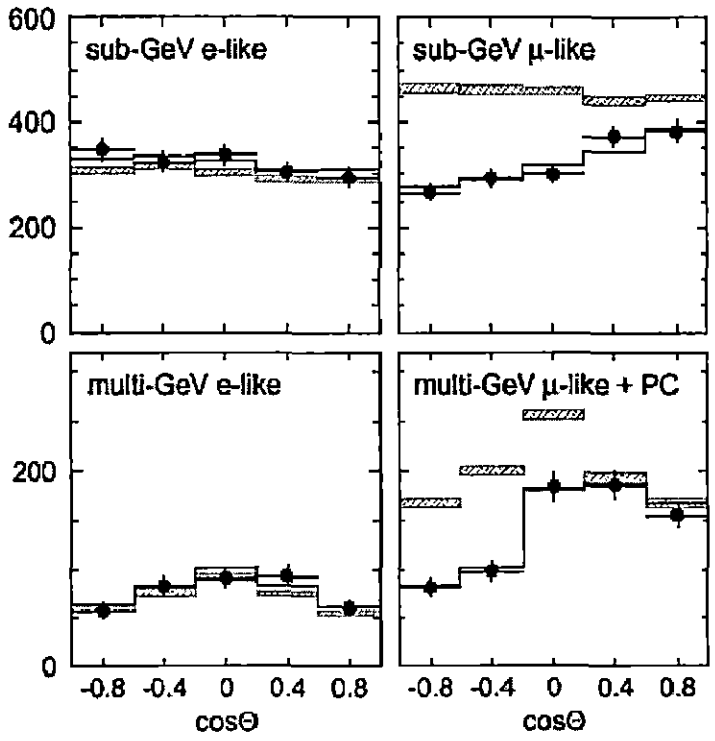

Figure 1.5: Angular distributions for e-like (left) and μ-like (right) events, for sub-GeV (top) and multi-GeV (bottom) neutrinos. Here the blue histograms show the Monte Carlo predictions [8].

The zenith-angle distributions observed in the Super-Kamiokande water Cherenkov detector for various data samples are given in Fig. 1.5. Negative cosΘ corresponds to the up-going neutrino events and positive cosΘ represents the down-going neutrino events. There is a strong up-down asymmetry for μ-like events with the zenith angle. The sub-GeV μ-like events are less than expected and the difference with Monte Carlo predicted events is larger for negative cosΘ, i.e. the upcoming events. Whereas the μ-like multi-GeV events match with the expected rate for the down-going events and but a large difference is observed for the upcoming neutrinos. There is no asymmetry observed in e-like events. The up-coming muon neutrinos have to travel a large distance through the earth compared with the down-going neutrinos. This could be the reason for the up-down asymmetry. The observation also give the idea that the electron neutrinos are not affected. *Neutrino Oscillations* give explanation to this phenomenon and according to this theory the muon type neutrinos traveling through the matter converts to tau neutrinos (ν_τ).

1.4.1 Neutrino Oscillations

Neutrino Oscillation or flavor transition is a quantum mechanical phenomenon. The flavor states are related to the mass eigen sates by a unitary mixing matrix called MNS mixing matrix [9],

$$|\nu_\alpha\rangle = \sum_j U^*_{\alpha j} |\nu_j\rangle \tag{1.6}$$

where ν_α = (ν_e, ν_μ, ν_τ) are the flavor states and ν_j =(ν_1, ν_2, ν_3) are the mass eigen states. The unitarity of mixing matrix, $U^\dagger U = 1$ implies that mass eigen states and flavor states are orthonormal i.e. $\langle \nu_j \,|\, \nu_k \rangle = \delta_{jk}$ and $\langle \nu_\alpha \,|\, \nu_\beta \rangle = \delta_{\alpha\beta}$.

Neutrino Oscillations in Vacuum

Neutrinos are produced as flavor particles in charged current weak interactions and are propagated as massive particles. The flavor states are the quantum superposition of wave functions as given in eqn. (1.6) and the mass eigen states can be expressed in terms of flavor states.

$$|\nu_j\rangle = \sum_\alpha U_{\alpha j} |\nu_\alpha\rangle \tag{1.7}$$

The mass eigen states propagate in space-time as plane waves. Then according to Schrodinger equation,

$$|\nu_j(t,x)\rangle = e^{-iE_j t + ip_j x} |\nu_j\rangle \tag{1.8}$$

Now let us consider the space-time evolution of the flavor state $|\nu_\alpha\rangle$ from eqns. (1.6) and (1.8),

$$|\nu_\alpha(t,x)\rangle = \sum_j U^*_{\alpha j} e^{-iE_j t + ip_j x} |\nu_j\rangle \tag{1.9}$$

From eqn (1.7) the above equation can be written as,

$$|\nu_\alpha(t,x)\rangle = \sum_{\beta=e,\mu,\tau} \left(\sum_j U^*_{\alpha j} e^{-iE_j t + ip_j x} U_{\beta j} \right) |\nu_\beta\rangle \tag{1.10}$$

The amplitude of transition from one flavor to another is,

$$A_{\alpha\beta}(t,x) = \langle \nu_\beta \,|\, \nu_\alpha(t,x)\rangle = \sum_j U^*_{\alpha j} e^{-iE_j t + ip_j x} U_{\beta j} \tag{1.11}$$

The probability of flavor transition is the modulus square of the transition amplitude,

$$P_{\alpha\beta}(t,x) = |A_{\alpha\beta}(t,x)|^2 = |\sum_j U^*_{\alpha j} e^{-iE_j t + ip_j x} U_{\beta j}|^2 \tag{1.12}$$

It is very difficult to measure the time t but the source to detector distance L can be measured very accurately in experiments. For the ultra relativistic neutrinos we can take an approximation $t \approx x = L$ in natural units. Now we can write, $E_j t - p_j x \approx (E_j - p_j)L = \frac{E_j^2 - p_j^2}{E_j + p_j} L \approx \frac{m_j^2}{2E} L$ and by putting this term in eqn. (1.12) we will get the probability in terms of the source to detector distance L and neutrino energy E [10]

$$P_{\alpha\beta}(L,E) = \sum_{j,k} U^*_{\alpha j} U_{\beta j} U_{\alpha k} U^*_{\beta k} exp\left(-i \frac{\Delta m^2_{jk} L}{2E} \right) \tag{1.13}$$

where $\Delta m^2_{jk} = m^2_j - m^2_k$ is the mass-squared difference.

Two-flavor mixing

For a two flavor neutrino oscillation the MNS mixing matrix can be simplified as,

$$U = \begin{pmatrix} \cos\theta & \sin\theta \\ -\sin\theta & \cos\theta \end{pmatrix} \tag{1.14}$$

The time evolution of flavor eigen state ν_α is,

$$|\nu_\alpha(t)\rangle = \cos\theta\,|\nu_1(t)\rangle + \sin\theta\,|\nu_2(t)\rangle = \cos\theta e^{\frac{-im_1^2 t}{2E}} |\nu_1(0)\rangle + \sin\theta e^{\frac{-im_2^2 t}{2E}} |\nu_2(0)\rangle \tag{1.15}$$

Now following eqn. (1.13) the *survival probability* of the neutrino flavor eigen state in vacuum can be derived as,

$$P_{\alpha\alpha} = |\langle \nu_\alpha \,|\, \nu_\alpha(t) \rangle|^2 = 1 - \sin^2\theta \sin^2\left(\frac{\Delta m^2 L}{4E}\right) \tag{1.16}$$

The transition probability of the flavor state α in to the flavor state β is then,

$$P_{\alpha\beta} = \sin^2\theta \sin^2\left(\frac{\Delta m^2 L}{4E}\right) \tag{1.17}$$

where $\Delta m^2 = m_2^2 - m_1^2$. Either of the mass eigen states must be non-zero for oscillations to occur. Angle θ is the mixing angle. If $\theta = 0$, no oscillations occur and the flavor states are identical to the mass states. When $\theta = \pi/4$ the oscillations are maximal. L/E is the ratio between source to detector distance and the neutrino energy called *baseline* which is fixed in an experiment. The zenith-angle distributions observed in the Super-Kamiokande shown in Fig. 1.5, can be explained by the neutrino oscillations. The upcoming muon neutrinos have to travel around 1000 km by crossing the earth from one side to another whereas the down-going neutrinos travel only 10 km in the atmosphere before reaching the detector situated in the earth. The observations from Fig. 1.5 are

1. The predicted and observed fluxes for both Sub-GeV and Multi-GeV e-like neutrino fluxes match well. This is because electron neutrino does not participate in the atmospheric neutrino oscillation.

2. There is a significant deviation in both the predicted and the observed flux for both Sub-GeV and Multi-GeV μ-like events. The down-going Sub-GeV muon neutrinos can oscillate in the atmosphere and convert to ν_τ and the oscillation is more for the up-coming neutrinos. The down-going Multi-GeV muon neutrinos cannot oscillate in the atmosphere but the up-coming Multi-GeV muon neutrinos travel a large distance through the earth and change their flavor into tau neutrinos.

Three-flavor mixing

The MNS transformation matrix in terms of three mixing angles and one phase can be written as,

$$U = \begin{pmatrix} c_{13}c_{12} & c_{13}s_{12} & s_{13}e^{-i\delta} \\ -c_{23}s_{12} - s_{13}c_{12}s_{23}e^{+i\delta} & c_{23}c_{12} - s_{13}s_{12}s_{23}e^{+i\delta} & c_{13}s_{23} \\ s_{23}s_{12} - s_{13}c_{12}c_{23}e^{+i\delta} & -s_{23}c_{12} - s_{13}s_{12}c_{23}e^{+i\delta} & c_{13}c_{23} \end{pmatrix} \tag{1.18}$$

where $s_{ij} = \sin\theta_{ij}$, $c_{ij} = \cos\theta_{ij}$ and δ is the Dirac phase. The oscillation probability from a neutrino eigen state ν_α to flavor eigen sate ν_β in the case of three flavor

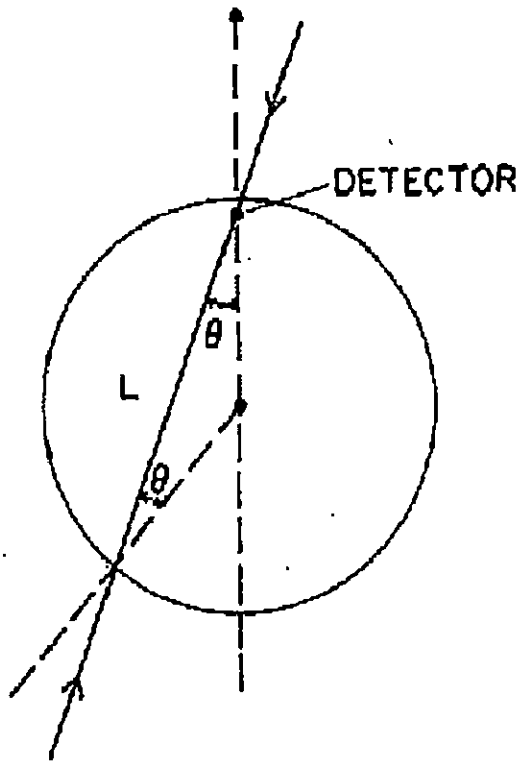

Figure 1.6: Upcoming and down-going atmospheric neutrinos through the earth

neutrino mixing can be given by,

$$P_{\alpha\beta} = \delta_{\alpha\beta} - 4\sum_{i>j} Re\left(U^*_{\alpha i}U_{\beta i}U_{\alpha j}U^*_{\beta j}\right)\sin^2\left(\frac{\Delta m^2_{ij}L}{4E}\right) + 2Im\left(U^*_{\alpha i}U_{\beta i}U_{\alpha j}U^*_{\beta j}\right)\cos\left(\frac{\Delta m^2_{ij}L}{2E}\right) \quad (1.19)$$

where the imaginary term corresponds to CP violation. There are six neutrino oscillation parameters. They are three angles (θ_{12},θ_{13}, θ_{23}), one CP-violating phase (δ) and two mass-squared differences (Δm^2_{21}, Δm^2_{32}). Among these Δm^2_{21} ($(\Delta m^2)_{sol}$), θ_{12} and θ_{13} are solar neutrino parameters and Δm^2_{32} ($(\Delta m^2)_{atm}$), θ_{23} and θ_{13} are atmospheric neutrino parameters. Neutrino oscillation experiments cannot measure the absolute masses but they can give only the mass-squared differences. We can

arrange the mass difference in two possible orders. If the sign of $(\Delta m^2)_{atm}$ is positive then $m_1 \ll m_2 \ll m_3$ and is called *normal hierarchy*. If the sign of $(\Delta m^2)_{atm}$ is negative then we arrange the masses in *inverted hierarchy* i.e. $m_3 \ll m_1 \simeq m_2$ (see Fig. 1.7).

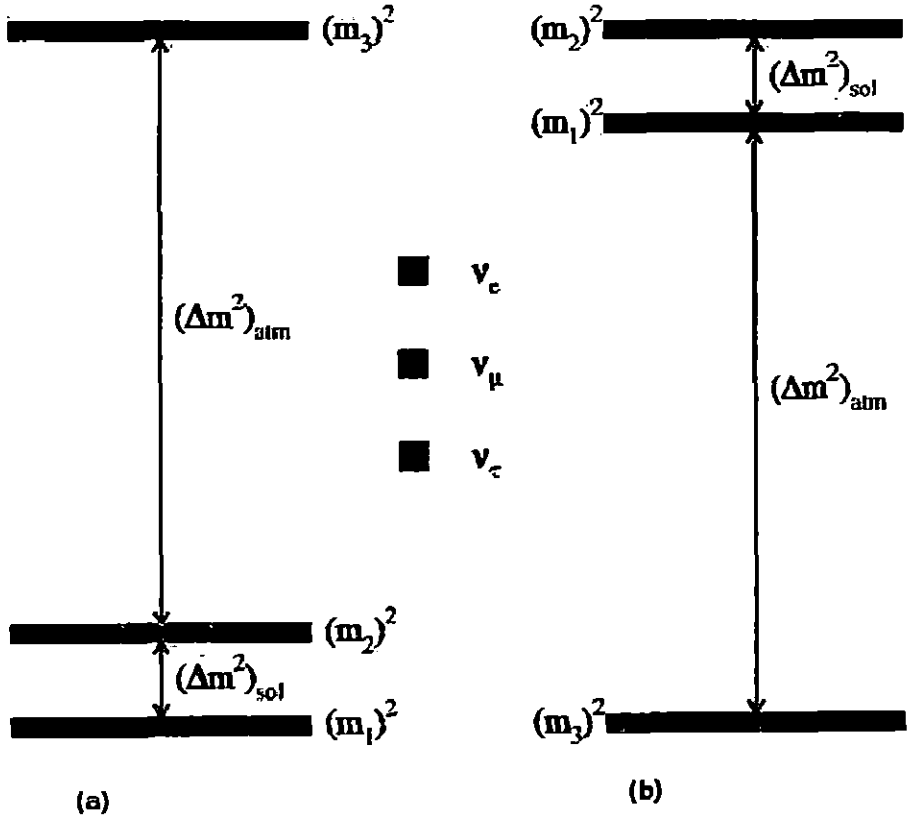

Figure 1.7: Neutrino mass hierarchy (a) normal ordering and (b) inverted ordering

1.4.2 Neutrino Oscillation Experiments

Neutrino oscillation experiments can be designed by selecting the baseline (L/E ratio) which are sensitive to different values of Δm^2. According to L/E ratio, neutrino oscillation experiments are divided into different categories,

- **Short BaseLine experiments (SBL):** Short BaseLine experiments (SBL) are classified into Reactor SBL and Accelerator SBL. Accelerator SBL is further divided into Pion Decay In Flight (DIF), Muon Decay At Rest (DAR) and Beam Dump. Reactor SBL experiments have a range $L/E \lesssim 10m/MeV$ with a sensitivity to $\Delta m^2 \gtrsim 0.1eV^2$. The SBL reactor experiments Day-Bay [11] and

RENO [12] have measured $\sin^2\theta_{13} \simeq 0.023 \pm 0.003$ and $\sin^2\theta_{13} \simeq 0.029 \pm 0.006$ respectively from the $\bar{\nu}_e$ disappearance experiment.

- **Long BaseLine experiments (LBL):** The source-detector distance in the Long BaseLine experiments (LBL) is around three times larger than the SBL experiments and are divided into the Reactor LBL and the Accelerator LBL experiments. The range of the Reactor LBL experiment, $L/E \lesssim 10^3 m/GeV$ and sensitivity to $\Delta m^2 \gtrsim 10^{-3} eV^2$. The Accelerator experiments have a range of $L/E \lesssim 10^3 km/GeV$ and sensitivity to $\Delta m^2 \gtrsim 10^{-3} eV^2$. The Double CHOOZ is a Reactor LBL experiment which calculated $\sin^2\theta_{13} \simeq 0.028 \pm 0.010$ [13].

- **Very Long BaseLine experiments (VLB):** The source to detector distance in the Reactor VLB experiments are of the order 100 km with a range of $L/E \lesssim 10^5 m/MeV$ and sensitivity to $\Delta m^2 \gtrsim 10^{-5} eV^2$. The Accelerator VLB experiments cover the range of $L/E \lesssim 10^4 km/GeV$ and sensitivity to $\Delta m^2 \gtrsim 10^{-4} eV^2$.

- **Solar neutrino experiments :** The Sun to earth distance is 1.5 X 10^{11} m and the energy of solar neutrinos comes in the range 0.2-15 MeV which is fixed by the nature. Then the range of $L/E \lesssim 10^{12} m/MeV$ and sensitivity to $\Delta m^2 \gtrsim 10^{-12} eV^2$.

- **Atmospheric neutrino experiments :** The up-coming atmospheric neutrinos have to cross the earth before reaching the detector on the other side of earth. Hence the source to detector distance is around 10^4 km and the energy of atmospheric neutrinos cover a range from around 500 MeV to 100 GeV. The range of $L/E \lesssim 10^4 km/GeV$ and sensitivity to $\Delta m^2 \gtrsim 10^{-4} eV^2$.

The recent updates of oscillation parameters are summarized in Table. 1.2 [14].

1.5 India-based Neutrino Observatory (INO) Experiment

Indian history of underground neutrino experiments dates back to 1960s. The first atmospheric neutrino was detected by a group of particle physicists from Tata Institute of Fundamental Research (India), Osaka City University (Japan) and Durham University (UK) in an underground laboratory in the Kolar Gold Fields (KGF) in India in 1965 at a depth of 2.3 km [15]. India-based Neutrino Observatory is an underground neutrino experiment [16] located in the Bodi West Hills in the Pottippuram Panchayat, Tamilnadu. INO will study the properties of the atmospheric neutrinos using a 50 kiloton magnetized Iron Calorimeter (ICAL) that can distinguish between neutrino and anti-neutrino events.

Table 1.2: Neutrino oscillation parameters summary. For Δm^2_{31}, $\sin^2\theta_{23}$, $\sin^2\theta_{13}$ and δ the upper (lower) row corresponds to normal (inverted) mass hierarchy [14]

parameter	best fit	1σ range	2σ range	3σ range
$\Delta m^2_{21}[10^{-5}eV^2]$	7.62	7.43-7.81	7.27-8.01	7.12-8.20
$\Delta m^2_{31}[10^{-3}eV^2]$	2.55	2.46-2.61	2.38-2.68	2.31-2.74
	2.43	2.37-2.50	2.29-2.58	2.21-2.64
$\sin^2\theta_{12}$	0.320	0.303-0.336	0.29-0.35	0.27-0.37
$\sin^2\theta_{23}$	0.613 (0.427)	0.400-0.461 and 0.573-0.635	0.38-0.66	0.36-0.68
	0.600	0.569-0.626	0.39-0.65	0.37-0.67
$\sin^2\theta_{13}$	0.0246	0.0218-0.0275	0.019-0.030	0.017-0.033
	0.0250	0.0223-0.0276	0.020-0.030	
δ	0.80π	$0\text{-}2\pi$	$0\text{-}2\pi$	$0\text{-}2\pi$
	0.80π			

1.5.0.1 Physics goals of INO

The major INO physics goals with magnetized Iron Calorimeter are listed [16] as follows:

- **Precise measurement of the oscillation parameters Δm^2_{32} and θ_{23}** by observing one full oscillation period with oscillation minima and maxima. The large range of L/E available for atmospheric neutrinos could help us to probe a wide range for Δm^2_{32}. Fig.1.8 gives the precision measurements to be achieved in the INO experiment compared with other running experiments.

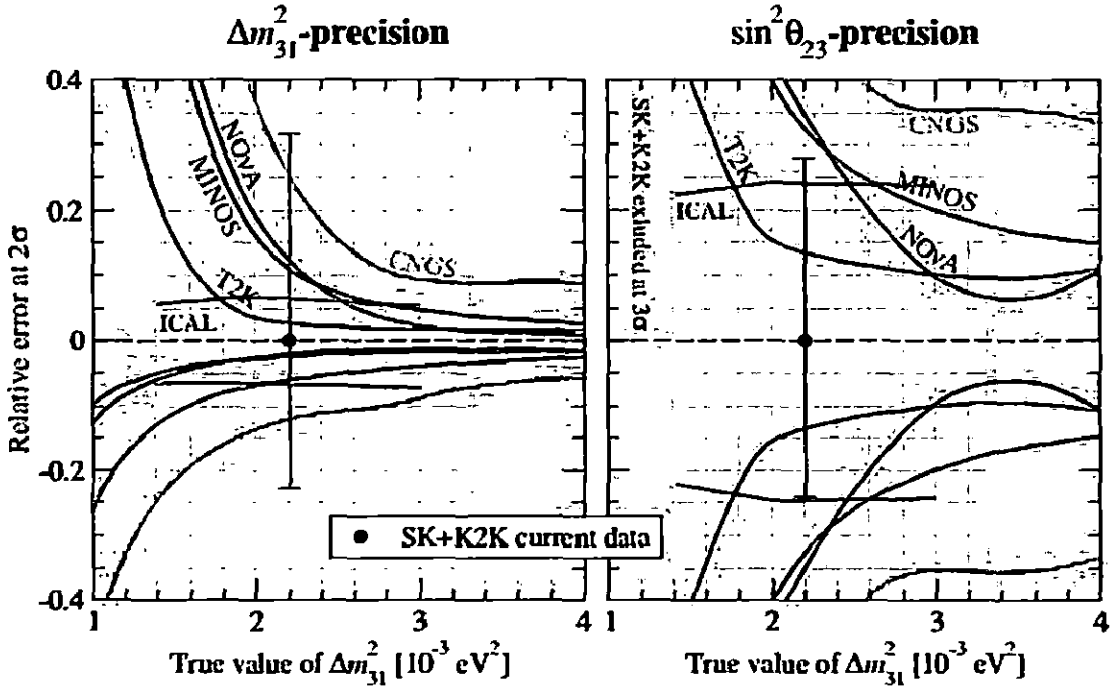

Figure 1.8: The relative error on Δm^2_{32} and $\sin^2\theta_{23}$ as a function of the input value of Δm^2_{32} at the 2σ level. 5 year exposure of ICAL detector have also been included [16].

- **Matter effects in μ^- and μ^+ events.** Charged events can be discriminated by the magnetized ICAL detector. This is possible by identifying the charge of muons produced by the interaction of neutrino and anti-neutrino with matter. The matter dependent effects are sensitive to the sign of Δm^2_{32} and the magnitude of θ_{13} [17,18].
- **Determination of mass hierarchy.** The sign of the mass-squared difference Δm^2_{32} involved in the atmospheric neutrino oscillations has to be determined. The mass ordering is direct if $\Delta m^2_{32}>0$ and inverted if $\Delta m^2_{32}<0$ (Fig.1.7). The

difference in the neutrino (ν_μ) and anti-neutrino ($\bar{\nu_\mu}$) up/down event ratio,

$$A = \frac{U}{D} - \frac{\bar{U}}{\bar{D}} \tag{1.20}$$

is different from each-other and also with the mass orderings due to matter effects [19]. Where $U(\bar{U})$ denotes the up-going events for neutrinos (anti-neutrinos) and $D(\bar{D})$ denotes the down-going events for neutrinos(anti-neutrinos) respectively.

- **Deviation from maximality of mixing angle θ_{23} and octant determination.** To determine whether the mixing angle θ_{23} is maximal (i.e., $\theta_{23} = \pi/4$), if not explored how well its octant can be determined.

- **Distinguishing $\nu_\mu \leftrightarrow \nu_\tau$ from $\nu_\mu \leftrightarrow \nu_s$.** The ICAL detector may determine whether the muon neutrino deficit observed by the previous experiments is due to the oscillations of the muon neutrinos to the tau neutrinos or to the sterile neutrinos.

- **CPT Violation.** The INO experiment would give the possibility of searching for CPT violation.

1.5.0.2 ICAL Detector

The ICAL detector will consist of three modules, each having a lateral size 16 m x 16 m and 14.5 m height. The total detector dimension will be 48.4 m x 16 m x 14.5 m. The detector will have 150 layers of magnetized iron plates of 5.6 cm thickness. A gap of 4 cm will be provided in between two iron plates to accommodate Resistive Plate Chambers (RPCs) which act as the active detector elements. Around 28800 large area RPCs of 2 m x 2 m dimension will be used in the ICAL detector which is huge in number. So RPCs are the better choice as active detectors since they are easy to fabricate and have low cost. The specifications of the ICAL detector and the RPCs are summarized in Table. 1.3 [20].

Table 1.3: ICAL detector and RPC parameters [20]

No. of modules	3
Module dimensions	16m x 16m x 14.5m
Detector dimensions	48.4m x 16m x 14.5m
No. of layers	150
Iron plate thickness	56mm
Gap for RPC layers	40mm
Magnetic field	1.3Tesla
RPC dimensions	1,950mm x 1,840mm x 24mm
Readout strip pitch	30mm
No. of RPcs/Road/Layer	8
No. of Roads/Layer/Module	8
No. of RPC units/Layer	192
No. of RPC units	28,800 (97, 505m^2)
No. of Readout strips	13,686,400

1.6 Summary

A brief description of the motivation for this doctoral work is given in this chapter. We organize subsequent chapters in the following way. The second chapter mainly deals with particle interactions with matter and various particle detectors, especially the Resistive Plate Chamber (RPC) in detail. Chapter 3 of the thesis is mainly devoted to the RPC development and instrumentation. It also discusses the experimental set-up for measuring the RPC parameters. The chapter 4 discusses the tools used for developing the simulation framework for the present doctoral work. Finally, in chapter 5 we compare the experimental results with the simulated results for various RPC parameters, charge spectra, efficiency and timing.

CHAPTER 2

RESISTIVE PLATE CHAMBERS (RPC)

The Resistive plate chambers (RPCs) are gaseous detectors based on the gas amplification in a small gas gap between two parallel plates which are kept under a high voltage of 9-10 kVs. The main features of this detector are that they are cheap, easy to fabricate and give very good spatial and time resolution. Recent results report that time resolution of the RPCs for minimum ionizing particles (MIPs) came down to 50 ps [21]. The various physics processes that happen inside an RPC when a high energy charged particle crosses the detector are explained in the following sections.

2.1 Particle Interactions with matter

The particles traveling through the material either gas, liquid or solid will have a certain probability to interact with the nuclei or with the electrons present in the material. The particles deposit their energy in matter through one of the following physics processes,

1. Charged particle interaction
2. Photon interaction
3. *Hadronic and Electromagnetic cascades*

2.1.1 Charged particle interaction

2.1.1.1 Energy loss by interaction with atomic electrons

When a charged particle traverses through matter, it loses energy mainly through collisions with electrons. Ionization is the process in which the charged particle

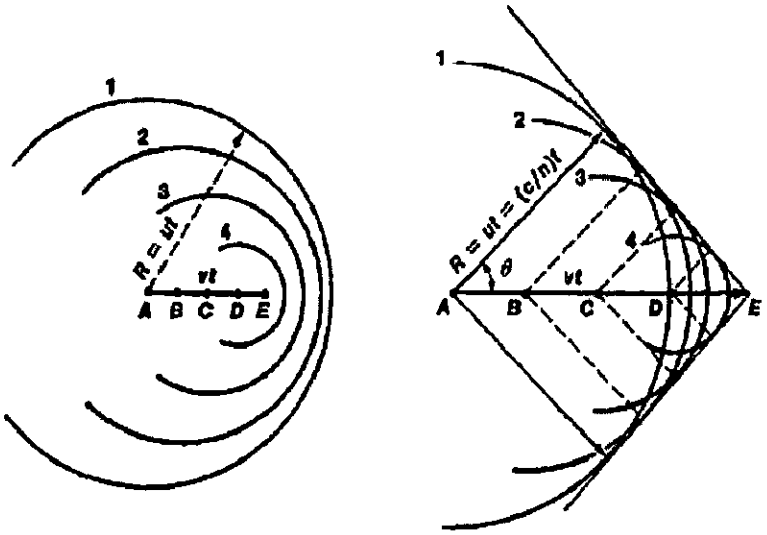

Figure 2.2: (Left)The motion of a charged particle in a medium at a velocity of v<u: the circles 1, 2, 3, and 4 represent the locations of the secondary waves emitted by the particle from points A, B, C, and D, respectively. (Right)The motion of a charged particle in a medium at a velocity of v>u: the angle indicates the direction of the emitted radiation

2.1.1.3 Bremsstrahlung Radiation

Radiative loss (Bremsstrahlung) occurs due to the deceleration of the charged particle in the coulomb field of a nucleus. Bremsstrahlung is the dominant energy loss process at high energies which is given by,

$$-\frac{dE}{dx} = 4\alpha N_A \frac{Z_{nucl}^2}{A} z^2 r^2 E ln \frac{183}{Z_{nucl}^{1/3}} \tag{2.5}$$

The average energy loss due to bremsstrahlung by an electron of Energy E, in a thickness of matter dx, is given by

$$\frac{dE}{dx} = -\frac{E}{X_0} \tag{2.6}$$

Where,

$$X_0 = \frac{A}{4\alpha N_A Z_{nucl}(Z_{nucl}+1) r_e^2 ln(183 Z_{nucl}^{-1/3})} \tag{2.7}$$

In the above equation X_0 represents the radiation length. This parameter is defined as the distance over which the electron energy is reduced by a factor 1/e due to the radiation loss only. The symbols used in equations 1.5 and 1.7 are defined as,
N_A is the Avogadro number

α is the fine structure constant ($\alpha = 1/137$) and
r_e is the classical electron radius
The energy where the losses due to the ionization and bremsstrahlung for electrons are the same is called critical energy (E_c)

$$\left.\frac{dE_c}{dx}\right|_{ion} = \left.\frac{dE_c}{dx}\right|_{brems} \tag{2.8}$$

For solid or liquid materials the critical energy can be given by,

$$E_c = \frac{610MeV}{(Z + 1.24)} \tag{2.9}$$

And for gases,

$$E_c = \frac{710MeV}{(Z + 0.92)} \tag{2.10}$$

2.1.1.4 Multiple Coulomb Scattering

Charged particles passing through the matter undergo repeated elastic scattering from the nuclei due to electromagnetic force. The changes in the direction of the particle along its trajectory is called direction straggling or multiple scattering. The cross section of this process is given by the Rutherford formula [23]

$$\frac{d\sigma}{d\Omega(\Theta)} = \frac{z^2 Z_{nucl}^2 r_e^2}{4}\left(\frac{m_e c}{\beta p}\right)^2 \frac{1}{sin^4(\Theta/2)} \tag{2.11}$$

According to the above relation, a particle with momentum p and velocity $v = \beta c$ undergoes a collision which deflects its trajectory into the solid angle $d\Omega$ at angle Θ to its original direction of motion. The Gaussian approximation can be taken for small angles of deviation. The root mean square (r.m.s) direction deviation of a particle traversing a thickness L of material is given by

$$\sqrt{\langle\Theta^2\rangle} = \frac{Z_{nucl}}{pc\beta}(20MeV)\sqrt{\frac{L}{X_0}} \tag{2.12}$$

Where X_0 is the radiation length.

2.1.2 Photon Interactions

2.1.2.1 Photoelectric effect

When the photon energy ($E_\gamma = \hbar\omega$) is greater than the binding energy $E_{binding}$(work function) of the electron in the material, photon is absorbed by the atom and an electron is emitted. The energy of the photo-electron is given by

$$E_{kinetic} = \hbar\omega - E_{binding} \tag{2.13}$$

The photoelectric effect is the dominant mode of interaction of gamma rays of energy less than 100 keV. The energy dependence of the cross section is approximately given by

$$\sigma \approx Const \frac{Z_{nucl}^{n}}{E_{\gamma}^{3.5}} \tag{2.14}$$

In the above equation the coefficient n varies between 4 and 5 over the energy of interest.

2.1.2.2 Compton scattering

The elastic scattering between a photon and an electron is called Compton scattering. Photon behaves like a particle with an energy $\hbar\omega$ in this process.

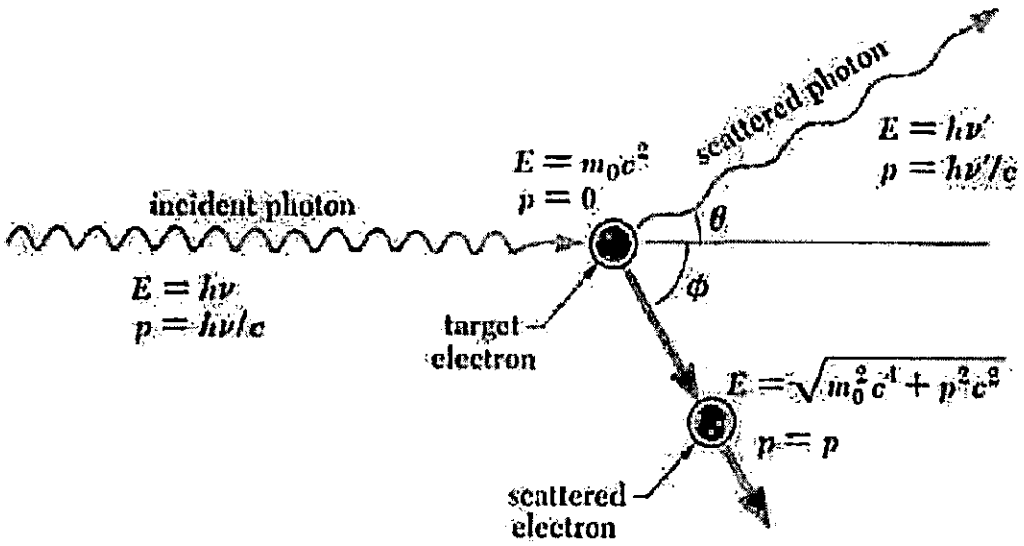

Figure 2.3: Kinematics of Compton scattering

The energy and the direction of the final state photon can be obtained from the energy and momentum conservation relation.

$$h\nu' = \frac{h\nu}{1 + \gamma(1 - cos\theta)} \tag{2.15}$$

$\gamma = h\nu/m_ec^2$ in the above equation. The cross section is given by Klein-Nishina formula [23]

$$\frac{d\sigma}{d\Omega} = \frac{r_e^2}{2} \frac{1}{[1 + \gamma(1 - cos\theta)]^2} \left(1 + cos^2\theta + \frac{\gamma^2(1 - cos\theta)^2}{1 + \gamma(1 - cos\theta)}\right) \tag{2.16}$$

2.1.2.3 Pair Production

The interaction of photon with the Coulomb field of a nucleus is called Pair Production. In this process, the energy of photon is utilized to create an electron-positron pair in the presence of a nucleus. The cross section for Pair Production at high energies is given by

$$\sigma = \frac{7}{9} 4\alpha r_e^2 Z_{nucl}(Z_{nucl}+1) ln\left(\frac{183}{3\sqrt{Z_{nucl}}}\right) \tag{2.17}$$

2.1.3 Hadronic and Electromagnetic Cascades

The interaction of high energy cosmic ray particles mostly protons with the atmospheric nuclei initiates hadronic cascades.

$$p + nucleus \longrightarrow \pi^+ + \pi^- + \pi^0 + ... + nucleus' \tag{2.18}$$

The decay of a neural pion gives two gamma rays,

$$\pi^0 \longrightarrow \gamma + \gamma \tag{2.19}$$

The high energy gamma rays initiate the production of an avalanche of electrons by pair production and the high energy electron (positron) emits gamma ray by Bremsstrahlung. This avalanche is known as electromagnetic cascade. These interactions are very important in the design of electromagnetic and hadronic calorimeters.

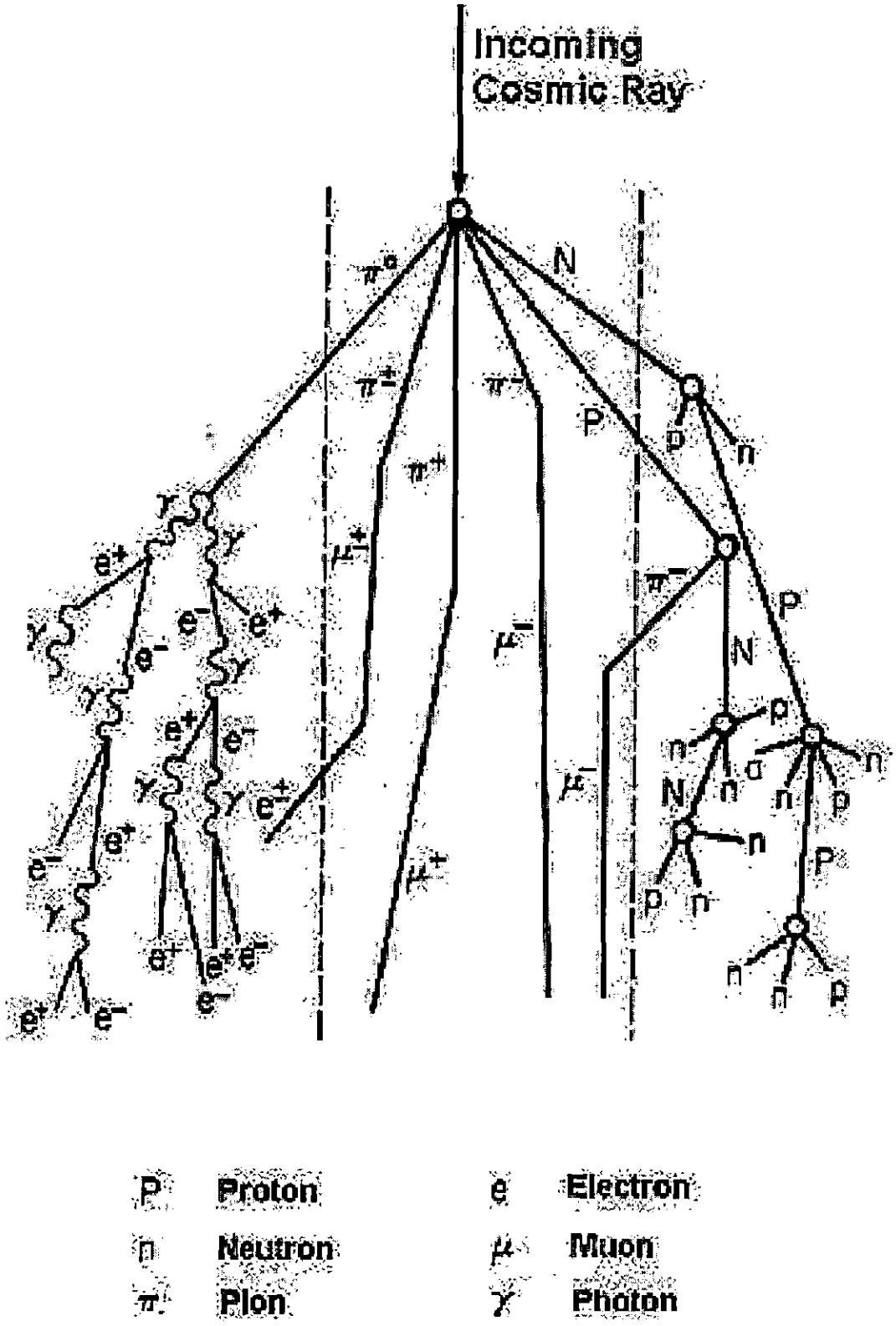

Figure 2.4: Schematic representation of hadronic and electromagnetic cascade

2.1.4 Neutrino Interactions

The interaction probability of neutrino with matter is very small. Neutrinos are neutral particles and also not sensitive to strong interactions. They interact only by the weak force.

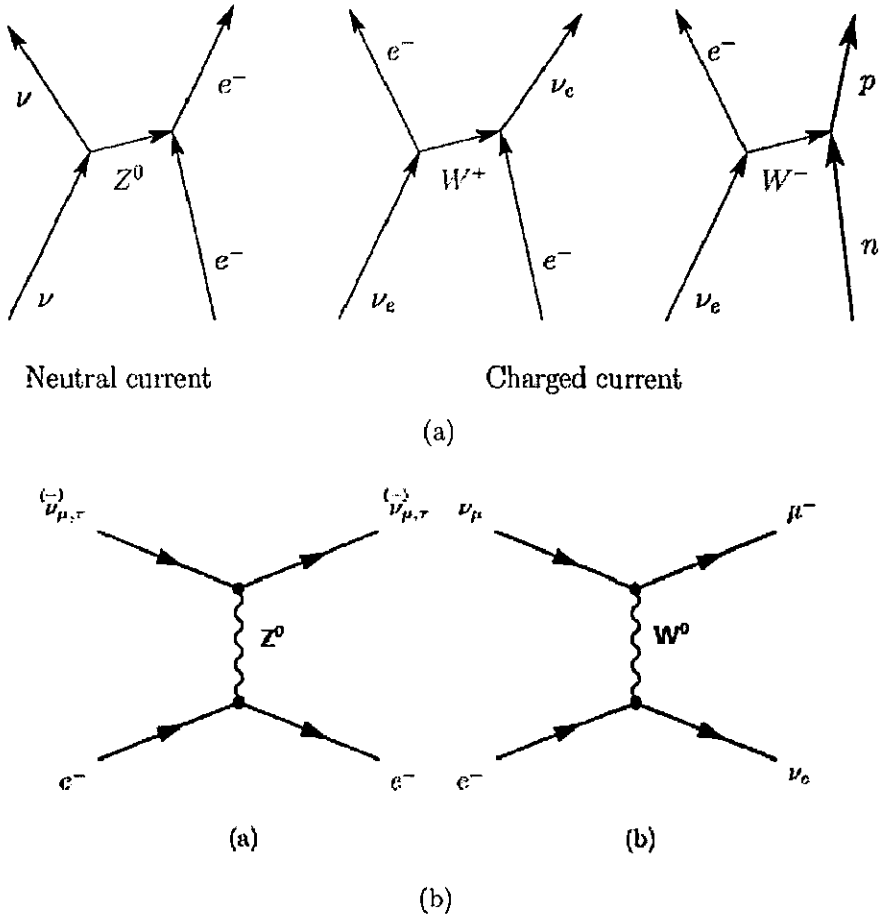

Figure 2.5: Neutrino interaction Feynman diagrams.

For electron neutrinos the elastic scattering with electrons can be mediated by the charged and neutral weak bosons ($W^{\pm}$ and Z^0) as shown in Fig. 2.5(a), whereas the scattering of muon and tau neutrinos from electrons is mediated only by the neutral bosons, as shown in Fig. 2.5(b).

2.2 Particle detection with RPC

The following detectors are used for the detection of charged and neutral particles like neutrinos, γ-rays and neutrinos.

- Gas detectors
- Semiconductor detectors
- Scintillation detectors
- Liquid detectors
- Cherenkov detectors
- Compton detectors
- Bolometers and Micro-calorimeters

In this section, we will discuss briefly about the working principle of gas detectors and Resistive Plate Chambers in detail.

2.2.1 Gas Detectors

A fast charged particle passing through a gaseous medium causes ionization and excitation of the gas molecules. The ionization process produces an electron and a positive ion in the medium. The primary electrons with sufficient kinetic energy interact with nearby gas molecules and produce secondary electrons and ion pairs. Let E_i be the ionization energy, W_i the average energy per ionization and n_p the average number of primary ionization per unit length. Then the total number of ion pairs n_t can be calculated by

$$n_t = \frac{dE}{dx}\frac{1}{W_i} \tag{2.20}$$

In this thesis, the primary ionization parameters like the average number of clusters of charge carriers per unit length and cluster size distribution are calculated by the HEED program [24].

2.2.1.1 Ionization Statistics

The probability of interaction of a particle traveling a distance between z and z + dz is $N\sigma dz$. Where N is the electron density and σ is the ionization cross section. Let P(z) be the probability of not having an interaction after a distance z. Now the probability of not having an interaction between z and z + dz is

$$P(z+dz) = P(z)(1 - N\sigma dz) \tag{2.21}$$

The average distance between two ionizing collisions is called mean free path (λ) which is given by

$$\lambda = \frac{\int zP(z)dz}{P(z)dz} = \frac{1}{N\sigma} \tag{2.22}$$

Table 2.1: The characteristics of some of the gases used in gaseous detectors [22].

Gas	Ionization potential (eV)	Mean energy of electron-ion pair, W_i (eV)	Energy loss (keV/cm)	Number of electron-ion pairs (cm^{-1})	Number of primary electrons(cm^{-1})
A_r	15.7	25	2.53	106	25
X_e	12.1	22	6.87	312	41
H_e	24.5	41.6	0.345	8.3	5
H_2	15.6	36.4	0.32	8.8	5.2
N_2	15.5	34.8	1.96	56.3	10
Air		33.8	2.02	59.8	
O_2	12.5	30.2	2.26	74.8	22
CH_4	12.6	30	1.61	54	37
C_2H_6	11.5	26	2.91	112	48
i-C_4H_{10}	10.6	26	5.67	220	90
CO_2	13.8	34	30103.35	100	35

The probability of the particle surviving a distance z is

$$P(z) = \exp^{\frac{-z}{\lambda}} \tag{2.23}$$

and the interaction probability

$$P_{int}(z) = 1 - P(z) = 1 - e^{\frac{-z}{\lambda}} \tag{2.24}$$

2.2.1.2 Diffusion and drift in Gases

Diffusion

Charge pairs (electrons and ions) produced by an ionizing particle diffuse uniformly outward from their point of creation in the absence of an electric field. The charge diffusion follows a Gaussian distribution,

$$\frac{dN}{dx} = \frac{N}{\sqrt{2\pi}\sigma_x} e^{\frac{-x^2}{2\sigma_x^2}} \tag{2.25}$$

$$\sigma_x = \sqrt{2Dt} \tag{2.26}$$

where D is the diffusion coefficient.

Drift

when an electric field is applied across a gas volume, the electrons and ions created by the ionization process accelerate towards the anode and the cathode respectively.

The average velocity of the particle along the direction of electric field is called drift velocity and is given by,

$$v_d = \mu E \tag{2.27}$$

where μ is called the mobility.

2.2.1.3 Electron Loss

Recombination

The created electrons and ions may be lost during their drift towards the corresponding electrodes due to two processes: recombination and electron attachment. In the absence of electric field, the ion-electron pairs recombine through their electric attraction and emit a photon in this process,

$$X^+ + e^- \longrightarrow X + h\nu \tag{2.28}$$

The rate of recombination is given by,

$$\frac{dn}{dt} = bn^-(t)n^+(t) \tag{2.29}$$

The recombination of ions and electrons depends on their concentrations $n^+(t)$ and $n^-(t)$ and the recombination coefficient, b.

Electron Attachment

The free electrons get attached to the electronegative atoms and form negative ions.

$$e^- + X \longrightarrow X^- + h\nu \tag{2.30}$$

The electronegative gases like O_2, Freon, Cl_2, SF_6 etc. will reduce the efficiency of the detector by capturing the electrons before they reach the electrodes.

2.2.1.4 Avalanche Multiplication

High electric field accelerates the electrons produced by the primary ionization. The primary electrons with sufficient kinetic energy collide with the nearby gas molecules and produce secondary electrons and they further interact and produce tertiary ionization. This chain of interaction continues and results in the formation of an avalanche (see Fig. 2.6).
The probability of an ionization per unit length is known as the *first Townsend coefficient* and is given in terms of the mean free path, λ

$$\alpha = \frac{1}{\lambda} \tag{2.31}$$

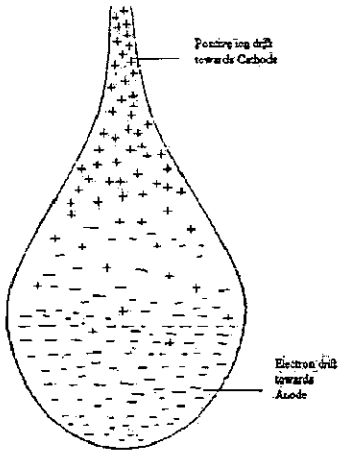

Figure 2.6: Shape of an avalanche. The slow positive ions trail behind the fast moving electrons

The number of electrons increases exponentially with the distance traveled by an electron in an electric field and is proportional to the initial number of electrons, N_0

$$N = N_0 e^{\alpha z} \tag{2.32}$$

The electron gain or the multiplication factor is then

$$G = \frac{N}{N_0} = e^{\alpha z} \tag{2.33}$$

2.2.2 Resistive Plate Chamber

Resistive Plate Chambers (RPCs) are gaseous parallel plate detectors with excellent spatial and time resolutions. RPCs were first developed by R. Santanico and R. Cardarelli [25] and are based on the same principle of spark chamber developed by Pestov and Fedotovich [26,27]. These detectors have been successfully used in many particle physics experiments for trigger and TOF applications. An RPC consists of two parallel plate electrodes with high bulk resistivity of about 10^{12} Ωcm which are usually made of glass or Bakelite (phenol formaldehyde resin). The backside surface of the plates are coated with suitable conductive coating like graphite having resistivity of the order 10^6 $\Omega/\square$ [20]. A gas gap is maintained in between parallel electrodes to produce primary ionization clusters and proper gas gain. The charge signal from the RPC depends on the gas gap. Spacers are placed to keep the uniformity of the gas gap throughout the volume of the detector otherwise due to electrostatic attraction the electrode plates may come close together. The signal

readout is taken from both X and Y readout strips which are kept perpendicular to each other. The metallic pick-up strips are separated from the graphite coating by thin insulating Mylar sheets. Fig. 2.7 shows the schematic diagram of an RPC.

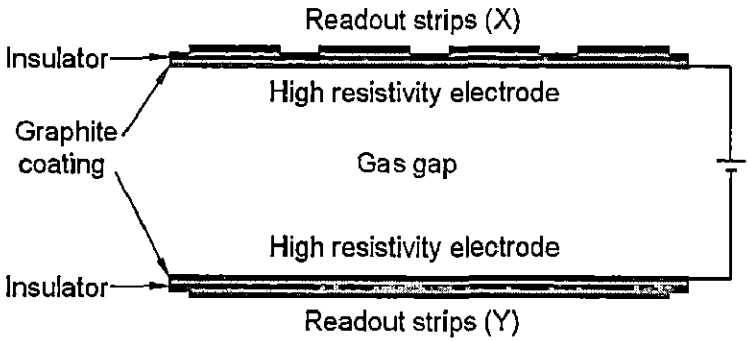

Figure 2.7: Schematic diagram of an RPC.

2.2.2.1 RPC working principle

An incoming charged particle that passes through the detector gas gap will transform some or all of its energy to the gas molecules in the active volume. The particle interaction through various physics processes happening inside the the gas gap, creates both positive and negative charged particles. The high voltage applied on the resistive plates causes an electric field to develop in the RPC. For the parallel plate geometry like RPC, the electric field between the two electrodes is uniform roughly V/d, where V is the applied high voltage and d is the distance between the electrodes. There are two kinds of charge carriers produced in the RPC during a particle interaction, negatively charged electrons and positively charged ions. Electrons are mostly responsible for the induced signal and the ions are responsible for the tail region of the signal. Under the influence of electric field, each electron multiply due to the secondary ionization by colliding with the nearby gas molecules. Some of the electrons also have a probability to get attached with the electronegative gas molecules present in the gas mixture. The effective charge carriers after multiplication and attachment proceed towards the anode and grow and develop into an avalanche. When the avalanche contains a large number of charge carriers, the net

electric field will be the resultant of the electric field due to the avalanche and the external electric field. This influences the gas gain and this phenomenon is called *space charge effect*. This process induces signals on both the x and y pick-up strips. Finally this signal from the detector is processed and stored.

2.2.2.2 Modes of operation

Avalanche Mode

In avalanche mode operation of an RPC, the gas amplification is decreased by a reduced electric field across the gas gap. By suitable selection of gas mixtures the avalanche growth can be controlled. The electron attachment and photon absorption are the two processes by which avalanche signal reduction occurs in an RPC . We slightly modify eqn. (2.33) by introducing another term called attachment coefficient, η. Now the gas gain can be written as,

$$G = \frac{N}{N_0} = e^{(\alpha-\eta)z} \tag{2.34}$$

where $\alpha - \eta$ is the effective Townsend coefficient. The signal generated in avalanche

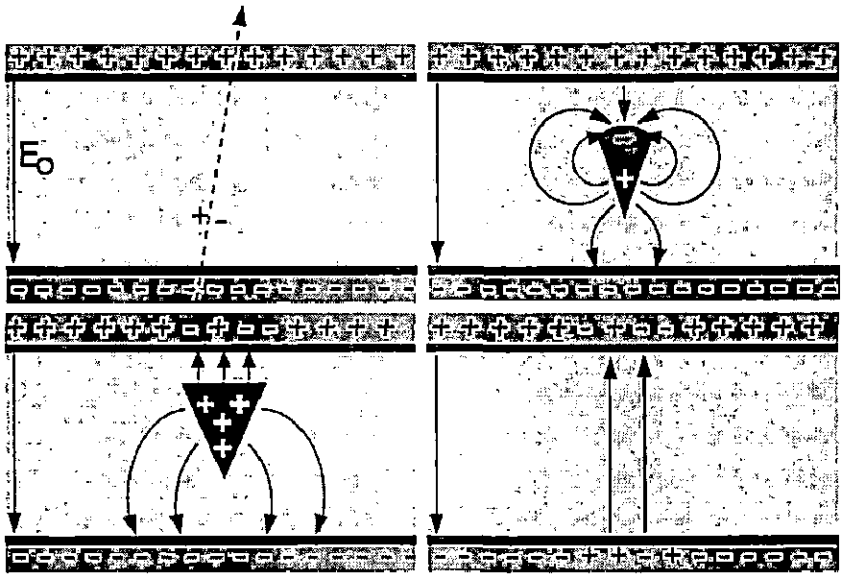

Figure 2.8: Schematic diagram of an avalanche development inside an RPC.

mode is small and hence pre-amplifiers are needed in the readout system. This mode of operation is suitable for high rate application like accelerator experiments. Fig. 2.8 shows various stages of an avalanche development inside the gas gap [28]. Initially, the charged particle passing through the RPC ionizes the gas medium.

Under the influence of the external electric filed , E_0 an avalanche develops in the gas gap. The internal field due to the charges in the avalanche also affects the E_0 in the small area where the avalanche develops. The faster electrons reach the anode quickly whereas heavy positive ions slowly reach the cathode.

Streamer Mode

In streamer mode of operation, the electric filed inside the gas gap is intense enough to generate localized discharges. Larger signals are observed in the streamer mode. This mode of operation is suitable for low rate applications like cosmic ray experiments. Fig. 2.9 shows the different stages of streamer development [28]. The avalanche developed spread quickly in the gas gap which also produces photons. These photons also contribute to the development streamer from the avalanche. A weak discharge is developed between the electrodes. The external electric field, E_0 is reduced in the discharge area.

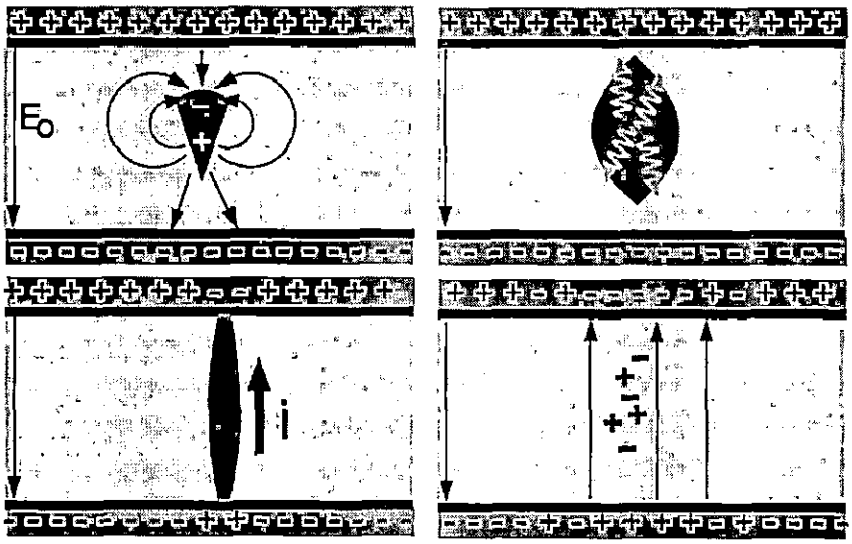

Figure 2.9: Schematic diagram of a streamer development inside an RPC.

Choice of gas mixture

Different factors are considered while selecting a proper RPC gas mixture. They include high gas gain, high rate capability, low working voltage and good proportionality. Working mode of the RPC i.e either avalanche or streamer mode is selected by the gas mixture. In streamer mode operation, usually a mixture of isobutane (iso-C_4H_{10}), Freon ($C_2H_2F_4$/R-134a) and Argon is used. While in avalanche mode, Freon, isobuatne and Sulfur hexaflouride (SF_6) gas mixture is used. Freon has high

electron affinity and reduces the streamer size from spreading transversely due to electron capture. Freon gas is safe, inflammable and non-ozone depleting. It has high density i.e high primary ionization and low operating voltage. But the global warming potential of Freon is 1300 times greater than CO_2 gas. Also it produces HF (Fluoridric acid) that damages the electrode surface. Isobutane prevents a secondary streamer by absorbing efficiently UV photons emitted by the de-excited molecules. Argon provides high charge multiplication. Even very small concentration of highly electronegative SF_6 reduces the charge signal by capturing electrons [29–31].

2.2.2.3 RPC Applications

Trigger RPC

Resistive Plate Chambers (RPCs) used for triggering the muon detector system are termed as Trigger RPCs. The single/double gap RPCs with gas gap 2 mm and operating voltage around 10 kV are used for triggering. They give very good detection efficiency (around 98%) and time resolution (around 1 ns).

Timing RPC

RPCs with multi-gap configurations with gas gap 0.2 to 0.3 mm is used in TOF applications. They work in avalanche mode and give around 99% efficiency and very good time resolution below 50 ps.

2.3 Summary

Resistive Plate Chambers (RPCs) have found extensive use in high energy physics and astroparticle experiments. Some of the past, currently running and future proposed experiments using RPCs as detector elements are listed in Table 2.2. The India based Neutrino Observatory (INO) collaboration will use a 50 kton magnetized iron calorimeter (ICAL) detector to study neutrino oscillations and measure their associated parameters. ICAL will use 28,800 glass Resistive Plate Chambers (RPCs) of 2 m X 2 m size to be operated in the avalanche mode, as its active detector elements. This thesis will discuss the experimental and simulation studies of ICAL RPCs.

Table 2.2: RPCs in various experiments [20]

Experiment	Area(m^2)	Electrodes	Gap(mm)	Gaps	Mode	Type
PHENIX	?	Bakelite	2	2	Avalanche	Trigger
NeuLand	4	Glass	0.6	8	Avalanche	Timing
FOPI	6	Glass	0.3	4	Avalanche	Timing
HADES	8	Glass	0.3	4	Avalanche	Timing
HARP	10	Glass	0.3	4	Avalanche	Timing
COVER-PLASTEX	16	Bakelite	2	1	Streamer	Timing
EAS-TOP	40	Bakelite	2	1	Streamer	Trigger
STAR	50	Glass	0.22	6	Avalanche	Timing
CBM TOF	120	Glass	0.25	10	Avalanche	Timing
ALICE Muon	140	Bakelite	2	1	Streamer	Trigger
ALICE TOF	150	Glass	0.25	10	Avalanche	Timing
L3	300	Bakelite	2	2	Streamer	Trigger
BES III	1200	Bakelite	2	1	Streamer	Trigger
Babar	2000	Bakelite	2	1	Streamer	Trigger
Belle	2200	Glass	2	2	Streamer	Trigger
CMS	2953	Bakelite	2	2	Avalanche	Trigger
OPERA	3200	Bakelite	2	1	Streamer	Trigger
YBJ-ARGO	5630	Bakelite	2	1	Streamer	Trigger
ATLAS	6550	Bakelite	2	1	Avalanche	Trigger
ICAL	97,505	Both	2	1	Both	Trigger

CHAPTER 3

RPC DEVELOPMENT AND INSTRUMENTATION

India based Neutrino observatory (INO) require 28,800 RPCs to be deployed as active detector elements in its Magnetized Iron Calorimeter (ICAL) for studying the properties of atmospheric neutrinos. A dedicated and aggressive R& D study has been done in developing the Resistive Plate Chambers starting from small dimensions of 30 cm × 30 cm to large area RPCs of dimensions 1 m × 1 m as well as 2 m × 2 m. In this chapter, we will study the design and development of 1 m × 1 m RPC and its associated DAQ and electronics. We will also study, the experimental results of the effect of the percentage of highly electronegative gas, SF_6 in the charge development on the RPC pick-up electrodes.

3.1 Fabrication of RPC

The proper selection and development of suitable materials for assembling the Resistive Plate Chambers are based on various R&D programs by the INO team [32,33]. The fabrication involves the selection of good quality materials for which the optimization of various assembly and quality control procedures were followed. The various materials like 3 mm thick float glass sheets which are used to make the RPC gaps are procured from a local company (M/s Asahi Float). The glass electrodes were coated with a special semi-resistive paint containing modified acrylic resin as binder, conductive black pigment and solvents including aromatic hydrocarbons and alcohols. The paint was developed indigenously with the help of a local company (M/s Kansai-Nerolac). Poly-carbonate edge-spacers, buttons for maintaining the gas gap and gas nozzles were used for making the gas gap. The pick-up panels are made from 5 mm plastic honeycomb material which are laminated on one side by 100 μm thick aluminum sheet and 50 μm thick copper sheet on the other side. The signal pick-up are strips of 30 mm width are made by machining on the copper sheet.

The fabrication procedure will be discussed in detail in the following sections.

3.1.1 Selection of glass for RPC electrodes

The selection of glass materials for INO RPCs have been carried out through detailed studies on glass samples supplied by various manufactures like Modi, Asahi float and Saint Gobian etc. After these studies, Asahi float glass was selected for making the electrodes for INO RPCs. Dielectric constant of the glass electrode of RPC is one of the inputs to the calculation of electric field.

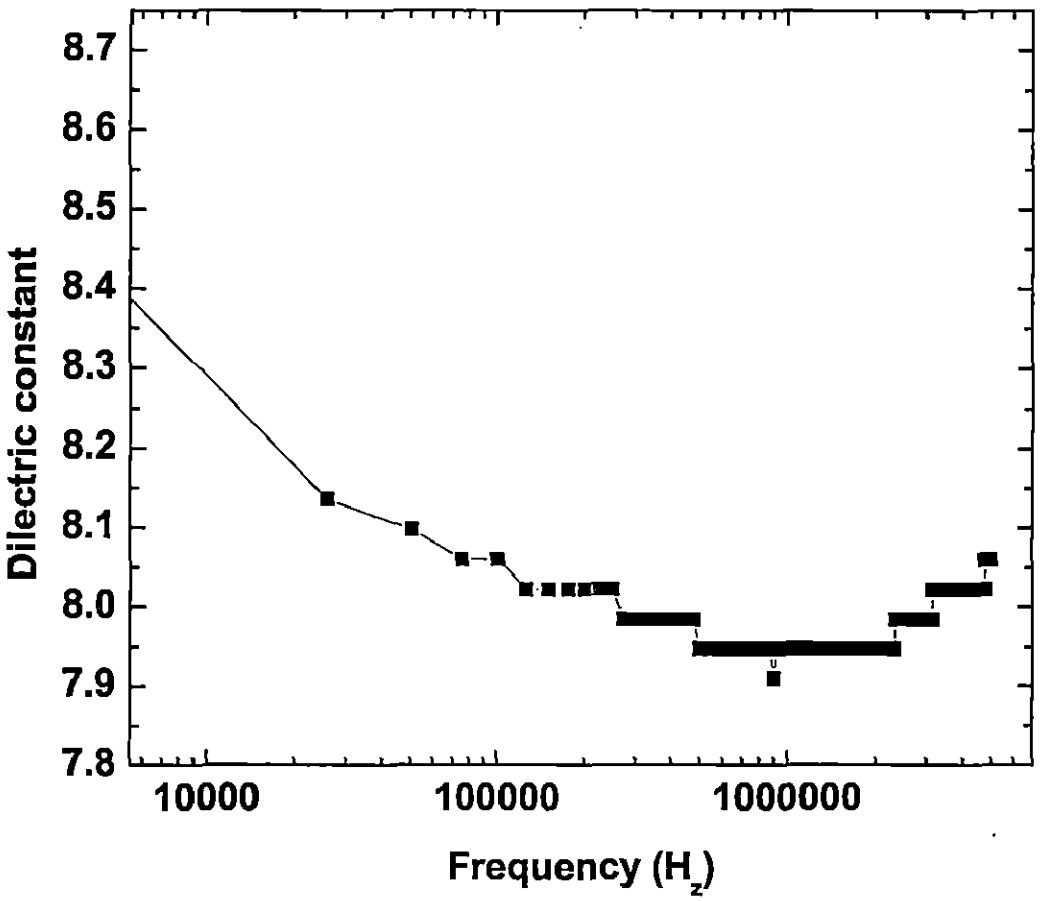

Figure 3.1: Dielectric constant measured for different frequencies.

We measured this quantity by converting a 3 cm × 3 cm Asahi glass sample of 3 mm thickness into a capacitor by putting copper tape on the upper and lower glass surfaces. Then we connected this setup to an Impedance Analyzer (HIOKI IM3570) to measure its capacitance at different frequencies. The value of the dielectric constant was calculated from the capacitance equation,

$$C = \frac{k\epsilon_0 A}{d} \tag{3.1}$$

Here A and d are the dimensions of the glass sample, k is the dielectric constant and ϵ_0 is the permitivitty of free space. The measured glass dielectric constant for different frequencies is shown in Fig.3.1. The average value of the dielectric constant was found to be 8.0 which was used in the simulation.

3.1.2 Preparation of glass electrodes

Two Asahi float glasses of 3 mm thickness of similar properties are selected for making RPC electrodes. The corners of each glass plates are chamfered at 45 degree. The next step is glass electrode coating. The glass plates are first cleaned properly with ethyl-alcohol and rinsed with distilled water. The glass plates are further cleaned with soap solution (Labolene) and distilled water before applying Nerolac conduction paint uniformly over the glass surface. The resistive coating helps in applying high voltage on the RPC electrode. At high bias voltage gas becomes conductive and hence the different layers paint-glass-gas act as conductor-dielectric-conductor structure which are capcitively coupled. So the signal which is produced by the passage of an ionizing particle is induced on the pick-up strips mounted above the resistive electodes. The surface resistivity of the electrode coating is preferred in the order of 1 MΩ. This is because around this value of surface resistivity, a localized discharge of area 0.1 cm^2 is developed in the gas gap with an ionizing particle which does not produce much cross-talk between adjacent pickup strips. If the surface resistivity is less, then the cross-talk will be very large. The surface resistivity of painted glass plates is measured using a jig of 15 cm. The indigenously developed jig is made up of two conducting bars of length, L which are separated by a width, W and fixed in a frame to form a square structure. The Resistance, R of the painted surface of thickness, t which is measured between two conductors is then proportional to $L/(W \times t)$ and is dependent only on the thickness, t of the coating. Fig. 3.2 shows the contour plots of surface resistivity measured for both the glass electrodes using the jig.

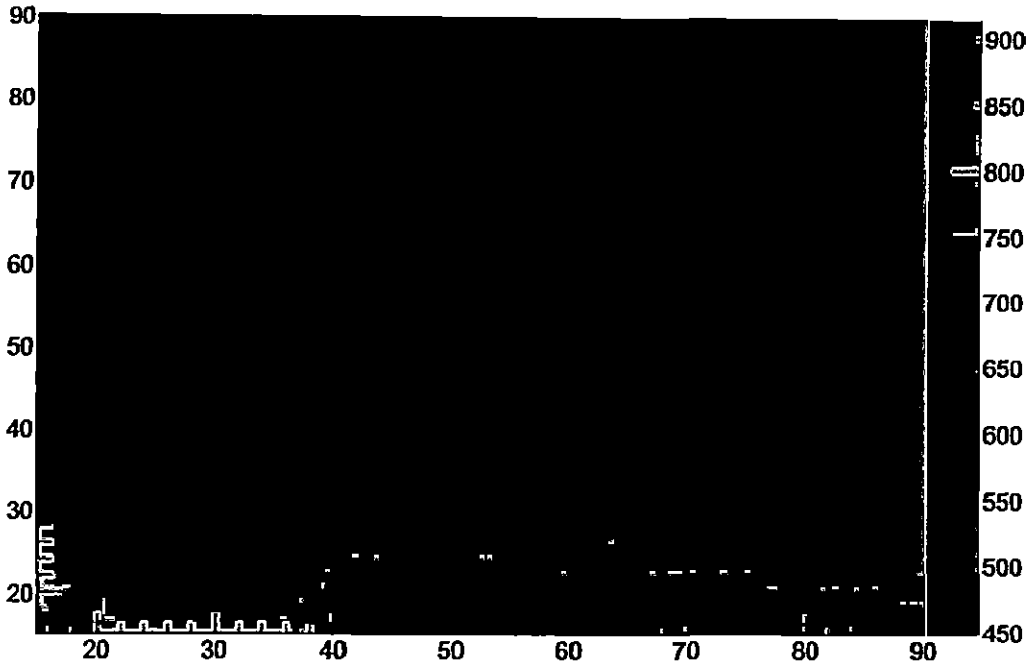

(a)

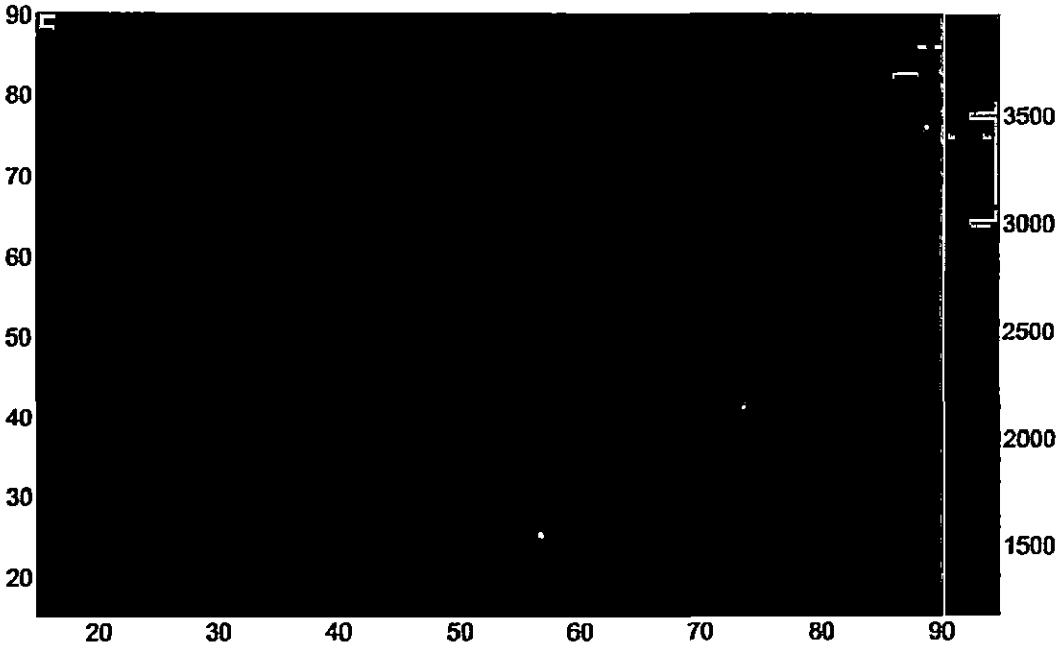

(b)

Figure 3.2: Surface resistivity plot of (a) upper side of the glass electrode and (b) bottom side of the glass electrode. The surface resistance is measured in kΩ/□

3.1.3 Making the gas gap

The gas gap for Resistive Plate Chamber is constructed by mounting two one side painted glass electrodes of specified area and thickness one above the other separated by a required gap between them. Firstly we keep one glass with painted surface facing below on the assembly table. Now we apply precise amount of glue (3M Scotch-Weld DP190 Gray epoxy adhesive)on the top of unpainted surface at every 200 mm spacing. Then we put poly-carbonate buttons shown in Fig.3.3 on this glue and again we apply a little drop of glue on the top of spacer button.

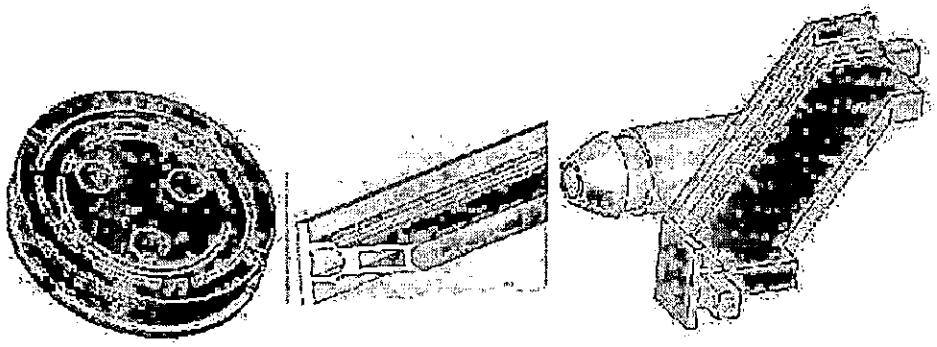

Figure 3.3: Button, spacer and gas nozzle.

The second glass plate is placed with the unpainted surface down on the top of the button spacer. Now we cover the assembly with a polythene sheet with their edges sealed on the assembly table with masking tapes. In order to make sure that the buttons glued nicely on both sides of the glass electrodes, we use the vacuum jig and start the suction pump for atleast 4 hours. This process removes the air from the volume created by the polythene sheet and the atmospheric pressure exerted on the polythene sheet gradually presses and tightens the glass electrodes against the spacer buttons. After this, we clean the edge spacers and gas nozzles with alcohol and put them along the sides of the gas gap. Then we apply glue between the edge spacers and gas nozzles and we keep it for few hours to harden the glue. When the glue sets on one side, we overturn the gas gap and again apply glue on the other side and keep it for some time for hardening the glue. If the gluing is not done properly, there are chances of gas leaks. In order to test this, we fill the chamber with freon gas with all the gas nozzles in the four corners sealed. Then we check for the leak position which is identified by Freon sniffer RIKEN GH-202 and re-gluing is done wherever necessary. When the gas gap is ready, the entire assembly of the gas gap looks as shown in Fig.3.4.

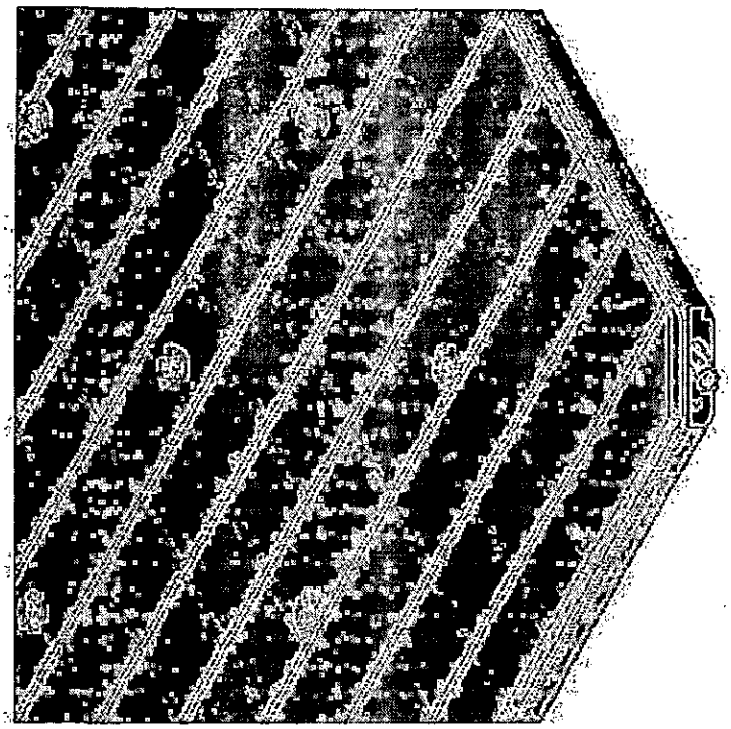

Figure 3.4: Schematic of gas gap assembly.

3.1.4 Assembling of an RPC

Once the gas gap passes the leak test, it is ready for the final packing, which is the final stage in the RPC fabrication. The high voltage cables are connected to the graphite layer by sticking on a copper tape and leads are then soldered on to the copper. A positive voltage is applied to one side and an equal and negative voltage to the other side, using a bipolar high voltage DC power supply. Then the pickup panels are mounted on either side of the gas gap which are separated from the glass electrodes using insulating Mylar sheets. The Mylar sheet is made from ethylene glycol and dimethyl terephthalate (DMT). The pickup panels are designed in such a way as to satisfy both the mechanical properties of the whole detector assembly and the electrical requirements of the circuit. The pickup panels are of honeycomb structure which is placed orthogonal to each other and then packed in an aluminium case that acts as common ground. The pickup panel consists of 64 copper strips for 2 m×2 m and 32 copper strips for 1 m×1 m RPC, on one side and a layer of 5 mm thick plastic and 100 μm aluminium foil on the other side. Each strip is machined to a width 28 mm and the gap between two adjacent strips is 2 mm. Honeycomb panels are lightweight and provide adequate mechanical strength. Each strip is terminated with a 50 Ω impedance to match the characteristic impedance of the preamplifier which follows the signal strip. Moreover, the attenuation of the pickup strips should

also be minimized. A fully assembled 1 m×1 m RPC is shown in Fig.3.5.

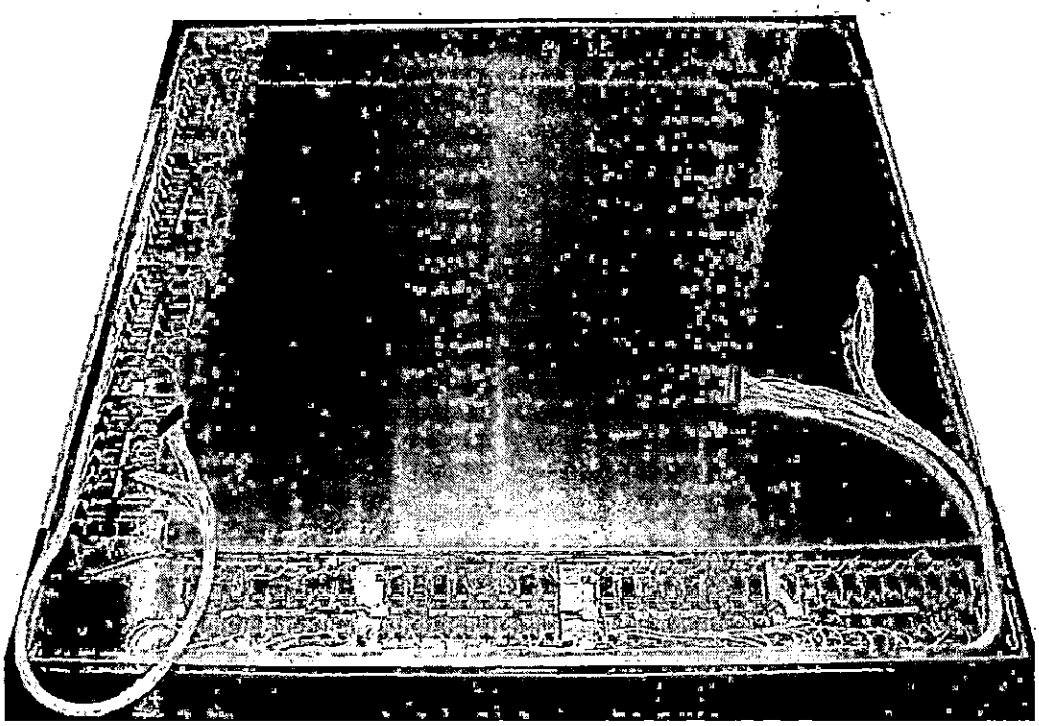

Figure 3.5: Fully assembled 1 m×1 m RPC with preamplifier boards connected after the pickup strip.

3.2 INO Prototype Detector Stack

A 12 layer 1 m×1 m RPC prototype detector stack has been used for the measurement of various RPC parameters like the tracking efficiency, the timing resolution, the charge collected by the pick-up strip etc. The picture of this detector is shown in Fig.3.6 [34]. From this figure, we can see two big aluminium racks that houses the front-end electronics for both x and y side signals which are placed on either side of the detector array. The front-end electronics and cabling are designed for both the negative polarity signals from the anode side as well as the positive polarity signals form the cathode side. There are 64 pickup signals from both x and y

readout planes (32 each) of the RPC. The readout channels are arranged into eight groups, each of this group is processed by 8-in-1 fast preamplifier board. The electric fields across the RPCs are applied by a differential high voltage of around ±4.9 kV. Also low voltage d.c power supplies of ±6 V and ±8 V are used for the preamplifier boards and front-end electronics. We can see the gas system on the left side of Fig.3.6 that supplies an avalanche gas mixture of R134a/Isobutane/SF_6 in a proportion 95.2/4.5/0.3 to every RPCs in the stack. Flow rates in the input channels are properly calibrated. The prototype detector stack is continuously tracking cosmic ray muons. The data acquisition system (DAQ) and the dedicated electronics are used to fetch information such as RPC strip hit profile and the timing information from the detector stack when a genuine muon event occurs, satisfying the trigger condition.

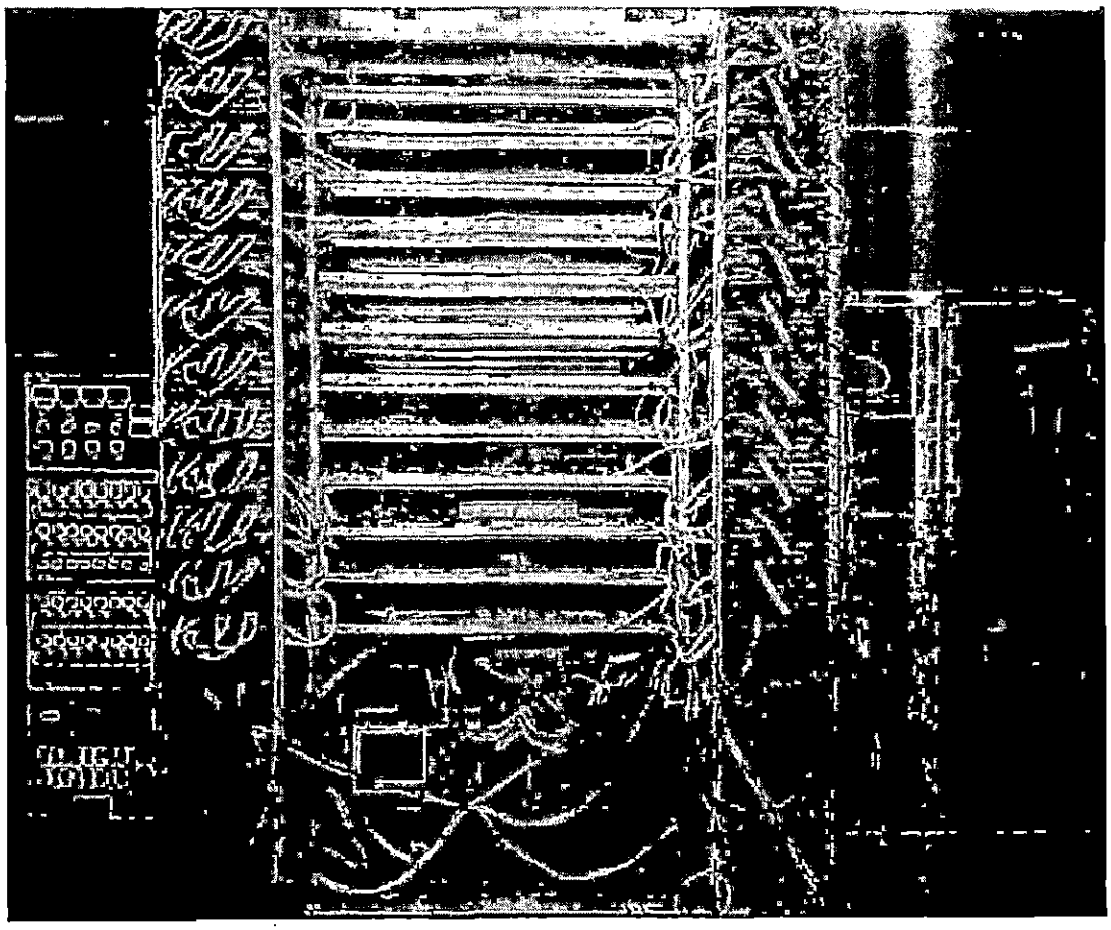

Figure 3.6: Prototype RPC detector stack along with the gas system (left) and DAQ and power supply systems.

3.3 Electronics and data acquisition systems

The Front-End electronics [20] and the Data Acquisition System (DAQ) [35,36] are designed in such a way to track the high energy cosmic muons that pass through the prototype detector stack. From this detector data, collected by the DAQ, we could measure various RPC parameters like the tracking efficiency, the timing resolution, the charge collected by the pick-up strips etc. The different stages involved in the data acquisition process are shown in the flow diagram 3.7 and are explained in detail in the following sections.

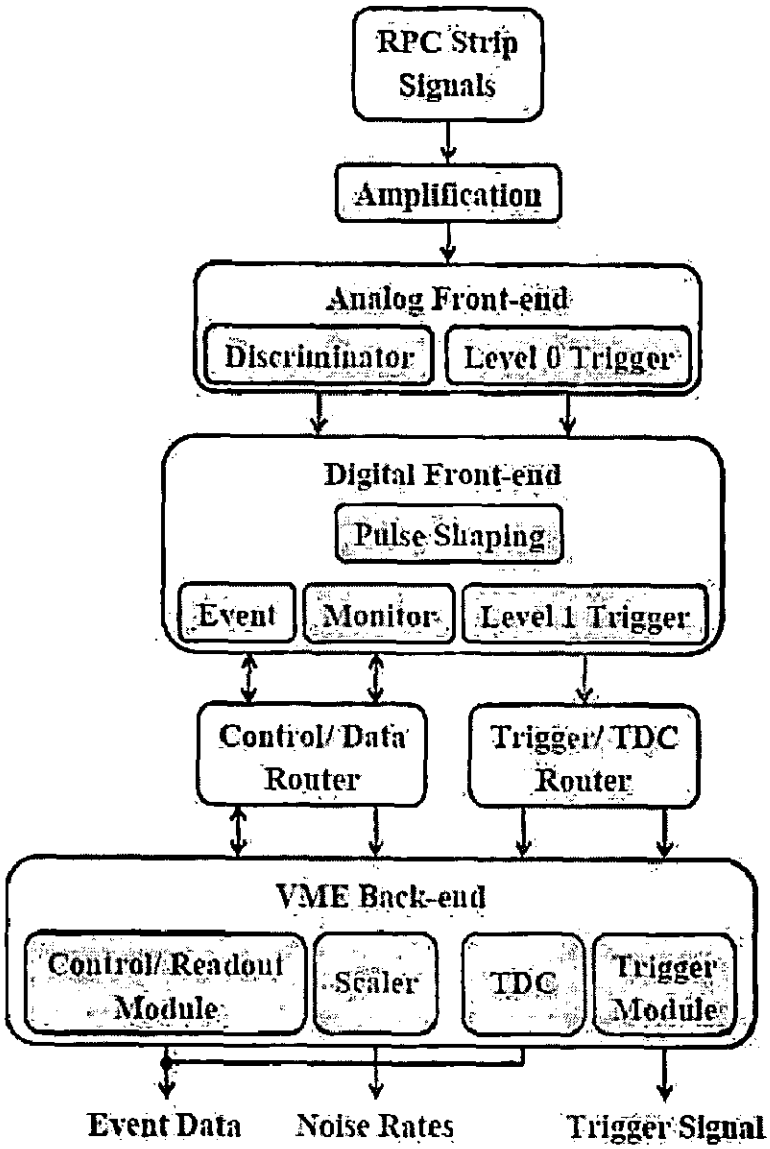

Figure 3.7: Flow diagram of DAQ scheme [36].

3.3.1 Preamplifier board

The signals from the RPCs are very weak since they are operated in the avalanche mode. The amplitude of the signals is around 2 mV and rise time 1 ns on the pickup strips having an impedance of 50 Ω. So the preamplification for this weak signal is needed for further data processing. An 8-in-1, two-stage Hybrid Micro Circuit (HMC) based preamplifiers having low noise, high speed and high gain are used for this purpose. The first stage HMCs are of two types: BMC 1595 and BMC 1597 which are used in the positive and negative electrodes respectively to produce a negative polarity signal. This stage of preamplification gives a gain of 10. The second stage peamplification is done by HMC, BMC 1513 which also provides a gain of 10. The characteristic gain of the preamplifiers measured for all the eight channels in a preamplifier board is shown in Fig.3.8.

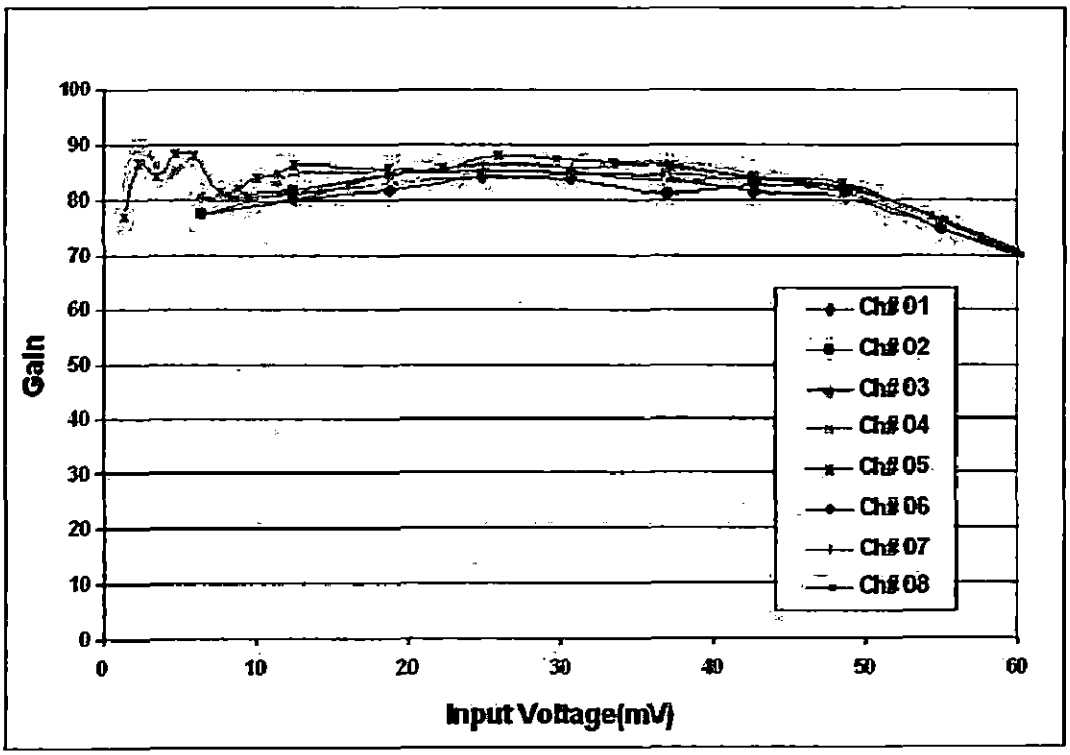

Figure 3.8: Preamplifier gain characteristics.

3.3.2 Analog Front-End (AFE)

After preamplification, the RPC signals are processed by the Analog Front-End (AFE) boards. The AFE coverts amplified analog signals from RPC strips into ECL (Emitter Coupled Logic) pulses using discriminator circuits. The AFE boards uses

a discriminator threshold (adjustable up to 500 mV) of -20 mV. The discriminator output signals of every eighth channel (in the fashion, 1 and 8, 2 and 9, 3 and 10...) are logically *OR*ed to generate level-0 trigger. These signals are then shaped to 100 ns. An AFE board can handle 16 RPC signals. Therefore two AFE boards are required for handling 32 pickup signals on one side of the 1 m × 1 m RPC.

3.3.3 Digital Front-End (DFE)

The discriminator signals and level-0 trigger signals are fed to the Digital Front-End (DFE) boards that can perform three different functions: event readout, monitoring and level-1 signal generation. The level-0 trigger signals are logically *AND*ed to make M-fold coincidence and is called level-1 trigger logic. For generating M-fold signals, level-0 signals are first converted into TTL signals and then fed to a CPLD chip (Xilinx XC9536-5PC44C). The ECL 1-fold signal is generated by logically *OR*ing the ECL level-0 signals outside the CPLD and is used to measure the timing of RPC signals at the back-end. The *level-1 trigger* signals are used at the back-end for generating the final trigger. The *event-readout* section manages shaped strip signals that are registered in a latch. This strip hit information along with board ID is flushed out serially with the generation of a final trigger. *Monitoring* section periodically monitors the noise rates from all the pickup strips, the four level-1 trigger signals and four fixed frequency signals.

3.3.4 Signal Routers

The communication between the front-end electronics and the back-end electronics is made possible through two signal routes: Control and Data Router (CDR) and the Trigger and Timing Router (TTR). The CDR board is used to route the readout signals from the RPC to the back-end, whereas the TTR routes the level-1 trigger signals from the DFEs to the final trigger module situated at the back-end.

3.3.5 VME based back-end

Finally the detector data from the Front-end electronics is collected by a VME based back-end and it communicates with the PC via a PCI-VME bridge [37]. A VME back-end consists of many commercial modules and some of them are discussed below.

Scaler

A commercial 32-bit scaler [38] counts RPC strip signals, four reference signals and level-1 signals periodically and sequentially. The scaler records the noise rate information and generate a VME interrupt by receiving the monitor trigger from the control and readout module.

Time to Digital Converter (TDC)

Timing from each layer of RPC is recorded by a multi-hit TDC of 100 ps resolution [39]. By receiving an event trigger from the control and readout module, timing information is recorded and a VME interrupt is generated. We used timing information from the TDC module after calibration to correct the differences in the propagation delay from strip to strip to measure the velocity of cosmic muons passing through the prototype detector [40].

Charge to Digital Converter (QDC)

The commonly used VME based Data Acquisition System (DAQ) has been modified for the experiment that will be discussed in this chapter, by adding QDC to the VME back-end. We used a commercial 12-bit QDC [41] with a least count 0.1 pC to measure the charge collected from the analog RPC pulses. QDC module (Model V792) has 32 input channels and one GATE input (ECL/NIM) common to all channels (see Fig.3.9). The integrated currents, received from the channel inputs when the GATE input signal is active, are converted into voltage levels by the QAC sections and then multiplexed and converted by two fast 12-bit ADC modules (see section.2 of V792 User's Manual [41]).

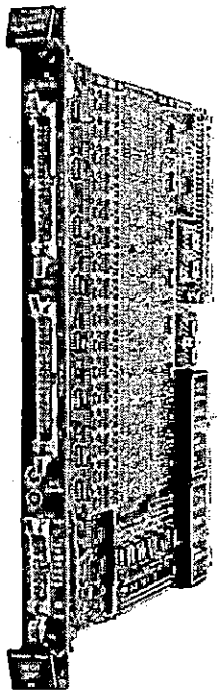

Figure 3.9: VME module QDC V792 [41].

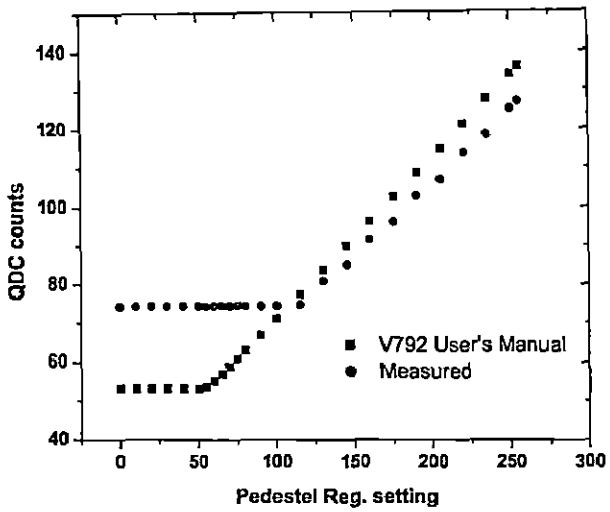

Figure 3.10: QDC V792 pedestel measurement.

Pedestel measurement has done to find the dynamic range of the QDC (see Fig.3.10). The QDC pedestal is the readout value when no input signal is present (open inputs).

3.4 Gas System

The Resistive Plate Chamber (RPC) is basically a gaseous parallel plate detector. For the proper functioning, the RPC requires an active volume containing an ionizing gas, an electronegative gas and a photon quenching gas. Depending on the modes of operation of RPC (i.e either avalanche or streamer mode) different combinations of gases are used. We used Freon (R134A) as an ionizing gas which has a high probability of primary ionization and also serves as a secondary electron quencher. Isobutane, which has a high absorption probability of UV photons, is used as the photon quenching gas. The highly electronegative gas, SF_6 is used in low percentage as the electron quencher. These gases are mixed in an appropriate proportion with a controlled flow through the gas detector, which is achieved through the on-line gas mixing and multi-channel distribution system [42]. The Mass-flow Controller (MFC) based gas mixing system (shown in Fig.3.11), can mix four input gases (Argon, Freon (R134a), Isobutane and SF_6) by volumetric method. It is able to distribute the gas mixture simultaneously to 16 output channels. In this system, capillary tubes are employed as flow resistors to control the gas flow rate in each of the output channels. The different components of the gas system are discussed below.

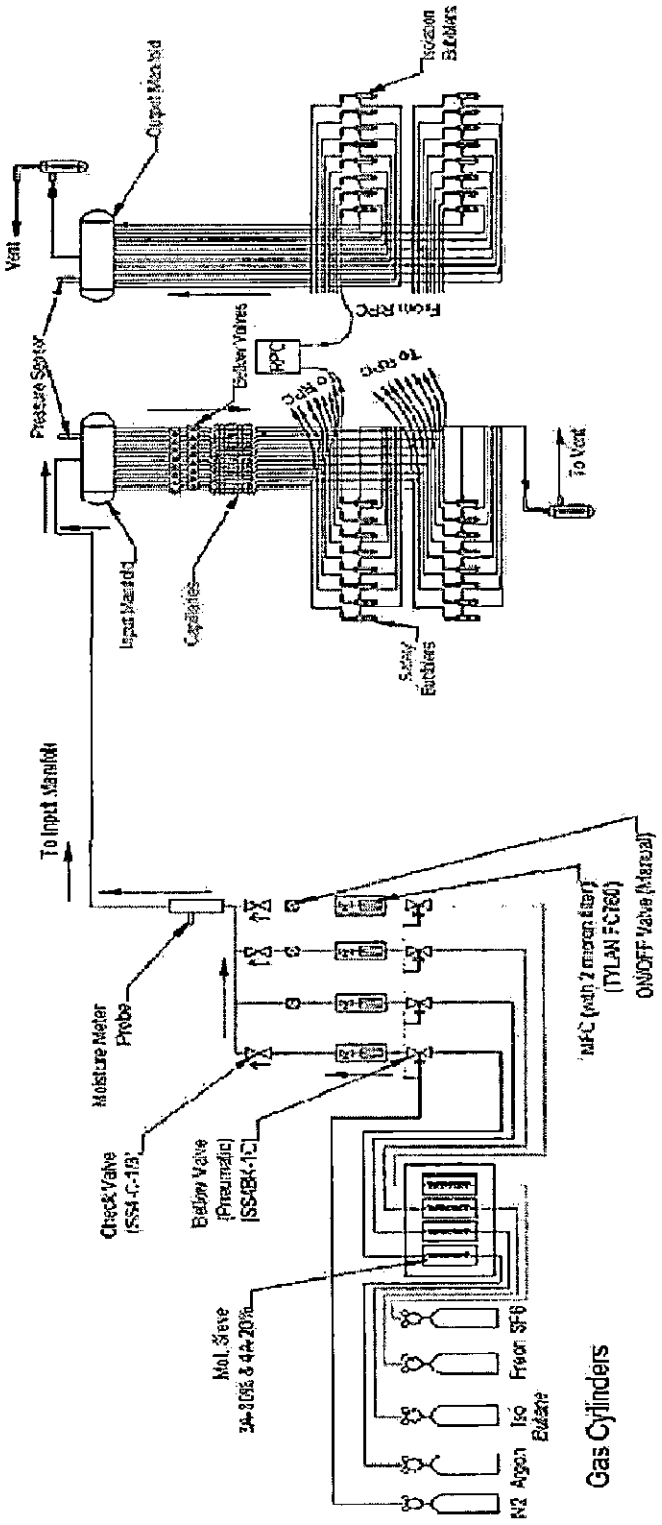

Figure 3.11: Gas mixing sytem.

3.4.1 Purifier column

The input gases supplied from the individual gas cylinders may contain moisture and other impurities that might have diffused through the valves during their transit time and storage. So these gases should be purified before supplying into the mixing unit. For this purpose, four in situ rechargeable molecular sieve-based columns (one for each input gas) are mounted on the input gas lines for absorbing moisture, oil traces and other contaminants from the gases. The molecular sieve-based columns are made of stainless steel and two built-in heaters of 500 W each which are connected in series. Each of these columns are charged with 300 g of molecular sieve absorbents of type 3 Å (80%) and type 4 Å (20%); the argon column has a 13X type absorbent in addition to these.

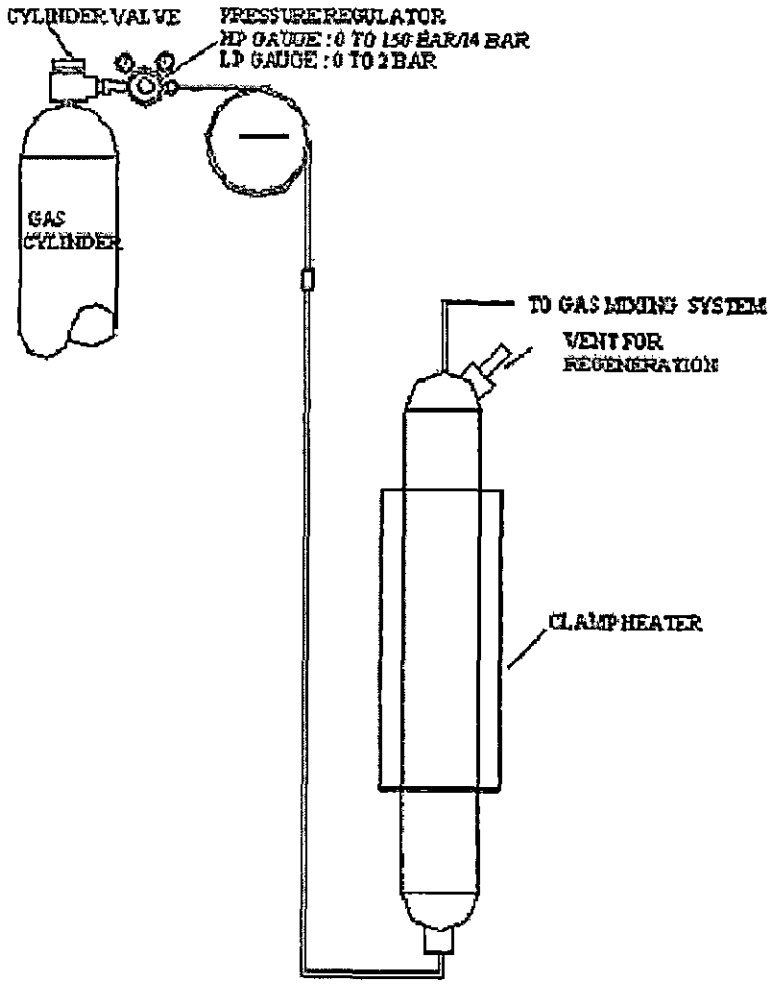

Figure 3.12: Schematic diagram of gas purifier system.

3.4.2 Mixing unit

After purification, the individual gases are sent to the gas mixing unit (shown in Fig.3.13). The gas mixing unit contains different components such as pneumatic valves, mass flow controllers, mixing line, check valves, bellow-sealed valves and also a probe for measuring moisture content. The bellow-sealed valves are pneumatically controlled and are activated by a pressure of about 4 bar. A dry nitrogen gas or an air compressor is used for maintaining this pressure.

3.4.3 Mass flow controllers

Mass flow controllers (MFC) of model FC-760 [43] are used for measuring and controlling the gas flow into the detector. MFCs are designed and calibrated to control a specific type of gas at a particular range of flow rates. There is a built-in 2 μm filter in each MFCs. The control input to MFCs and the output from the MFCs are DC voltages of range (0-5 V) which are linearly proportional to the mass flow. The flow rates are displayed as SCCM (Standard Cubic Centimeters per Minute) units. Flow rates of individual gases are calibrated. The calibration procedure is given in the following section.

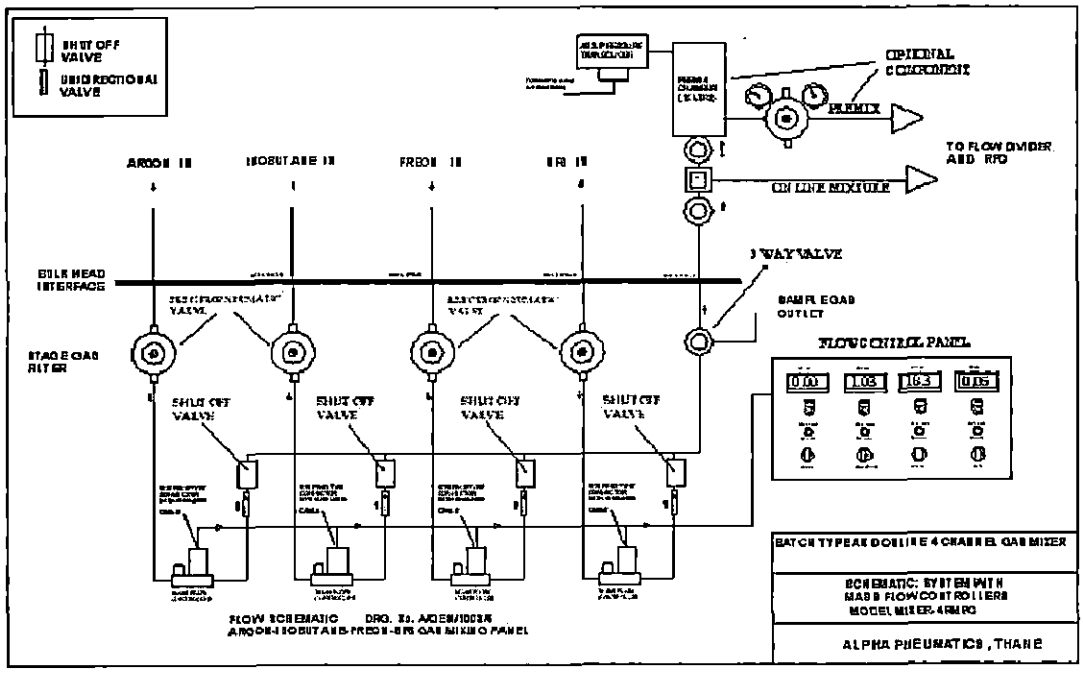

Figure 3.13: Schematic diagram of gas mixing console.

3.4.4 Distribution system

The distribution system consists of a manifold and pressure transducer gauge of range 0-1 kg/cm^2. The pressure transducer is used to indicate the pressure of the gas mixture. It operates on 15 V DC and gives a current of 4-20 mA. The gas mixture first enters into the manifold, from there it is mixed in a small cylinder which gives higher cross section and residence time. The manifold distributes the gas into the 16 channels. There are pneumatically activated valves for the individual channels and control switches are kept at the bottom front panels. Flow resistors which are 2 m long capillaries, provide uniform flow of gas mixture in all the gas chambers. The flow rate can be calculated by Hagen-Poiseulle relation [44]:

$$R = \frac{\pi r^4 \Delta P}{8\eta L} \tag{3.2}$$

where R is the gas flow rate, r is the capillary radius, P is the differential pressure and L is the length of the capillary tube.

3.4.5 Safety bubblers

In order to take care of the back pressure and to protect RPCs from the damages due to over pressure, safety bubblers are mounted on individual gas output lines. Safety bubblers are made of borosilicate glass and are connected to a stainless steel by a flexible Tygon tube. Every bubbler has a 25 mm column of silicon diffusion pump oil [45] (about 5 ml), which has a density of 1.8 g/cc. When over pressurization occurs due to blockages in the gas flow path, the bubbler relieves excess gas as bubbles through the oil.

3.4.6 Isolation bubblers

The Isolation bubblers prevent the back diffusion of air into the RPC. There are sixteen such bubblers in the present gas system. The gas mixture flowing out of each RPC is allowed to flow through the isolation bubblers. If there is no bubbling in isolation bubblers, that is the indication of proper gas flow in the RPC.

3.4.7 Calibration of Mass flow controllers

The rating on the MFCs corresponds to the flow of Nitrogen gas. So the MFCs should be calibrated for other gases before we use them in our experiment. The MFCs used in our gas system are calibrated using the downward water displacement method. They are again cross calibrated by the linear gas flow method. The calibration plots for Freon (R134a), Isoutane and SF_6 are shown in Figs. 3.14, 3.15 and 3.16 respectively.

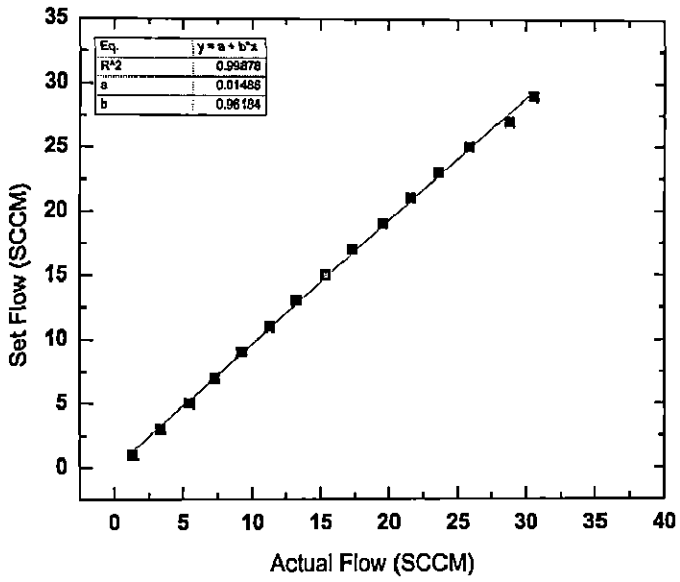

Figure 3.14: MFC calibration plot for Freon (R134a).

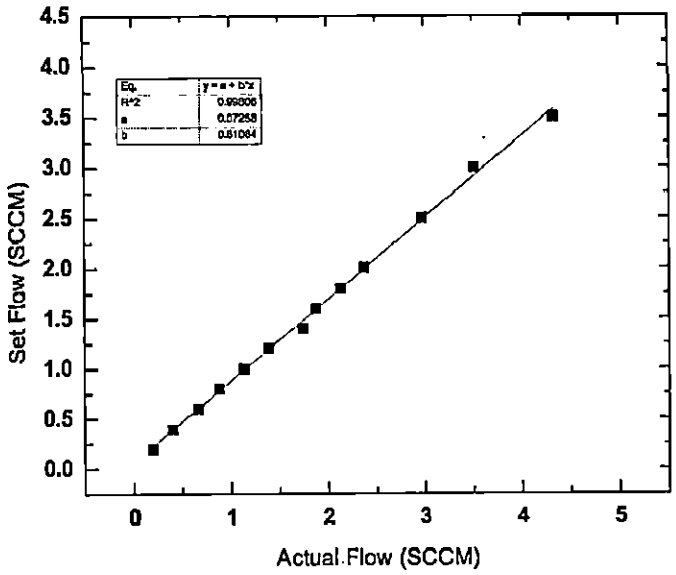

Figure 3.15: MFC calibration plot for Isobutane.

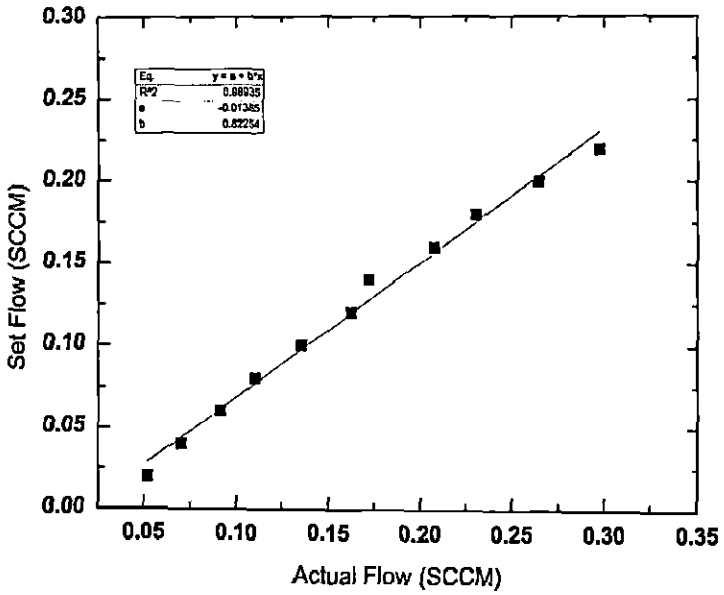

Figure 3.16: MFC calibration plot for SF_6.

3.5 Experiment setup for SF_6 studies

The experimental setup for finding the induced charge distribution on the RPC pickup strips when cosmic muons pass through the detector is shown in Fig.3.17. We have collected the charge distribution in two ways (a) by using DAQ system and (b) by using a CRO. The trigger setup has been made using scintillator paddles which is explained in the following section.

3.5.1 Trigger setup with Scintillator detetcor

The scintillator paddles are used as cosmic ray telescopes. A scintillator paddle is made up of a 1 cm thick scintillator tile, a light-guide and a Photo Multiplier Tube (PMT). The whole assembly is wrapped with a light reflecting material called *Tyrek* and further covered with a black *Tedler* paper in order to minimize the light losses and also to prevent the ambient light from entering into the detector. Fig.3.18 shows a fully assembled scintillation detector. When charged particles strike the scintillator tile, scintillations are produced. Then the light-guide carries the light produced by the paddle towards the PMT, which is optically coupled. The scintillations are converted into electrical signal and also amplified by the PMT.

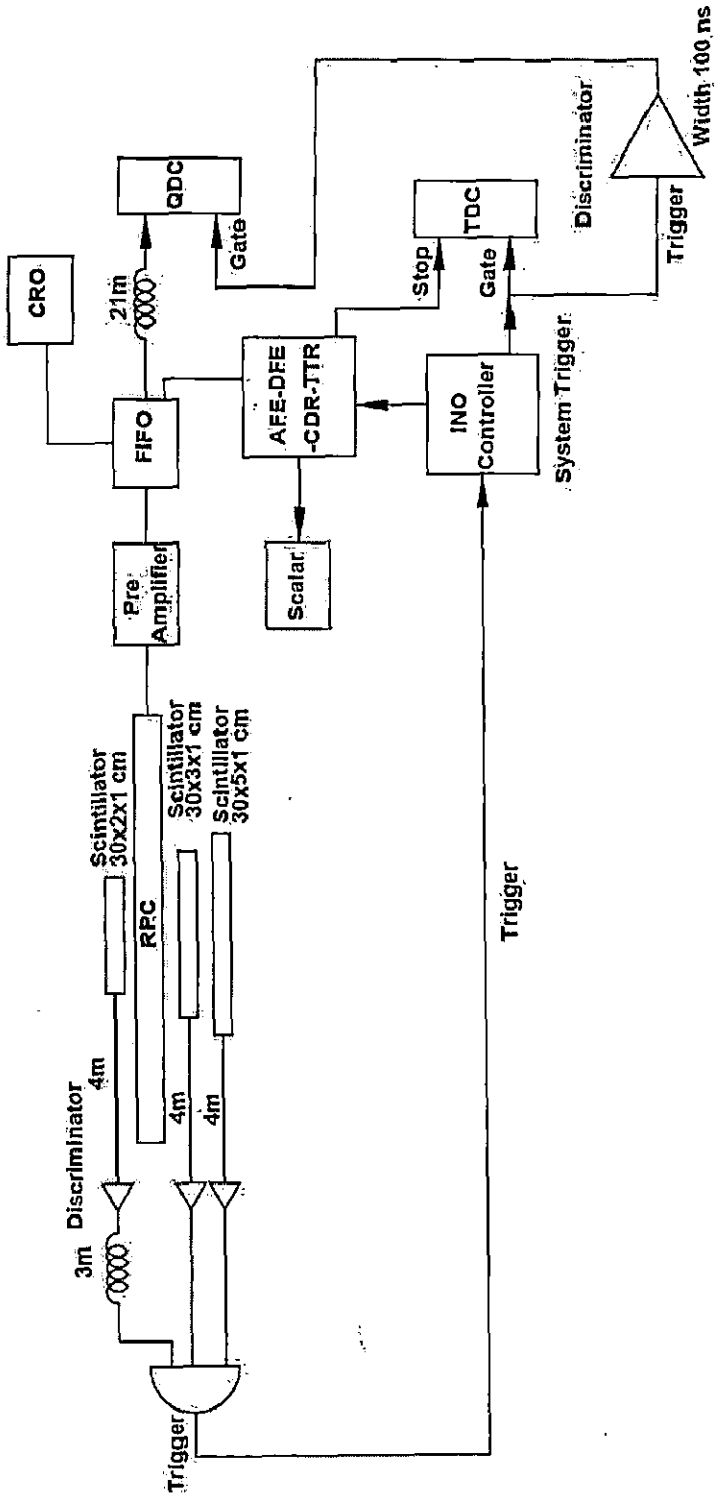

Figure 3.17: Experimental setup

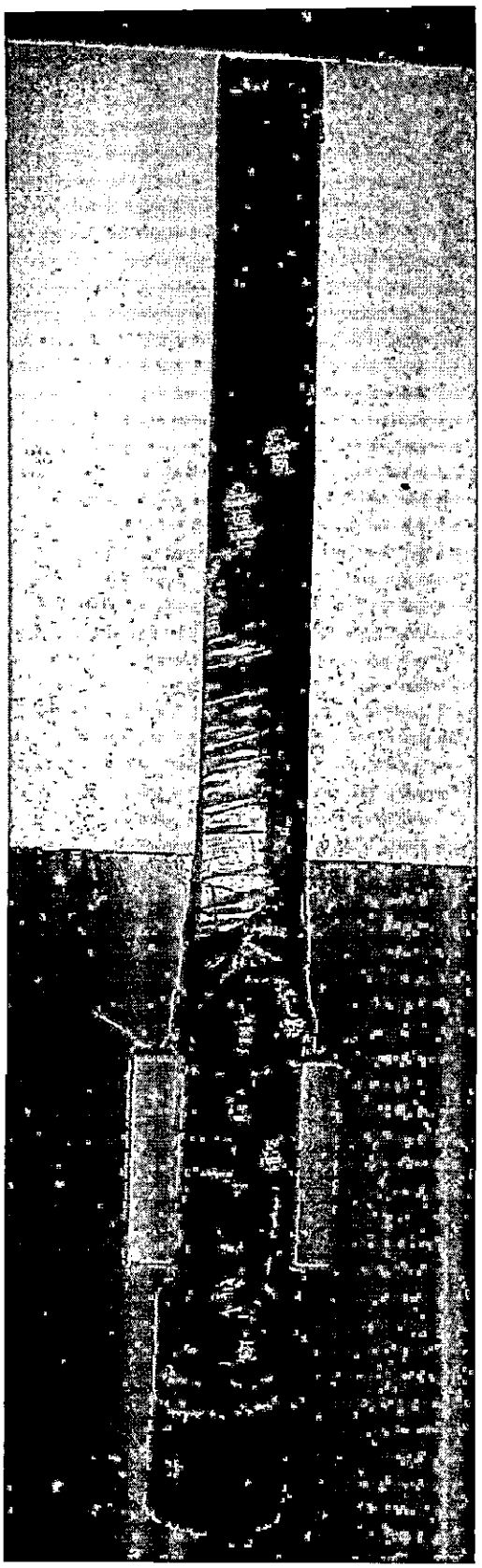

Figure 3.18: Scintillator paddle based cosmic muon telescope.

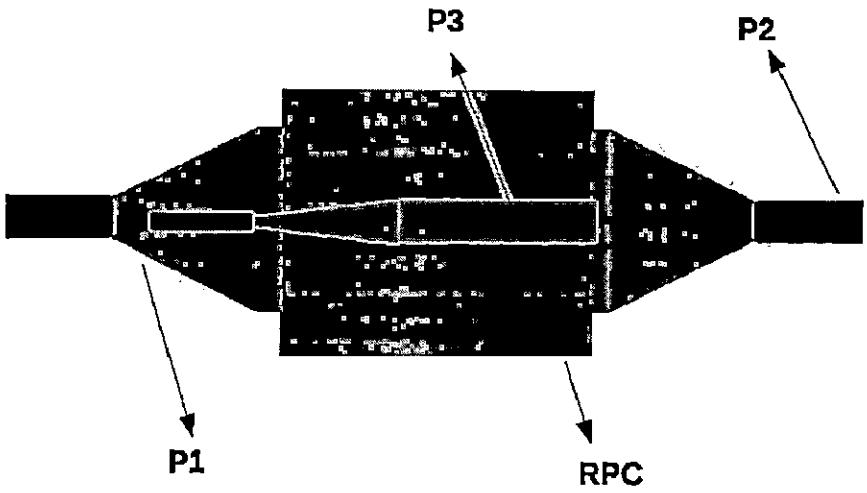

(a)

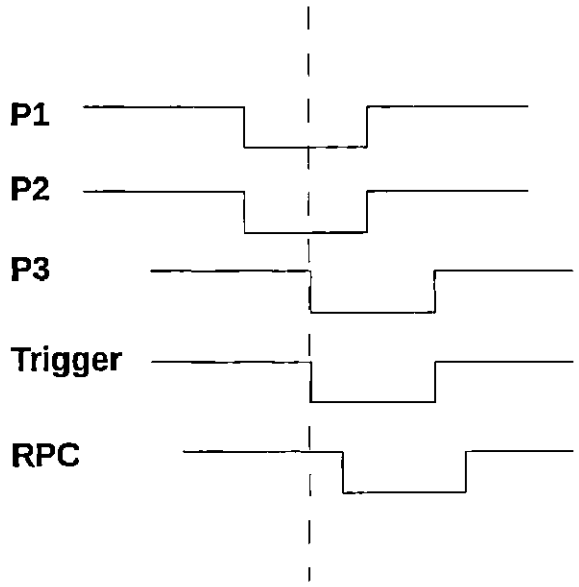

(b)

Figure 3.19: (a) Schematic diagram of trigger assembly using scintillator paddle and (b) Timing of scintialltor signals (P1, P2 and P3), trigger pulse (P1·P2·P3) and RPC signal.

Three scintillator paddles arranged vertically one above the other have been used for generating the trigger. A 30 cm×2 cm×1 cm, scintillator detector, which is placed above the RPC strip under study together with two scintillator detectors of

30 cm×3 cm×1 cm and 30 cm×5 cm×1 cm dimensions, which are placed below the RPC will provide a narrow window for the vertical cosmic muons. The measurement has been done with only one of the 32 strips of an RPC in the stack. The trigger setup has been placed appropriately so that the strip under study is sandwiched between them (shown in Fig.3.19). The RPC *events* are selected if the signals from the scintillator detectors obey the trigger condition,

$$Trigger = P1 \cdot P2 \cdot P3 \tag{3.3}$$

3.5.2 Effect of SF_6 on produced Charge

We used one 1 m × 1 m RPCs from the 12-layer RPC prototype detector stack at Tata Institute of Fundamental Research (TIFR), Mumbai for the experiment [46]. The experiment to find the charge collected by the RPC has been done by varying the concentration of SF_6 in small amount to a mixture $C_2H_2F_4/C_4H_{10}$. The analog pulses from the preamplifier of the RPC layer under study have been connected to linear FIFO in order to produce three buffered outputs. One copy of the output signal has been connected to QDC. The functioning of QDC is given in detail in section 3.3.5. The trigger signal is shaped to 100 ns and used as the QDC gate. The analog signal is appropriately delayed in-order to bring the avalanche pulse inside the gate. Besides, the RPC is operated in purely avalanche regime, where the fraction of the streamer pulses is negligible. A clean avalanche pulse within the *trigger* pulse is shown in Fig.3.20. The noise rate and temperature variation other than the day-night variation are comparatively very small which are shown in Fig.3.21. The charge measured with DAQ system and its fit with a Landau distribution as obtained using CERN ROOT package [47] for different gas mixtures are shown in Fig.3.22, where the fit parameters, p0 is the normalization coefficient, p1 is the most probable charge and p2 is the width of the distribution (Γ). The second copy of these signal has been fed to the usual DAQ signal path and the third signal has been connected to a digital sampling storage oscilloscope, using which analog pulses are digitized on the trigger signal and stored. The charge from the oscilloscope recorded signal is calculated using the formula $Q = \frac{\sum_{i=0}^{t} V_i \Delta t}{R}$, where the impedance R is 50 Ω, V_i is the amplitude of the signal at a sampling point i and Δt is the sampling interval. The charge distributions measured for various gas mixtures are shown in Figs. 3.23 and 3.24. The noise rate and the RH parameters (temperature and humidity) have been continuously monitored during the entire data taking period in order to ensure the good quality data.

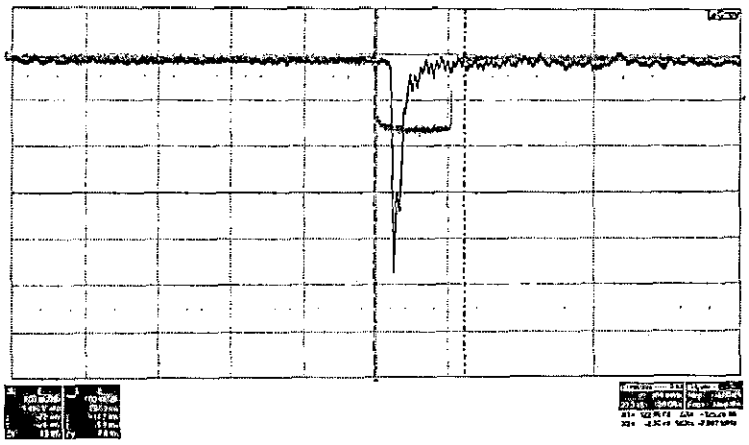

Figure 3.20: Screen shot of an RPC signal within the QDC gate.

We have done similar measurements we have for 2 m × 2 m RPC [20,33].

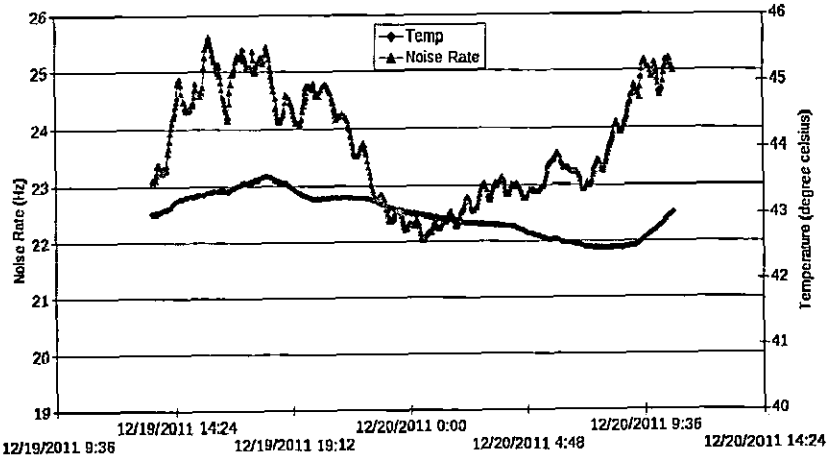

Figure 3.21: Noise rate and temperature of the RPC strip under study during the data taking period. The y-axis on the left side represents the temperature and the y-axis on the right side represents the noise rate.

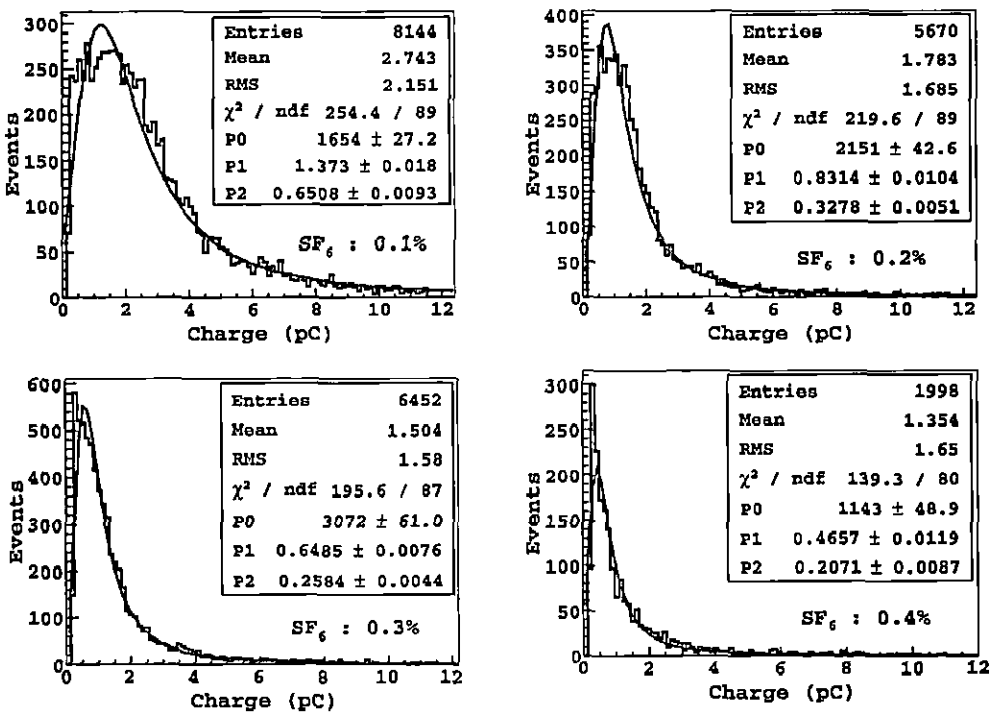

Figure 3.22: Measured charge distribution for different SF_6 concentrations in the gas mixture. Red line is the landau fit.

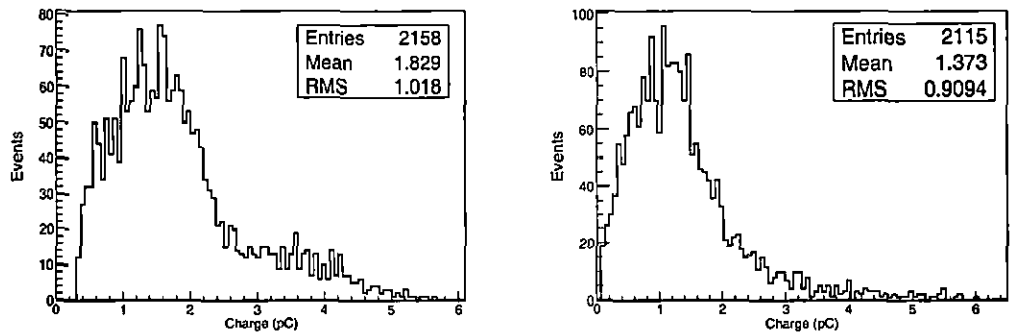

(a) (b)

Figure 3.23: Measured charge distribution for gas mixtures (a) $C_2H_2F_4/C_4H_{10}/SF_6$: 95.4/4.5/0.1 and (b) $C_2H_2F_4/C_4H_{10}/SF_6$: 95.3/4.5/0.2 with CRO.

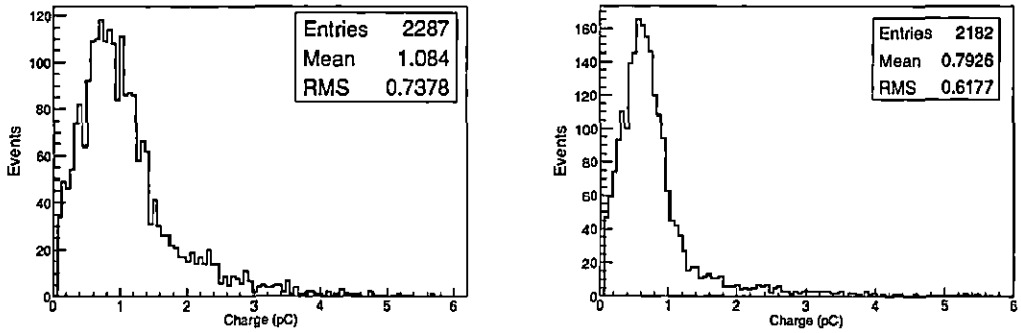

(a) (b)

Figure 3.24: Measured charge distribution for gas mixtures (a) $C_2H_2F_4/C_4H_{10}/SF_6$: 95.2/4.5/0.3 and (b) $C_2H_2F_4/C_4H_{10}/SF_6$: 95.1/4.5/0.4 with CRO.

3.6 Summary

In this chapter, we discussed the RPC fabrication procedure in detail. We also described about the Data Acquisition System, electronics and the gas mixing procedure for the detector. The experimental study was to find out the effect of SF_6 in the avalanche gas mixture. We could see from the results that, there is a drastic decrease in the charge distribution by increasing the amount of SF_6 in small quantities (0.1%, 0.2%, 0.3% and 0.4%) in the gas mixture. This result was interesting and motivated us to look into the numerical simulation of charge development in RPCs and this will be discussed in chapter 5.

CHAPTER 4

RPC SIMULATION AND TOOLS

Monte Carlo simulation is a very useful tool in High Energy Physics for designing an experiment and also for analyzing the results from the experiment. In High Energy Physics Experiments, Monte Carlo Simulations are used for event generation, tracking and detector performance studies. Particle event generators provide input to detector simulation program. Then the detector simulation program tracks the particle through the detector material by simulating the particle interaction with the material. Finally, we simulate the detector response and get the output from the detector. The commonly used event generators in high energy physics include Hadron event generator like PYTHIA [48], Heavy Ion event generator like HIJING [49,50] and neutrino event generator like GENIE [51]. The simulation of the passage of particles through the detector material can be done by simualtion toolkits like Geant4 [52]. The optimization of detector parameters is essential while designing and calibrating particle detectors. This can be done by device level simulations by either varying the field configuration or the composition of gas mixture. This will be mainly discussed in this chapter. The basic processes involved in a gas-based detector are,

- **Particle interaction and Primary Ionization.** An incoming charged particle ionizes the gas atoms or molecules in the active volume of the detector along its trajectory.

- **Electric Field.** The electric filed accelerates the charged particles (electrons/ions) towards corresponding electrodes.

- **Charge transport and Multiplication.** Electrons are multiplied in a strong electric field while drifting towards the electrode. The diffusion of electrons occurs due to their random nature of collision with the gas molecules.

↬ **Charge Induction.** The motion of electrons and ions induces a current on the readout electrodes.

All the above mentioned processes can be simulated by various simulation tools that are used to develop the complete simulation framework for the modeling of Resistive Plate Chamber discussed in this chapter. The interactions of relativistic charged particles with the gas medium and their energy loss can be simulated by the HEED program [53]. This program is based on the photoabsorption ionization (PAI) model proposed by Allison and Cobb [54]. The electric field within RPC is calculated by the nearly exact boundary element method (neBEM) solver [55–57]. The electron transport parameters are calculated using a semi-classical Monte Carlo simulation package called the Magboltz program [58] which solves the Boltzmann transport equations for electrons in arbitrary gas mixtures.

4.1 Primary Ionization

The excitation and ionization of gas molecules are two major phenomena that occur when relativistic charged particles travel through a gaseous detector. The energy deposited by these fast particles along their trajectory is normally very small and is of the order of a few keV. The average energy needed to produce one electron-ion pair is given by [59],

$$W = \frac{L}{\bar{n}} \left\langle \frac{dE}{dx} \right\rangle \tag{4.1}$$

where $\bar{n}$ is the mean number of electron-ion pairs created along the trajectory L and $\left\langle \frac{dE}{dx} \right\rangle$ is the mean energy loss per unit path length of the traversing particle. The mean energy measured for different gas mixtures is given in Table 2.1. The energy, W depends on many parameters like the composition and density of the gas and also on the nature of the primary particle. If the kinetic energy acquired by the electron is sufficiently high, the electron can further ionize the gas molecules. So every primary electron may produce more than one secondary electrons. The ionization process can be treated as a quantum mechanical phenomenon which occurs as the result of the field of traversing particle and the field of the atoms it interacts with. In the following section we discuss the energy loss of a charged particle in a polarizable medium which is characterized by complex dielectric constant, $\epsilon(k,\omega) = \epsilon_1(k,\omega) + i\epsilon_2(k,\omega)$.

4.1.1 Energy Loss by a Relativistic Particle

The energy loss produced by a relativistic charged particle can be calculated following the Landau method [60]

$$\frac{dE}{dx} = ze\vec{\mathrm{E}}(\vec{\mathrm{r}},t) \cdot \frac{\vec{\beta}}{\beta} \tag{4.2}$$

where $\vec{\beta}c$ is the velocity of the charged particle and $\vec{\mathrm{E}}(\vec{\mathrm{r}},t)$ is the electric field at the position of the particle $\vec{\mathrm{r}} = \vec{\beta}ct$. The electric field , $\vec{\mathrm{E}}(\vec{\mathrm{r}},t)$ created by this charged particle passing through a non-magnetic dielectric medium can be calculated [54,61] from Maxwell's equations,

$$\begin{aligned} \vec{\nabla}\times\vec{\mathrm{E}} &= -\frac{1}{c}\frac{\partial\vec{\mathrm{B}}}{\partial t}, \qquad \vec{\nabla}\cdot\vec{\mathrm{B}} = 0, \\ \vec{\nabla}\times\vec{\mathrm{B}} &= \frac{1}{c}\frac{\partial\vec{\mathrm{D}}}{\partial t} + \frac{4\pi}{c}\vec{j}, \quad \vec{\nabla}\cdot\vec{\mathrm{D}} = 4\pi\rho. \end{aligned} \tag{4.3}$$

The incident particle with charge ze and velocity $\vec{\beta}c$ gives the source terms, $\rho = ze\delta^3\left(\vec{\mathrm{r}} - \vec{\beta}ct\right)$ and $\vec{j} = \vec{\beta}c\rho$. The problem can be solved by introducing potentials in the Coulomb gauge,

$$\vec{\mathrm{B}} = \vec{\nabla}\times\vec{\mathrm{A}}, \quad \vec{\mathrm{E}} = -\frac{1}{c}\frac{\partial\vec{\mathrm{A}}}{\partial t} - \vec{\nabla}\phi, \quad \vec{\nabla}\cdot\vec{\mathrm{A}} = 0. \tag{4.4}$$

Now Maxwell's equations become,

$$\vec{\nabla}\cdot\left(\epsilon\vec{\nabla}\phi\right) = -4\pi ze\delta^3\left(\vec{\mathrm{r}} - \vec{\beta}ct\right) \tag{4.5}$$

$$-\nabla^2\vec{\mathrm{A}} = -\frac{1}{c^2}\frac{\partial}{\partial t}\left(\epsilon\frac{\partial\vec{\mathrm{A}}}{\partial t}\right) - \frac{1}{c}\frac{\partial}{\partial t}\left(\epsilon\vec{\nabla}\phi\right) + 4\pi ze\vec{\beta}\delta^3\left(\vec{\mathrm{r}} - \vec{\beta}ct\right) \tag{4.6}$$

We can represent the terms in Fourier space for convenience. Now the displacement field $\vec{\mathrm{D}}$ and the magnetic field $\vec{\mathrm{B}}$ can be represented in terms of Fourier integrals as,

$$\vec{\mathrm{D}}\left(\vec{\mathrm{r}},t\right) = \frac{1}{(2\pi)^2}\int d^3k \int d\omega\epsilon\left(\vec{\mathrm{k}},\omega\right)\vec{\mathrm{E}}\left(\vec{\mathrm{k}},\omega\right)e^{\vec{i}\left(\vec{\mathrm{k}}\cdot\vec{\mathrm{r}}-\omega t\right)}$$

$$\vec{\mathrm{B}}\left(\vec{\mathrm{r}},t\right) = \frac{1}{(2\pi)^2}\int d^3k \int d\omega\vec{\mathrm{B}}\left(\vec{\mathrm{k}},\omega\right)e^{\vec{i}\left(\vec{\mathrm{k}}\cdot\vec{\mathrm{r}}-\omega t\right)}$$

The Fourier components of the vector potential $\vec{\mathrm{A}}\left(\vec{\mathrm{k}},\omega\right)$ and scalar potential $\phi\left(\vec{\mathrm{k}},\omega\right)$ can be written as,

$$\phi\left(\vec{\mathrm{k}},\omega\right) = \frac{1}{\epsilon\left(\vec{\mathrm{k}},\omega\right)k^2}2ze\delta\left(\omega - \vec{\mathrm{k}}\cdot\vec{\beta}c\right) \tag{4.7}$$

$$\vec{\mathrm{A}}\left(\vec{\mathrm{k}},\omega\right) = 2ze\frac{\left(-\omega\vec{\mathrm{k}}/k^2c + \vec{\beta}\right)}{\left(k^2 - \epsilon\left(\vec{\mathrm{k}},\omega\right)\omega^2/c^2\right)}\delta\left(\omega - \vec{\mathrm{k}}\cdot\vec{\beta}c\right) \tag{4.8}$$

The electric field created by the charged particle can be obtained as,

$$\vec{\mathrm{E}}\left(\vec{\mathrm{r}},t\right)=\frac{1}{2\pi^2}\int d^3k\int d\omega e^{\vec{i}\left(\vec{\mathrm{k}}\cdot\vec{\mathrm{r}}-\omega t\right)}\left(\frac{\vec{i}\omega}{c}\vec{\mathrm{A}}\left(\vec{\mathrm{k}},\omega\right)-\vec{i\mathrm{k}}\phi\left(\vec{\mathrm{k}},\omega\right)\right) \tag{4.9}$$

Substituting eqn (4.7) and eqn (4.8) in eqn (4.9) we get,

$$\vec{\mathrm{E}}\left(\vec{\mathrm{r}},t\right)=\frac{ize}{2\pi^2}\int d^3k\int d\omega e^{\vec{i}\left(\vec{\mathrm{k}}\cdot\vec{\mathrm{r}}-\omega t\right)}\delta\left(\omega-\vec{\mathrm{k}}\cdot\vec{\beta}c\right)\left(\frac{\frac{\omega^2}{k^2c^2}\vec{\mathrm{k}}-\frac{\omega}{c}\vec{\beta}}{-k^2+\epsilon\left(\vec{\mathrm{k}},\omega\right)\omega^2/c^2}-\frac{\vec{\mathrm{k}}}{k^2\epsilon\left(\vec{\mathrm{k}},\omega\right)}\right) \tag{4.10}$$

The mean energy loss of the particle is obtained by substituting eqn (4.10) in eqn (4.2),

$$\left\langle\frac{dE}{dx}\right\rangle=\frac{z^2e^2i}{\beta2\pi^2}\int\int\left[\frac{\frac{\omega}{c}\left(\frac{\omega\vec{\mathrm{k}}\cdot\vec{\beta}}{k^2}-\beta^2\right)}{\left(-k^2+\frac{\epsilon\omega^2}{c^2}\right)}-\frac{\vec{\mathrm{k}}\cdot\vec{\beta}}{k^2\epsilon}\right]\delta\left(\omega-\vec{\mathrm{k}}\cdot\vec{\beta}c\right)e^{i\left(\vec{\mathrm{k}}\cdot\vec{\beta}c-\omega\right)t}d^3kd\omega \tag{4.11}$$

Now taking d^3k as $2\pi k^2dkd(\cos\psi)$ in spherical coordinates and integrating over $\cos\psi$ we get,

$$\left\langle\frac{dE}{dx}\right\rangle=\frac{iz^2e^2}{\beta2\pi^2}\int_{-\infty}^{\infty}\int_{\frac{\omega}{\beta c}}^{\infty}dk\left[\frac{k\omega\left(\beta^2-\frac{\omega^2}{k^2c^2}\right)}{-k^2c^2+\epsilon\left(k,\omega\right)\omega^2}-\frac{\omega}{kc^2\epsilon\left(k,\omega\right)}\right] \tag{4.12}$$

Since the above integration is over both positive and negative frequencies, we limit ω to positive frequencies by using $\epsilon\left(-\omega\right)=\epsilon^*\left(\omega\right)$,

$$\begin{aligned}\left\langle\frac{dE}{dx}\right\rangle &= -\frac{2z^2e^2}{\beta^2\pi}\int_0^{\infty}\int_{\frac{\omega}{\beta c}}^{\infty}dk\left[\omega k\left(\beta^2-\frac{\omega^2}{k^2c^2}\right)\mathrm{Im}\left(\frac{1}{-k^2c^2+\epsilon\left(k,\omega\right)\omega^2}\right)\right.\\ &\left.+\frac{\omega}{kc^2}\mathrm{Im}\left(\frac{-1}{\epsilon\left(k,\omega\right)}\right)\right]\end{aligned} \tag{4.13}$$

4.1.2 Photo Absorption Ionization (PAI) Model

The Photo Absorpton and Ionization (PAI) Model was developed by Allison and Cobb [54] in 1980. This model is based on the measured photoabsorption cross section, $\sigma_\gamma\left(\omega\right)$ for a medium with electron density, N and atomic charge, Z.

$$\sigma_\gamma\left(\omega\right)=\frac{Z\omega}{Nc}\epsilon_2\left(k,\omega\right) \tag{4.14}$$

The photoabsorption cross section is directly related to $\epsilon_2(k,\omega)$ which comes from the complex dielectric constant of the medium,

$$\epsilon(k,\omega) = \epsilon_1(k,\omega) + i\epsilon_2(k,\omega). \tag{4.15}$$

Here, the real part of eqn (4.15) ($\epsilon_1(k,\omega)$) describes polarization and the imaginary part ($\epsilon_2(k,\omega)$) describes the absorptive properties of the medium. The imaginary part of the complex dielectric constant, $\epsilon_2(k,\omega)$ can be expressed in terms of the generalized oscillator strength density, $f(k,\omega)$

$$\epsilon_2(k,\omega) = \frac{2\pi^2 N e^2}{m\omega} f(k,\omega) \tag{4.16}$$

where m is the mass of the electron. The function $f(k,\omega)$ describes the coupling of the electrons to the field of the atom. In the resonance region below the free electron line (see reference [54,59]), $f(k,\omega)$ is independent of wave number k and is given in terms of photoabsorption cross section, $\sigma_\gamma(\omega)$.

$$f(k,\omega) = \frac{mc}{2\pi^2 e^2 Z}\sigma_\gamma(\omega) \tag{4.17}$$

$\sigma_\gamma(\omega)$ can be measured experimentally. The photoabsorption cross-section of argon and sulphur hexaflouride as function of photon energy are given in Figs. 4.1 and 4.2 respectively. The total oscillator strength in the resonance region is given by,

$$\int_{res} f(k,\omega)\, d\omega = \frac{mc}{2\pi^2 e^2 Z}\int_{\hbar k^2/2m}^{\infty} \sigma_\gamma(\omega)\, d\omega \tag{4.18}$$

On the free electron-line, we take a δ function which represents point-like scattering in the absorption. Ignoring Fermi motion of bound electrons, the oscillator strength can now be written as,

$$f(k,\omega) = \frac{mc}{2\pi^2 e^2 Z}\delta\left(\omega - \frac{\hbar k^2}{2m}\right)\int_0^{\omega} \sigma_\gamma(\omega')\, d\omega' \tag{4.19}$$

The normalized photoabsorption cross section in the above equation satisfies Thomas-Reiche-Kuhn sum rule,

$$\int_0^{\infty} \sigma_\gamma(\omega)\, d\omega = \frac{2\pi^2 e^2 Z}{mc} \tag{4.20}$$

Here we extend the $\epsilon(k,\omega)$ to the kinematic domain of energy $E = \hbar\omega$ and momentum $p = \hbar k$ which is exchanged between the moving particle and the medium. For small k below the free-electron line we can take,

$$\epsilon(k,\omega) = \epsilon(\omega) \tag{4.21}$$

The real and imaginary parts of the complex dielectric constant are related through the Kramers-Kronig relation,

$$\epsilon_1(k,\omega) - 1 = \frac{2}{\pi} P \int_0^\infty \frac{x\epsilon_2(x)}{x^2 - \omega^2} dx \tag{4.22}$$

Where P is the principal value. Now we can integrate eqn (4.13) over k for calculating $\left\langle \frac{dE}{dx} \right\rangle$

$$\begin{aligned}\left\langle \frac{dE}{dx} \right\rangle = & -\int_0^\infty d\omega \frac{e^2}{\beta^2 c^2 \pi} \left[\frac{Nc}{Z} \sigma_\gamma(\omega) ln \left[\left(1 - \beta^2 \epsilon_1\right)^2 + \beta^4 \epsilon_2^2 \right]^{1/2} + \right. \\ & \left. \frac{Nc}{Z} \sigma_\gamma(\omega) ln \left(\frac{2m\beta^2 c^2}{\hbar\omega} \right) + \omega \left(\beta^2 - \frac{\epsilon_1}{|\epsilon|^2} \right) \Theta + \frac{1}{\omega} \int_0^\omega \frac{\sigma_\gamma(\omega')}{Z} d\omega' \right]\end{aligned} \tag{4.23}$$

where $\Theta = arg\left(1 - \epsilon_1\beta^2 + i\epsilon_2\beta^2\right)$. The energy loss happens through a number of discrete collisions with energy $E = \hbar\omega$. Hence, the average energy loss is the product of the mean energy, E and the collision probability per unit path which is again the cross-section times the density, N. Therefore, eqn (4.23) can be written as,

$$\left\langle \frac{dE}{dx} \right\rangle = \int_0^\infty EN \frac{d\sigma}{dE} \hbar d\omega \tag{4.24}$$

The differential cross section per electron per unit energy loss is,

$$\begin{aligned}\frac{d\sigma}{dE} = & \frac{\alpha}{\beta^2\pi} \frac{\sigma_\gamma(E)}{EZ} ln \left[\left(1 - \beta^2\epsilon_1\right)^2 + \beta^4\epsilon_2^2 \right]^{-1/2} + \frac{\alpha}{\beta^2\pi} \frac{1}{N\hbar c} \left(\beta^2 - \frac{\epsilon_1}{|\epsilon|^2} \right) \Theta \\ & + \frac{\alpha}{\beta^2\pi} \frac{\sigma_\gamma(E)}{EZ} ln \left(\frac{2mc^2\beta^2}{E} \right) + \frac{\alpha}{\beta^2\pi} \frac{1}{E^2} \int_0^E \frac{\sigma_\gamma(E')}{Z} dE'\end{aligned} \tag{4.25}$$

where α is the fine structure constant. The first two terms of eqn (4.25) come from the magnetic vector potential term of the Coulomb gauge where the electric field is transverse to the direction of momentum transfer. Hence, the first two terms are termed as the transverse cross-section. Whereas the third and fourth terms of the same equation are called the longitudinal cross section since they come from the electrostatic term in the Coulomb gauge where the electric field is parallel to the momentum transfer. The fourth term of eqn (4.25) represents the Rutherford scattering cross-section at high energies greater than the binding energy of the atomic shell that absorbs the photon. From eqn (4.20) and eqn (4.23) we get [59]

$$\frac{d\sigma}{dE} \to \frac{2\pi r_e^2 mc^2}{\beta^2 E^2} \tag{4.26}$$

where $r_e = e^2/mc^2$ is the classical electron radius.

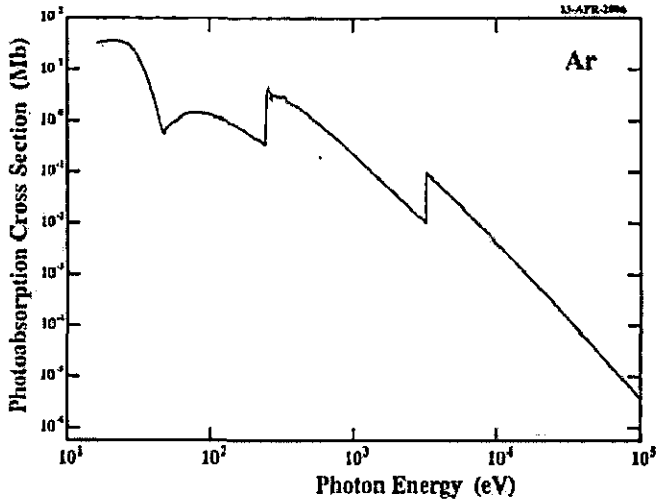

Figure 4.1: Measured photoabsorption cross sections for Argon [62].

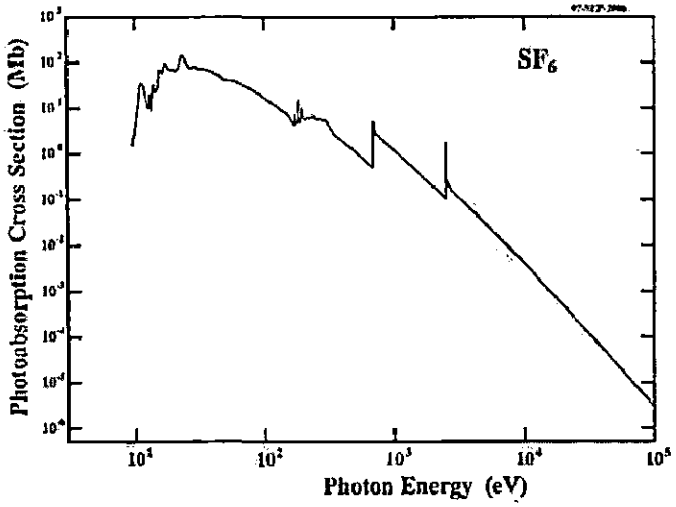

Figure 4.2: Measured photoabsorption cross sections for SF_6 [62].

4.1.3 Simulation with HEED

HEED ("High Energy Electrodynamics") [53] written by I. Smirnov is a Monte-Carlo Simulation package based on the photo-absorption ionization model (PAI) of W.W.M. Allison and J.H. Cobb [54] that we discussed in section 4.1.2. This program can calculate the energy loss of a moving charged particle. The HEED program also includes the modified version of PAI, called the photo absorption ionization and relaxation (PAIR) model which considers the cross-sections of individual shells.

The HEED program calculates the primary ionization parameters by simulating the atomic relaxation effects (by the emission of fluorescence photons and Auger electrons) and by tracking the emerging δ-electrons. It can simulate the ionization effects such as the cluster density, the primary electron distribution etc. inside the gas chamber.

4.1.4 Simulation with Geant4

Geant4 simulation package is used for simulating the interactions of particles in matter [63]. It has got wide applications in high energy physics, astrophysics and space science, medical physics and radiation protection. The Geant4 program is a complete simulation package and within this we can define the geometry of the detector, various physics processes, tracking and visualization. The physics processes defined in the Geant4 program include the standard electromagnetic, low energy electromagnetic, hadronic and optical processes. The interactions of particles cover a wider energy range from 250 eV to 1 TeV. The Geant4 Low Energy Electromagnetic Physics can even model the electromagnetic interactions of photons, electrons, hadrons and ions with matter down to very low energies of a few eV scale. The different steps involved in the Geant4 simulation process are the following:

- define the geometry of the experiment.
- define various materials to be used.
- specify the kind of primary particles (its PID, momenta, direction etc)to be used in the run.
- define the external electromagnetic fields.
- define the physics processes governing the particle interactions.
- specify the sensitive detector components.
- generate, track and store event data.
- visualize the detector and particle trajectories.

Fig.4.3 shows the Geant4 class category diagram [64] in which the class files are organized into 17 major class categories. Using this wide collection of library classes, users can build their own applications. Any application program can be derived from three abstract base classes given by the Geant4 program namely: G4VUserDetectorConstruction, G4VUserPhysicsList and G4VUserPrimaryGeneratorAction These three base classes are registered with the class G4RunManager which controls the entire program. The geometry of the detector, materials, scoring regions

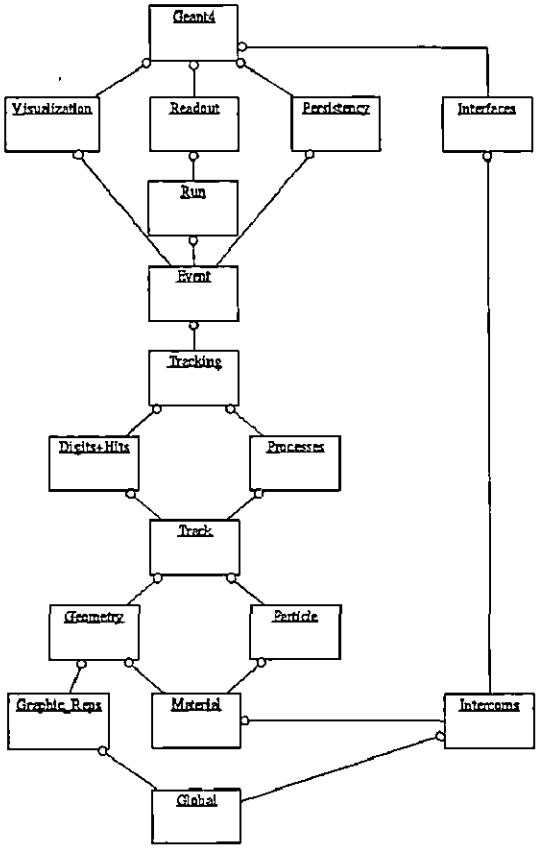

Figure 4.3: Geant4 class category

and visualization attributes are defined in the class G4VUser DetectorConstruction. The physics processes for particular particle interactions, production cuts of photons, electrons and positrons are derived from the class G4VUserPhysicsList, whereas the primary particles, their energy, direction etc are defined from the class G4VUserPrimaryGeneratorAction. The five Geant4 base classes whose methods are used at different stages of simulations are described as,

G4UserRunAction: invoked at the beginning and at the end of simulation.

G4UserEventAction: invoked at the beginning and at the end of each particle history.

G4UserStackingAction: invoked at the start of each history when a new track is pushed onto the stack.

G4UserTrackingAction: invoked at the beginning and at the end of each particle trajectory.

G4UserSteppingAction: invoked at the end of each step.

4.1.4.1 Geant4 physics process for photons and electrons

We used various physics processes which are defined in the Geant4 program for simulating the electromagnetic interactions of photons and electrons in Resistive Plate Chamber. The processes include mainly the PAI (photo-absorption ionization model), the Standard EM processes, the Penelope and the Livermore EM processes. Though our main concern is the interactions of the minimum ionizing particle in the sensitive detector, all the low energy processes are also included. The physics processes which are based on various physics models are discussed below:

Standard EM processes

The Standard EM processes cover an energy range upto the order of 100 TeV. The physics processes include the Cerenkov effect, the transition radiation and the scintillation. The Photon processes include the Compton scattering which is defined in the Geant4 class G4ComptonScattering, the gamma conversion or pair production is defined in the class G4GammaConversion and the Photo-electric effect is defined in the class G4PhotoElectricEffect. The electron or positron processes are Bremsstrahlung which are defined in G4eBremsstrahlung class , the Ionization and delta ray production are defined in the G4eIonisation and the positron annihilation are defined in the class G4eplusAnnihilation. Many of these processes have already been discussed in detail in the second chapter of the thesis.

Livermore EM processes

The low energy physics processes are applicable for an energy range from 250 eV to 100 GeV [65]. The data tables are from Lawrence Livermore National Laboratory (LLNL) which include Evaluated Atomic Data Library (EADL),Evaluated Electrons Data Library (EEDL) and Evaluated Photons Data Library (EPDL97).

Penelope EM processes

The low energy electromagnetic models based on the PENELOPE (PENetration and Energy LOss of Positrons and Electrons) can cover an energy range from 250 eV to 1 GeV [66,67].

4.1.5 Comparison of HEED and Geant4 Results

We used the HEED and Geant4 packages to calculate the distributions of electrons produced by the interactions of muons of energy 100 GeV in a 2 mm gap RPC for two different gas combinations. While calculating primary electrons produced in the

Geant4 program, we filled the histogram only with the non-zero events. This is to avoid shifting of the histogram origin to the zero value. Fig. 4.4 shows the distribution of the electrons for the gas mixture, $C_2H_2F_4/C_4H_{10}/SF_6$ in the proportion 95.4:4.5:0.1 and $Ar/C_4H_{10}/C_2H_2F_4$ in the proportion 76.0:4.0:20.0 respectively. It is clear from Fig. 4.4(a) and Fig. 4.4(b) that the HEED and Geant4 program results are comparable. The Geant4 program includes a number of low energy physics processes (see section 4.1.4) that the HEED program does not. Since our interest is in the interactions triggered by a relativistic particle, the low energy processes can be ignored. The Geant4 program includes the Photo Absorption Ionization Model (PAI) model [68](discussed in section 4.1.2) like the HEED program [53]. The number of electrons produced at an interaction point when a high energy particle passes through the detector are grouped as clusters and the clusters calculated with the Geant4 program for different gas mixtures are shown in Fig. 4.5. Fig. 4.5(a) shows the cluster distribution for a gas mixture $C_2H_2F_4/C_4H_{10}/SF_6$ in the proportion 95.4:4.5:0.1. From this figure, the mean value of clusters comes out to be 21.45. The cluster density calculated with the HEED program for the same gas mixture is 9.54 mm^{-1} and from this value we can calculate total number of clusters in a 2 mm gas gap as 19.09 which is matching well with the Geant4 result. Similarly for the gas mixture $Ar/C_4H_{10}/C_2H_2F_4$ in the proportion 76.0:4.0:20.0, the values calculated from the Geant4 and HEED programs are 9.71 (see Fig. 4.5(b)) and 10.05 respectively. The average number of clusters per mm for different incident energies of the primary particle calculated with the HEED and Geant4 programs are shown in Fig.4.6 for different gas combinations. Also Fig.4.7 shows the number of electrons per cluster. The computational time needed for the Geant4 program is more compared to the HEED program. The coding is easier in the HEED program and the user need to call only the specific functions in his code. While in the Geant4 program, the user has to decide and specify the physics processes valid for the required energy range in his code. In spite of all these complexities, the Geant4 program has got a wider applicability since we can construct any complex detector geometries using this program.

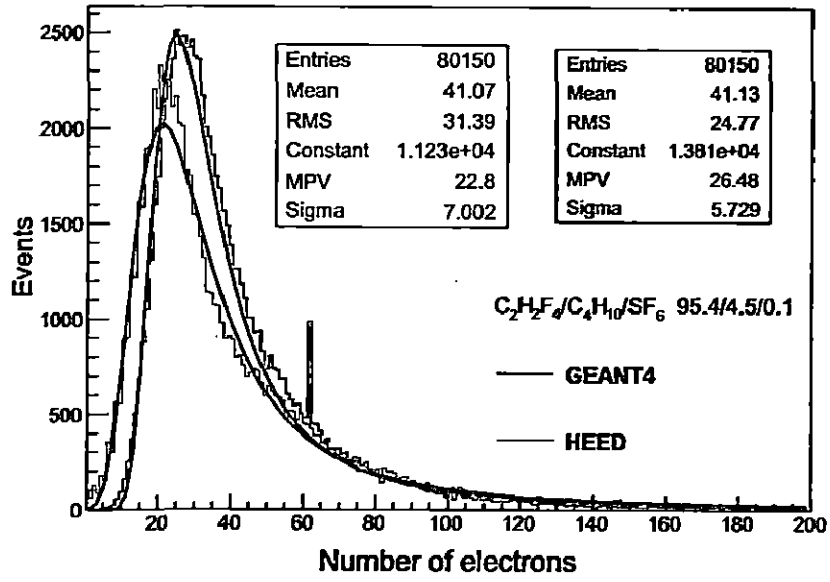

(a)

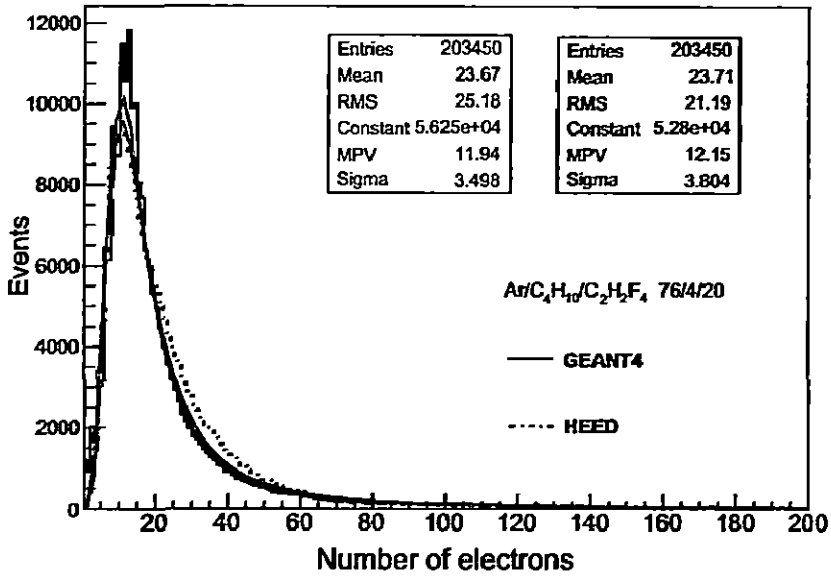

(b)

Figure 4.4: Electron distribution in gas mixtures (a) $C_2H_2F_4/C_4H_{10}/SF_6$ in the proportion 95.4:4.5:0.1 and (b)$Ar/C_4H_{10}/C_2H_2F_4$ in the proportion 76.0:4.0:20.0, when a muon of energy 100 GeV passed through the RPC chamber kept at T= 20°C and P=760 Torr. The red lines represent the landau fit.

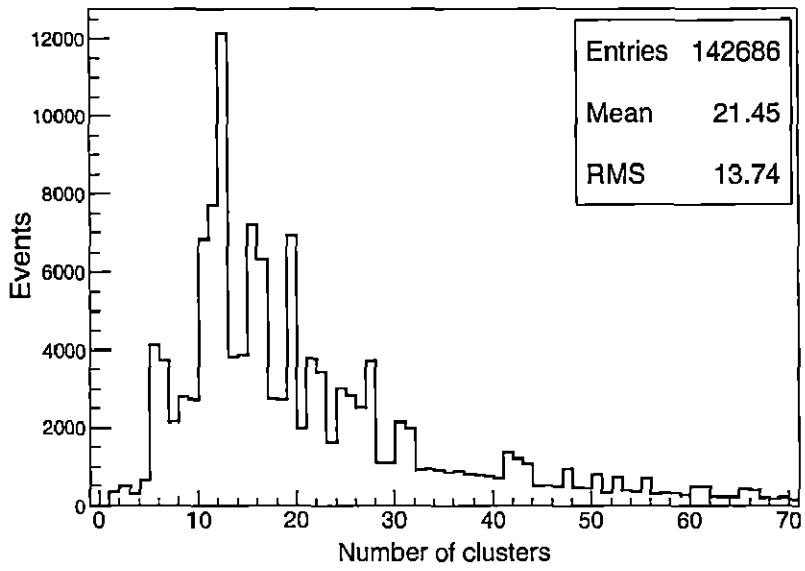

(a)

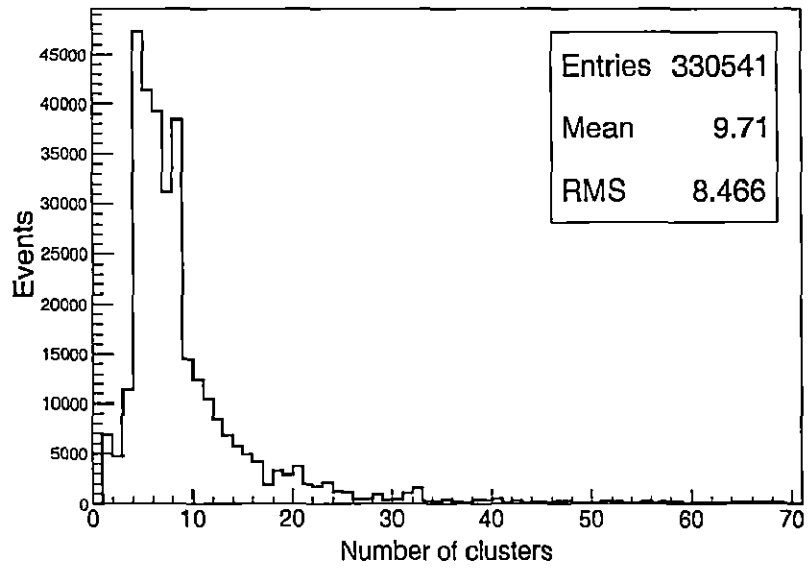

(b)

Figure 4.5: Cluster distribution for the gas mixtures (a) isobutane, freon and SF_6 in the ratio 95.4:4.5:0.1 and (b) argon, isobutane and freon in the ratio 76.0:4.0:20.0, when a muon of energy 100 GeV passed through the RPC chamber kept at T= 20°C and P=760 Torr.

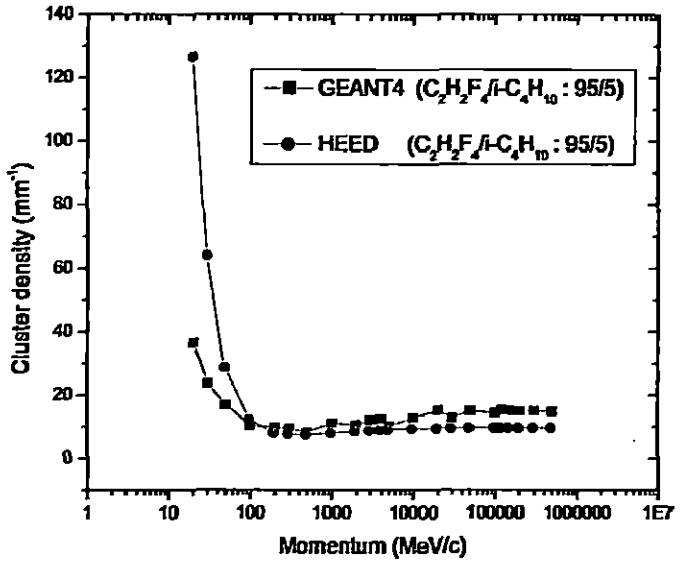

(a)

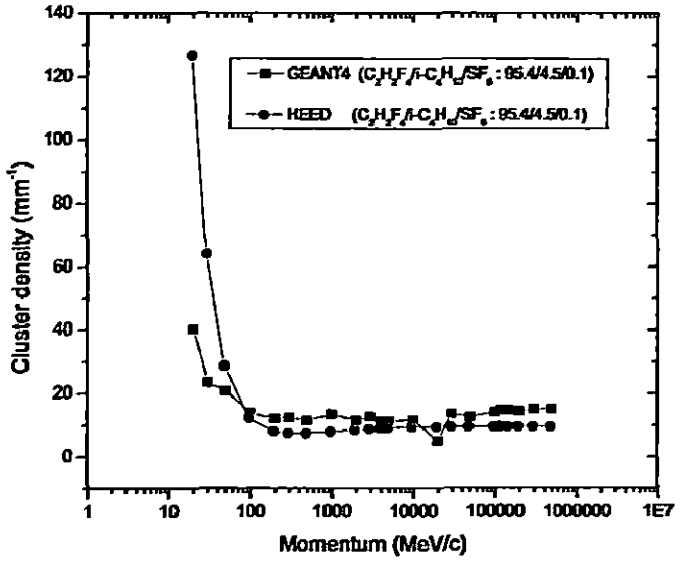

(b)

Figure 4.6: Cluster density for different gas mixtures (a) freon and isobutane in the ratio 95.0:5.0 and (b) isobutane, freon and SF_6 in the ratio 95.4:4.5:0.1, when a muon of different energies passed through the RPC chamber kept at T= 20°C and P=760. Torr.

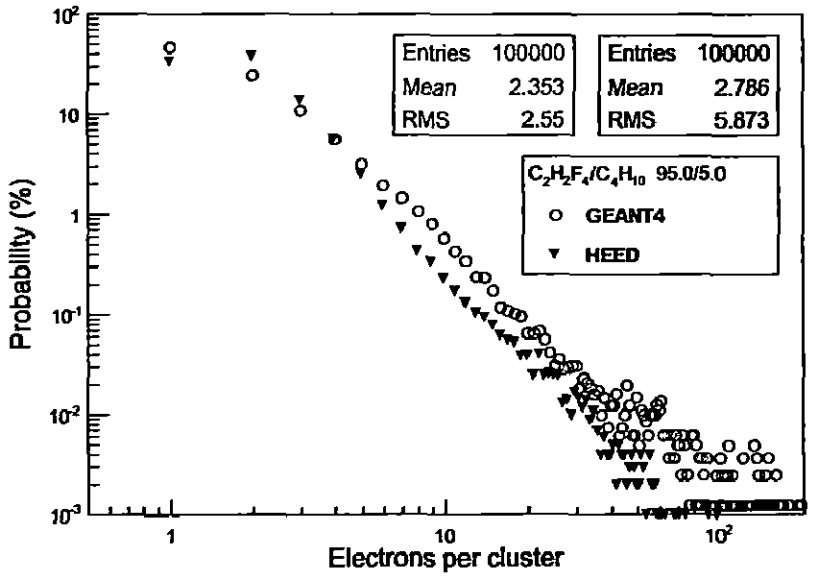

(a)

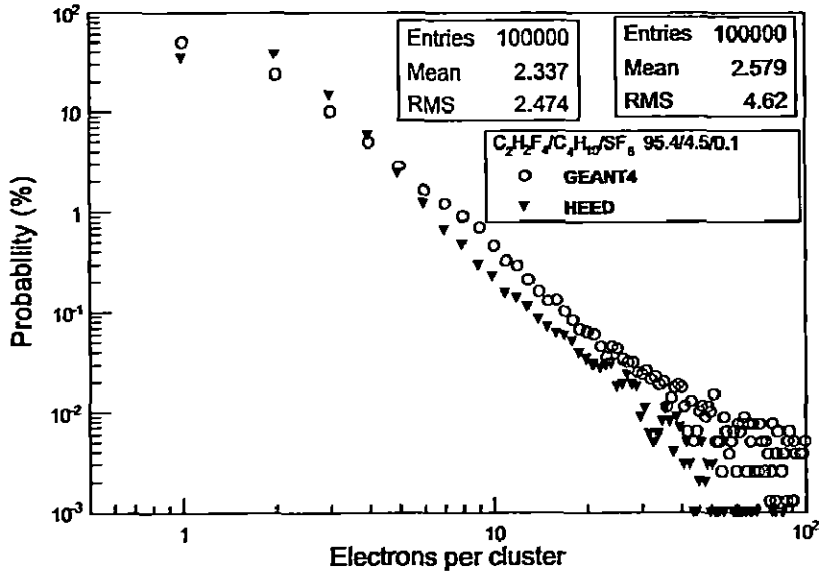

(b)

Figure 4.7: Cluster size distribution for different gas mixtures (a) freon and isobutane in the ratio 95.0:5.0 and (b) freon, isobutane and SF_6 in the ratio 95.4:4.5:0.1, when a muon of energy 100 GeV passed through the RPC chamber kept at T= 20°C and P=760 Torr.

4.2 Electric Field

There are various methods for solving the electromagnetic field configuration of particular detector geometries. Other than the three-dimensional (3D) field solvers, the two-dimensional simple (2D) analytical models like Conformal Mapping for computing the weighting fields and potentials by approximating electrode configuration in the Resistive Plate Chambers have also been reported [69]. However, these models are not applicable to the realistic and complicated detector geometries. The commonly followed 3D field solvers include the Finite Difference Method (FDM), the Finite Element Method (FEM). The Boundary Element Method which is also termed as the surface charge method is another interesting approach that is known to be accurate and warrants attention. In the following sections we briefly describe these field solvers.

4.2.1 Finite Difference Method

The Finite Difference Method (FDM) is a tool for solving the partial differential equation (PDE) numerically. The FDM discretizes the domain of interest into small grids and then computes approximate solutions for this grid. Finally, the derivatives in the equation are replaced using the differential quotients. The error between the numerical solution and the exact solution is determined by the error that is occurred while moving from a differential operator to a difference operator. The discretization error can be reduced by making the meshing more accurate.

4.2.2 Finite Element Method

In the Finite Element Method (FEM) method, an electrostatic problem can be formulated using a second order partial differential equation (PDE) in the computational domain, Ω. We then apply the boundary conditions (BC) on the boundary of the domain. The entire physical system/device to be analyzed is devided into smaller grids/cells (discretization or meshing). Then it solves the Laplace's equation at nodal points of the volume elements created after discretizing the detector volume. The solution of potential obtained at nodal points is interpolated/extrapolated following a polynomial of normally low order to get the solution at non-nodal points. Each finite element mesh will have a simple approximation of the solution. Finally, the elements with local approximate solution are assembled together to solve the system of equations. Fig. 4.8 shows the various steps involved in the FEM for solving a problem. The governing equations for calculating the electric field distribution in the RPC can be derived from Maxwell's equations.

$$\vec{\nabla} \times \vec{E} = 0 \tag{4.27}$$

$$\vec{\nabla} \cdot \vec{D} = \rho \tag{4.28}$$

$$\vec{D} = \epsilon \vec{E} \tag{4.29}$$

Following eqn. (4.27), we can represent $\vec{E}$ as a gradient of scalar potential, $\vec{\phi}$

$$\vec{E} = -\vec{\nabla}\vec{\phi} \tag{4.30}$$

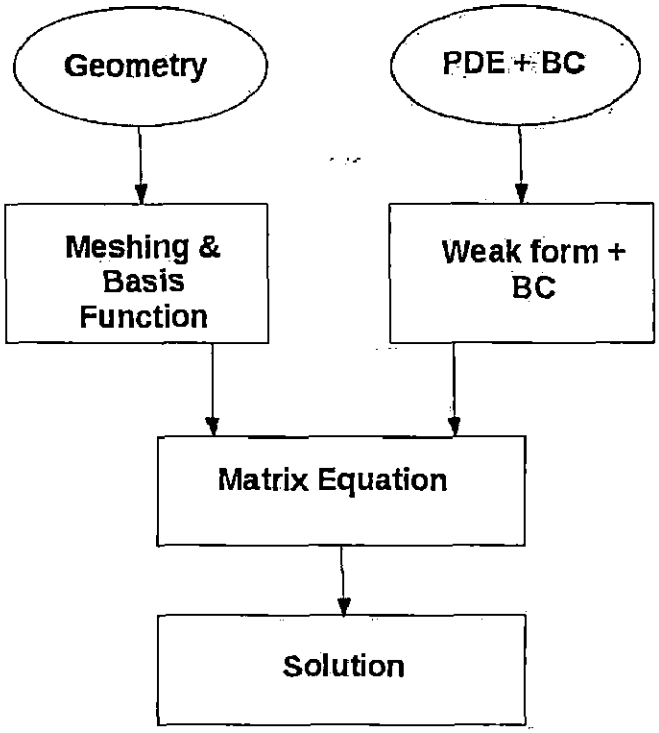

Figure 4.8: Flow diagram of processes involved in FEM.

Now from eqn. (4.28), eqn. (4.29) and eqn. (4.30) we get,

$$\vec{\nabla} \cdot (\epsilon \vec{\nabla}\vec{\phi}) = -\rho \tag{4.31}$$

On the boundaries we specify two kinds of boundary conditions,

↬ **Drichlet boundary condition:** Value of the potential,

$$\phi = V \tag{4.32}$$

↬ **Neumann boundary condition:** The normal derivative of the potential,

$$\frac{\partial \phi}{\partial n} = 0 \tag{4.33}$$

In order to find the weak form of the given problem, we multiply eqn. (4.31) with a test function, v and integrate over the computational domain, Ω

$$\int_{\Omega} \left(\vec{\nabla} \cdot (\epsilon \vec{\nabla} \vec{\phi}) \right) v d\Omega = - \int_{\Omega} \rho v d\Omega \tag{4.34}$$

Integrating by parts we get,

$$\int_{\Omega} \vec{\nabla} \cdot (\epsilon \vec{\nabla} \vec{\phi} v) d\Omega - \int_{\Omega} \epsilon \vec{\nabla} \vec{\phi} \cdot \vec{\nabla} v d\Omega = - \int_{\Omega} \rho v d\Omega \tag{4.35}$$

Using the divergence theorem and also taking the test function v=0, on the Drichlet boundary, the eqn. (4.35) can be written as,

$$\int_{\Omega} \epsilon \vec{\nabla} \vec{\phi} \cdot \vec{\nabla} v d\Omega = \int_{S} \epsilon v \frac{\partial \phi}{\partial n} dS + \int_{\Omega} \rho v d\Omega \tag{4.36}$$

Now we take an approximation to the test function, v and the scalar potential, ϕ

$$v = \sum_{i=1}^{n} v_i N_i \tag{4.37}$$

$$\phi = \sum_{j=1}^{n} \phi_j N_j \tag{4.38}$$

Here n are the number of nodes and N_i are the shape functions. Substituting eqn. (4.37) and eqn. (4.38) in eqn. (4.36),

$$\sum_{i=1}^{n} \sum_{j=1}^{n} \left(\int_{\Omega} \epsilon \left(\vec{\nabla} N_i \right)^T \vec{\nabla} N_j d\Omega \phi_j - \int_{\Omega} N_i \rho d\Omega - \int_{S} \epsilon N_i \frac{\partial \phi}{\partial n} dS \right) = 0 \tag{4.39}$$

The eqn. (4.39) can now be written in matrix form as,

$$\vec{K} \phi = \vec{h} \tag{4.40}$$

Here, $\vec{K} = \sum_{p=1}^{P} k_{ij}^q$ where $k_{ij}^q = \int_{\Omega} \epsilon \left(\vec{\nabla} N_i \cdot \vec{\nabla} N_j \right) d\Omega$,

$\vec{h} = \sum_{p=1}^{P} h_{ij}^q$ where $h_{ij}^q = \int_{\Omega} N_i \rho d\Omega + \int_{S} \epsilon N_i \frac{\partial \phi}{\partial n} dS$ and $\phi = (\phi_1, \phi_2, ..., \phi_n)^T$

$\vec{K}$, $\vec{h}$ are the global stiffness matrix and the residual vector respectively. Similarly, k_{ij} and h_{ij} are the elemental stiffness matrix and the residual vector respectively. Here, P represents the elements in the global mesh.

4.2.3 Boundary Element Method

The Boundary Element Method (BEM) discretizes the device surface or boundaries into small elements carrying unknown charge distribution. The BEM solves for the charge distribution on the boundary elements following the Green function technique. It involves solving boundary integral equation obtained from the solution of the Poisson equation by numerically evaluating the potential or field as an effect of charge distribution accumulated over boundaries or material surfaces as a result of applying certain potential to the detector. The potential and field at any point in the device can be determined accurately by knowing the charge density distribution using the same Green function approach.

The main advantage of the BEM over other methods like the FEM is the reduced dimensionality of the problem in the BEM. Both the FDM and the FEM need the entire domain and the boundaries of the device to be discretized for computing the solution while the numerical discretization for the BEM is needed only at the interfaces or boundaries. The primary step of the BEM technique is to discretize the boundaries and surfaces of a given problem. The elements resulting out of the discretization process are normally rectangular or triangular though elements of other shapes are also used. The next step is to find out the charge distribution on the elements that satisfies eqn. (4.41) following the given boundary conditions.

$$\phi(\vec{r}) = \int_{vol} G(\vec{r}, \vec{r}')\rho(\vec{r}')dv' \tag{4.41}$$

In the above equation, $\phi(\vec{r})$ is the potential at a point r in space and $\rho(\vec{r})$ is the charge density at an infinitesimally small volume dv placed at r. The problem is, generally, to find $\rho(\vec{r})$ as a function of space, resulting the known distribution of $\phi(\vec{r})$. Since the potentials on the surface elements are known from the given potential configuration, eqn. (4.41) can be used to generate algebraic expressions relating unknown charge densities and potentials at the centroid of the elements. One unique equation can be obtained for each centroid considering influences of all other elements including self influence and thus the same number of equations can be generated as there are unknowns. In matrix form, the resulting system of simultaneous linear algebraic set of equations can be written as follows,

$$\vec{K} \cdot \rho = \phi \tag{4.42}$$

where $\vec{K}$ is the matrix consisting of influences among the elements due to unit charge density on each of them, ρ represents a column vector of unknown charge densities at the centroids of the elements and ϕ represents known values of potentials at the centroids of these elements. Each element of this influence coefficient or capacity coefficient matrix, $\vec{K}$ is a direct evaluation of an equation similar to the equation which represents the effect of a single element on a boundary/surface (obtained through discretization) on a point where a boundary condition of a given problem

is known. While, in general, this should necessitate an integration of the Green function over the area of the element, this integration is avoided in most of the BEM solvers through the assumption of nodal concentration of singularities with known basis function. Since the right hand side is known, in principle, it is possible to solve the system of algebraic equations and obtain the surface charge density on each of the element used to describe the conducting surfaces of the detector following

$$\rho = \vec{K}^{-1} \cdot \phi \tag{4.43}$$

Once the charge distribution on the boundaries and all the surfaces are known, the potential and field at any point in the computational domain can be obtained using eqn. (4.41) and its derivative.

Usual BEM suffers from several drawbacks that have resulted in its relative lack of popularity. Two of the most important ones are mentioned as follows: (i) It is assumed that a surface distribution of the charge density on an element can be represented by a nodal arrangement based on a chosen basis function. (ii) It is assumed that the satisfaction of the boundary condition at a predetermined point (or, through the use of known shape functions) is equivalent to satisfying the same on the whole element in a distributed manner. The former assumption leads to infamous numerical boundary layer due to which the near-field solution in the regions close to an element becomes erroneous. Thus the estimation of potential and field in the near-field regions close to the boundaries and surfaces by the usual BEM is found to be inaccurate.

4.2.4 nearly exact Boundary Element Method (neBEM)

The above problem, faced by the BEM has been resolved to a great extent through the development of the neBEM [55–57] solver that uses exact integration of the Green function and its derivative in its formulation. These integrations for rectangular and triangular elements having uniform charge density have been obtained as the closed-form analytical expressions using the symbolic mathematics. Thus they account for the truly distributed nature of the charge density on a given element. The major advantage achieved through the use of the proposed closed-form expressions is that the accuracy is enhanced throughout the physical domain including the near-field region without using any special formulation in any part of the domain.

In order to estimate the potential and field in composite systems containing the dielectric material, the above formulations have been extended. In the process, the integral equations representing potential due to the total charge distribution on conductor-to-dielectric (CD) interfaces and the polarization charge distribution (that are assumed to have attained steady state values) on the dielectric-to-dielectric (DD) interfaces are used in conjunction with proper boundary conditions on these interfaces.

It should also be noted that the neBEM solver is also capable of estimating the effects of floating conductors as and when necessary.

In the neBEM approach, the integrations for evaluating influences (both potential and flux) due to the rectangular and triangular elements having uniform charge density have been obtained as the closed-form analytic expressions [55–57]. The potential ϕ at a point (X, Y, Z) in free space due to a uniform source distributed on a rectangular flat surface with corners situated at $(x_1, 0, z_1)$ and $(x_2, 0, z_2)$ as shown in Fig. 4.9 is known to be a multiple of

$$\phi(X,Y,Z) = \int_{z_1}^{z_2}\int_{x_1}^{x_2} \frac{dxdz}{\sqrt{(X-x)^2+Y^2+(Z-z)^2}} \tag{4.44}$$

where the multiple depends upon the strength of the source and other physical considerations. The closed-form analytic expressions for $\phi(X, Y, Z)$ is given as:

$$\begin{aligned}
\phi(X,Y,Z) = \frac{1}{2}\Bigg(& 2Zln\left(\frac{D_2-(X-x_1)}{D_1-(X-x_1)}\right) + 2Zln\left(\frac{D_3-(X-x_2)}{D_4-(X-x_2)}\right) \\
& +2x_1 ln\left(\frac{D_1-(Z-z_1)}{D_2-(Z-z_1)}\right) + 2x_2 ln\left(\frac{D_4-(Z-z_2)}{D_3-(Z-z_1)}\right) \\
& +2z_1 ln\left(\frac{D_1-(X-x_1)}{D_3-(X-x_2)}\right) + 2z_2 ln\left(\frac{D_4-(X-x_2)}{D_2-(X-x_1)}\right) \\
& -S_1(X+i|Y|)\tanh^{-1}\left(\frac{R_1-iI_1}{D_1|Z-z_1}\right) - S_1(X-i|Y|)\tanh^{-1}\left(\frac{R_1+iI_1}{D_1|Z-z_1}\right) \\
& +S_2(X+i|Y|)\tanh^{-1}\left(\frac{R_2-iI_1}{D_2|Z-z_2}\right) + S_2(X-i|Y|)\tanh^{-1}\left(\frac{R_2+iI_1}{D_2|Z-z_2}\right) \\
& +S_1(X+i|Y|)\tanh^{-1}\left(\frac{R_1-iI_2}{D_3|Z-z_1}\right) + S_1(X-i|Y|)\tanh^{-1}\left(\frac{R_1+iI_2}{D_3|Z-z_1}\right) \\
& -S_2(X+i|Y|)\tanh^{-1}\left(\frac{R_2-iI_2}{D_4|Z-z_2}\right) - S_2(X-i|Y|)\tanh^{-1}\left(\frac{R_2+iI_2}{D_4|Z-z_2}\right)\Bigg) \\
& -2\pi Y
\end{aligned} \tag{4.45}$$

where,

$$D_1 = \sqrt{(X-x_1)^2+Y^2+(Z-z_1)^2} \quad D_2 = \sqrt{(X-x_1)^2+Y^2+(Z-z_2)^2}$$

$$D_3 = \sqrt{(X-x_2)^2+Y^2+(Z-z_1)^2} \quad D_4 = \sqrt{(X-x_2)^2+Y^2+(Z-z_2)^2}$$

$$R_1 = Y^2+(Z-z_1)^2 \quad R_2 = Y^2+(Z-z_2)^2$$

$$I_1 = (X - x_1)\,|Y| \quad I_2 = (X - x_2)\,|Y|$$

$$S_1 = sign\,(z_1 - Z) \quad S_2 = sign\,(z_2 - Z)$$

In a similar way, the electrostatic field can be represented as a multiple of

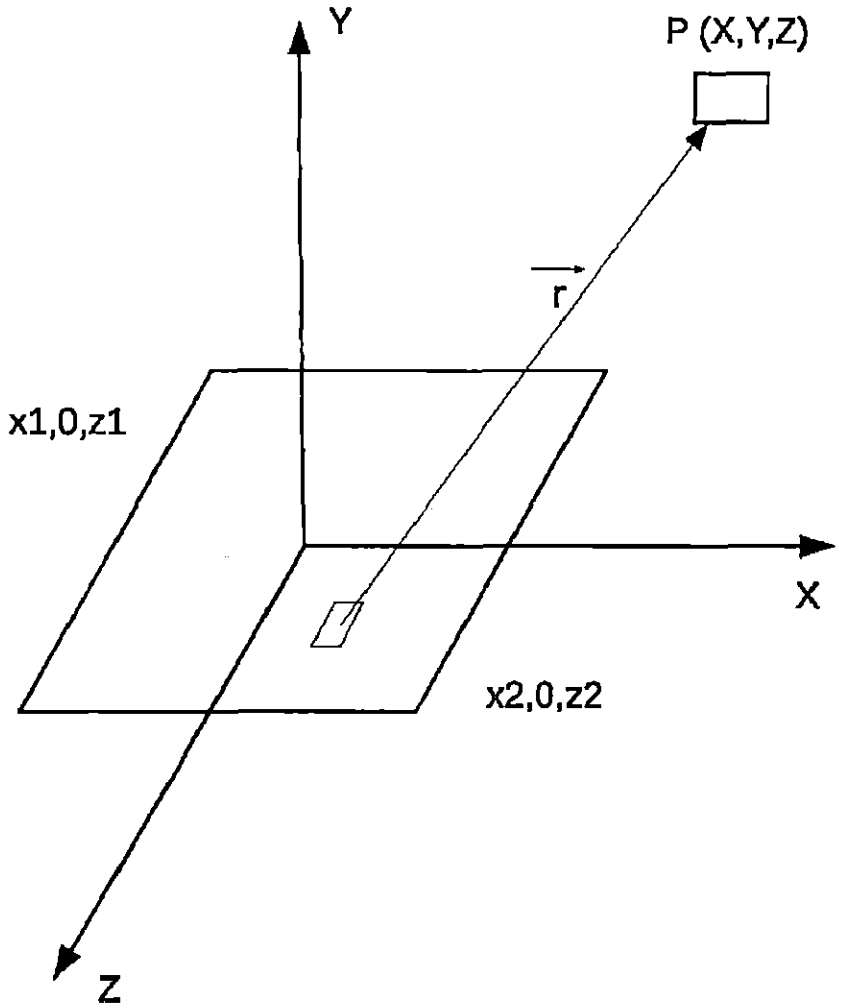

Figure 4.9: Potential at point P(X,Y,Z) with uniformly distributed source.

$$\vec{F}\,(X,Y,Z) = \int_{z_1}^{z_2} \int_{x_1}^{x_2} \frac{\hat{r}\,dx\,dz}{r^2} \tag{4.46}$$

Here $\hat{r}$ is the displacement vector from the small area element to the point $P\,(X,Y,Z)$ where we evaluate the force field. By integration of eqn. (4.46) we get expressions

for field in the X, Y and Z directions which is given as:

$$F_x(X,Y,Z) = ln\left(\frac{D_1-(Z-z_1)}{D_2-(Z-z_2)}\right) - ln\left(\frac{D_3-(Z-z_1)}{D_4-(Z-z_2)}\right) \tag{4.47}$$

$$\begin{aligned} F_y(X,Y,Z) = -\frac{1}{2}isign(Y) \times \Bigg(& S_2 \tanh^{-1}\left(\frac{R_2+iI_2}{D_4|Z-z_2|}\right) - S_2 \tanh^{-1}\left(\frac{R_2-iI_2}{D_4|Z-z_2|}\right) \\ & + S_1 \tanh^{-1}\left(\frac{R_1-iI_2}{D_3|Z-z_1|}\right) - S_1 \tanh^{-1}\left(\frac{R_1+iI_2}{D_3|Z-z_1|}\right) \\ & + S_2 \tanh^{-1}\left(\frac{R_2-iI_1}{D_2|Z-z_2|}\right) - S_2 \tanh^{-1}\left(\frac{R_2+iI_1}{D_2|Z-z_2|}\right) \\ & + S_1 \tanh^{-1}\left(\frac{R_1+iI_1}{D_1|Z-z_1|}\right) - S_1 \tanh^{-1}\left(\frac{R_1-iI_1}{D_1|Z-z_1|}\right)\Bigg) + C \end{aligned} \tag{4.48}$$

where C is the constant of integration and is given as:

$$C = \begin{cases} 0 & \text{if outside the extent of the flat surface} \\ 2\pi & \text{if inside the extent of the surface and Y>0} \\ -2\pi & \text{if inside the extent of the surface and Y<0} \end{cases}$$

$$F_z(X,Y,Z) = ln\left(\frac{D_1-(X-x_1)}{D_2-(X-x_1)}\right) - ln\left(\frac{D_3-(X-x_2)}{D_4-(X-x_2)}\right) \tag{4.49}$$

All these equations are valid throughout the physical domain including the near-field and have been used to develop the nearly exact Boundary Element solver.

4.2.5 Calculation of Electric Field

4.2.5.1 Description of the Device

For the calculation of electric field, we considered a glass RPC with the gas gap of thickness 2 mm in the simulation. The glass plates are of 3 mm thickness and above each of these plates, a thin graphite coating of thickness 20 μm has been provided with a high voltage of 9.8 KV. A 200 μm thick PET film separates the 5 mm thick plastic honey-comb pick-up panel from the graphite layers. Seven readout strips of width 3 cm in X and Y-direction have been considered. The dielectric constants of glass, graphite and gas layers have taken to be 8.0 , 12.0 and 1.000513 (equivalent to air) respectively. The electric fields calculated using the neBEM solver for the RPC at different high voltages are shown in Fig. 4.10 and Fig. 4.11 .

We have also calculated the electric fields for the RPC using the COMSOL Multiphysics [70], a commercial Finite Element Package. In the COMSOL Multiphysics, the geometry of the RPC can be entered via a graphical user interface. After entering

the geometry, we have done proper meshing for the device by rectangular components which is shown in Fig.4.12(a). As a next step we used the physical parameter like the electrostatic potential as input. Then we write the partial differential equations and apply the boundary conditions to find the solution. The solution output from the COMSOL Multiphysics for a voltage 10kV applied on the RPC electrode is shown in Fig. 4.12(b). The electric fields calculated using the COMSOL Multiphysics for the RPC at different high voltages are shown in Fig. 4.13 and Fig. 4.14 . In Fig. 4.15 and Fig. 4.16, the electric field along z-direction is calculated using both the neBEM solver and COMSOL Multiphysics. Results from the neBEM solver and COMSOL Multiphysics compare well.

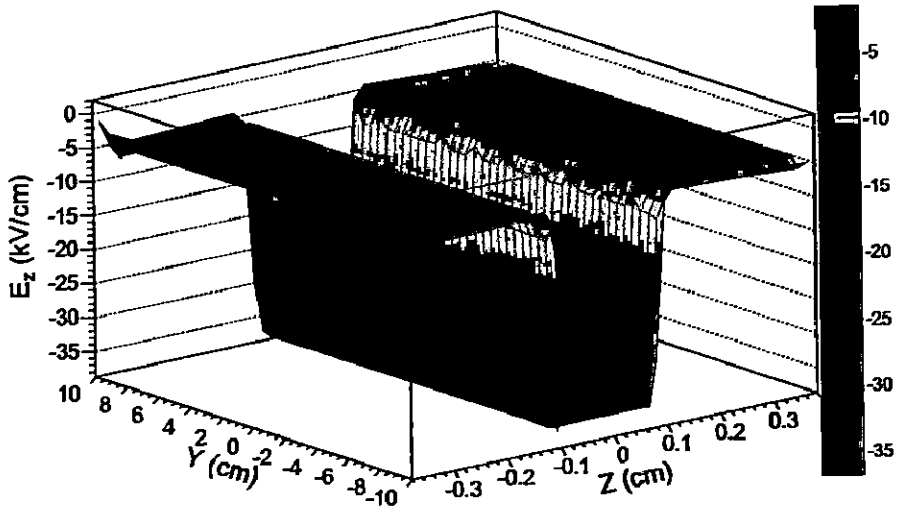

(a)

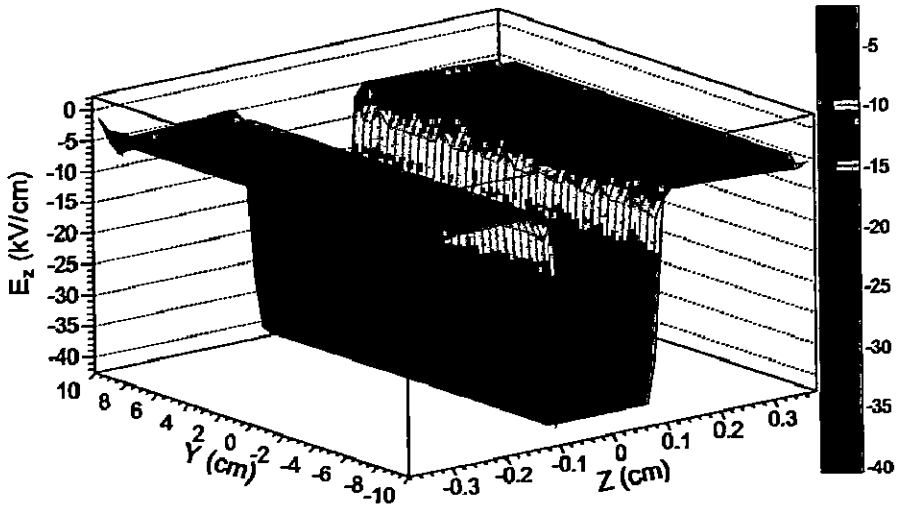

(b)

Figure 4.10: Electric Field on the YZ-plane at (a) 10kV and (b) 11 kV in a 2 mm gap glass RPC calculated using the neBEM solver.

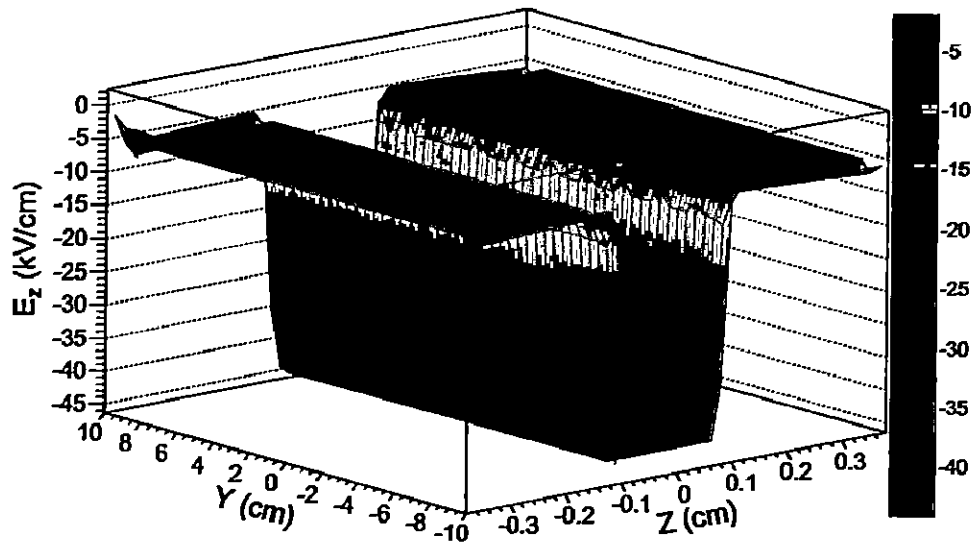

(a)

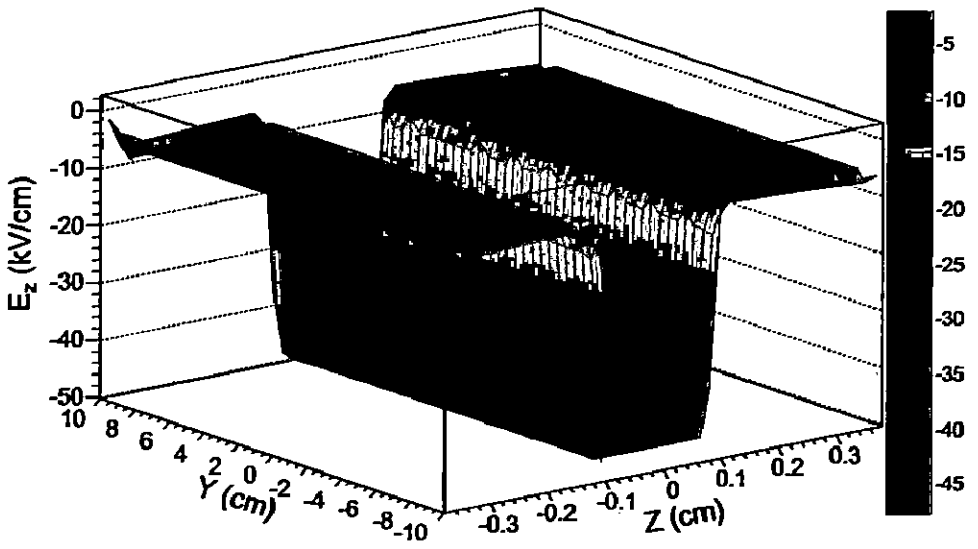

(b)

Figure 4.11: Electric Field on the YZ-plane at (a) 12 kV and (b) 13 kV in a 2 mm gap glass RPC calculated using the neBEM solver.

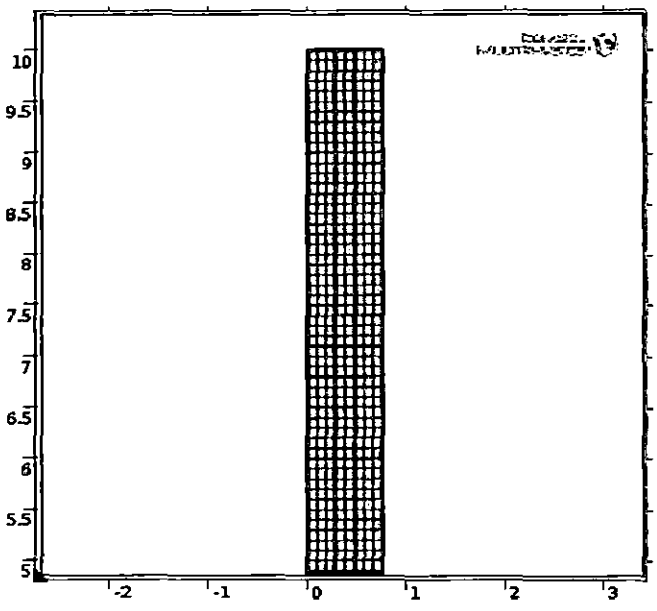

(a)

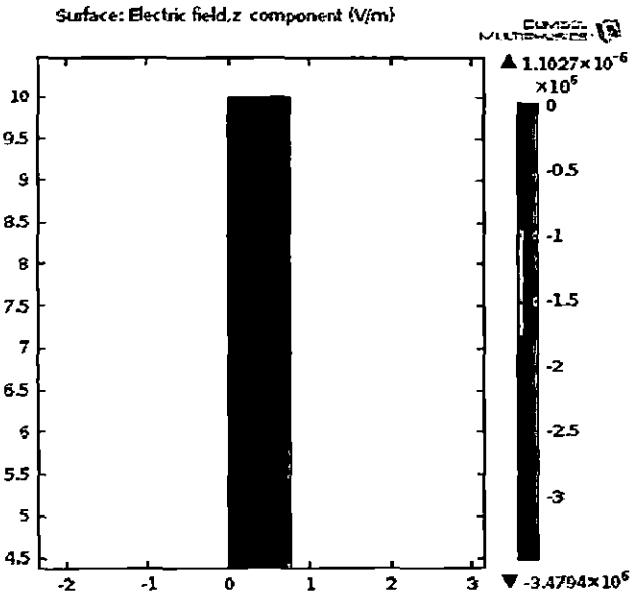

(b)

Figure 4.12: (a) Mesh and (b)The z-component of the electric field in y-z plane computed with the COMSOL Multiphysics .

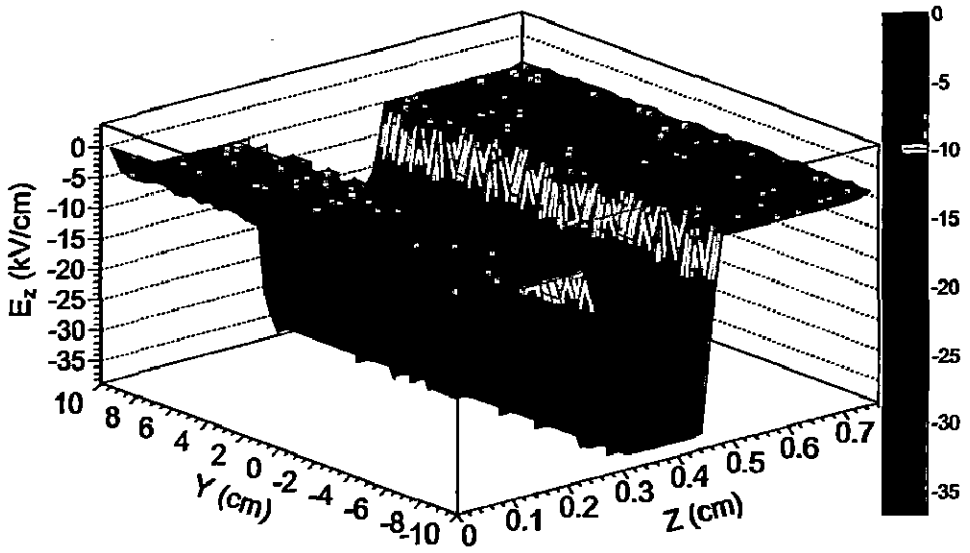

(a)

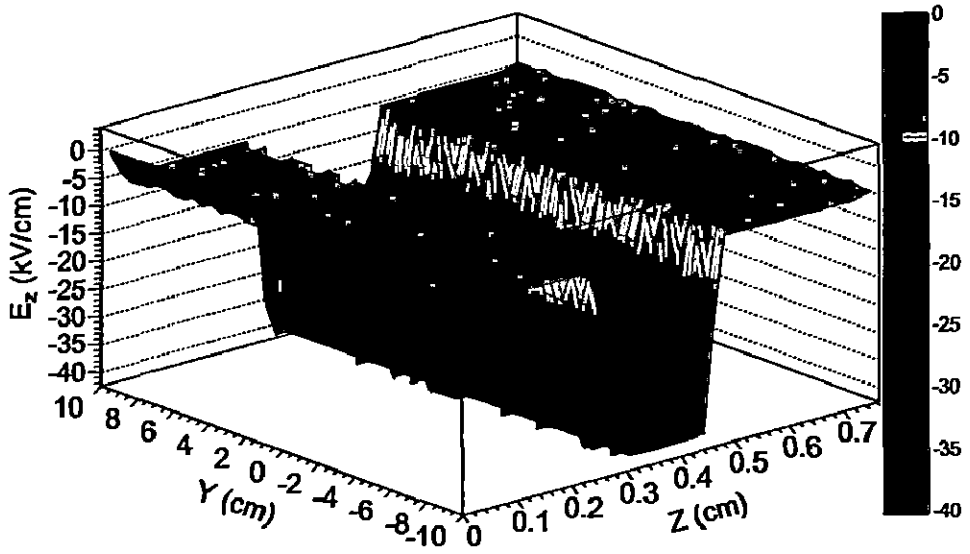

(b)

Figure 4.13: Electric Field on the YZ-plane at (a) 10kV and (b) 11 kV in a 2 mm gap glass RPC calculated using the COMSOL Multiphysics.

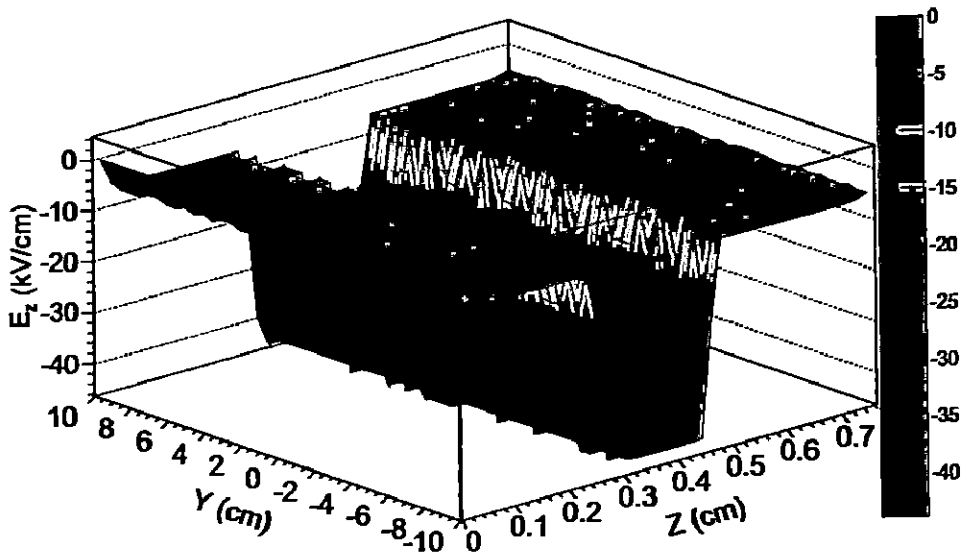

(a)

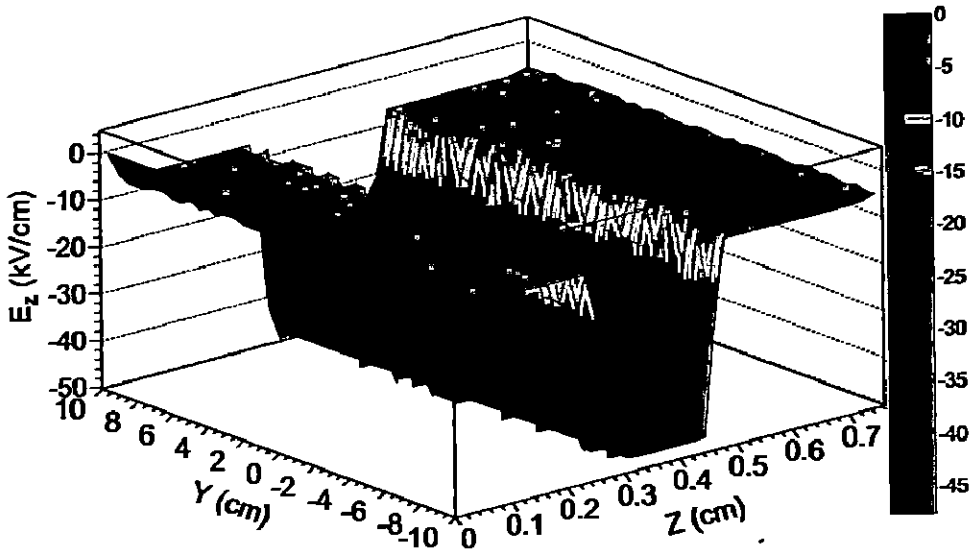

(b)

Figure 4.14: Electric Field on the YZ-plane at (a) 12 kV and (b) 13 kV in a 2 mm gap glass RPC calculated using the COMSOL Multiphysics.

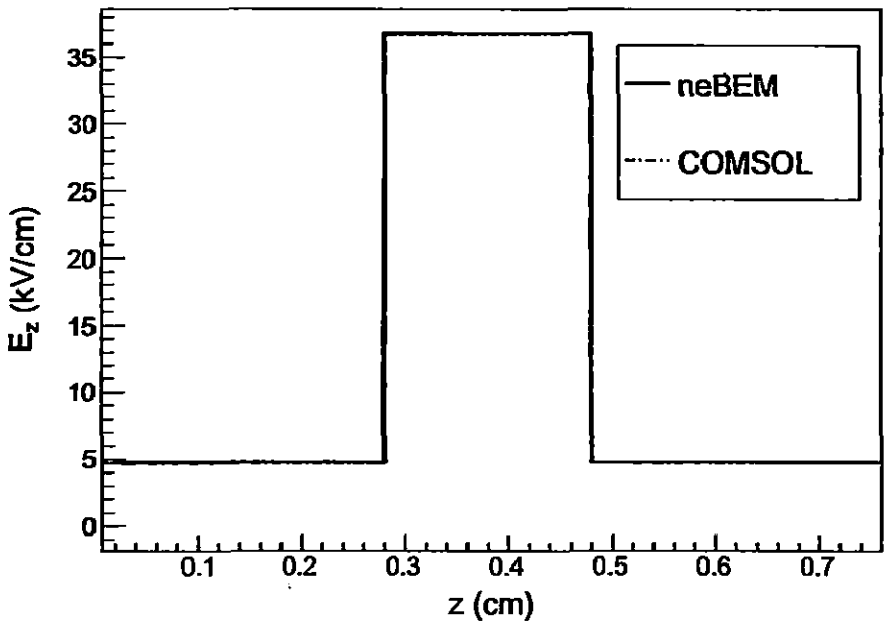

(a)

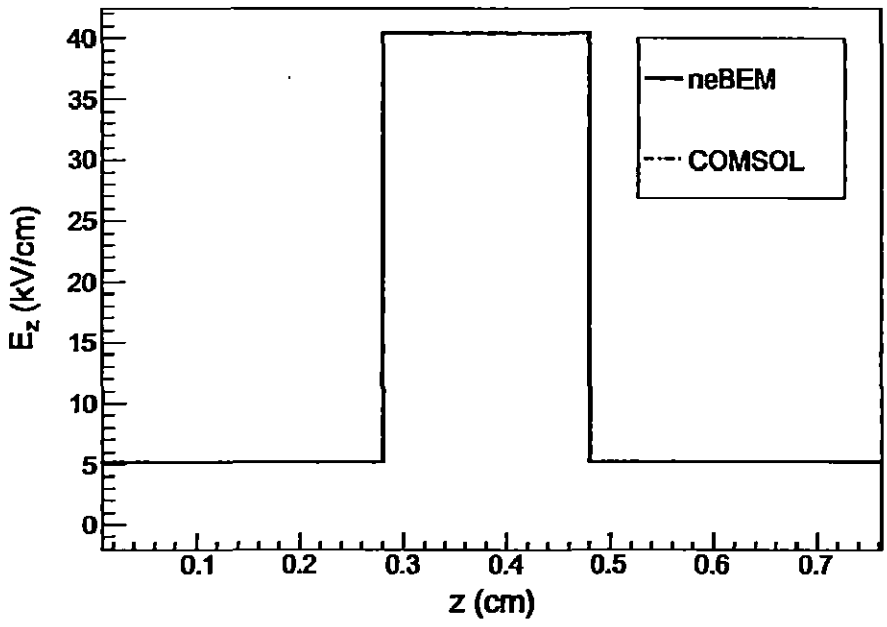

(b)

Figure 4.15: Electric Field on z-direction at (a) 10kV and (b) 11 kV in a 2 mm gap glass RPC calculated using the COMSOL Multiphysics (red dotted line) and the neBEM solver (black line).

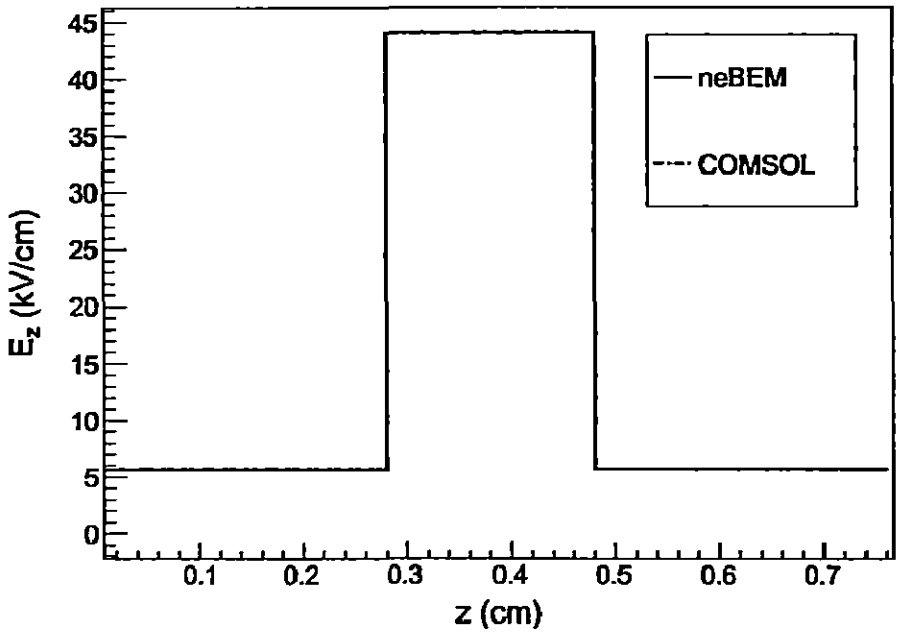

(a)

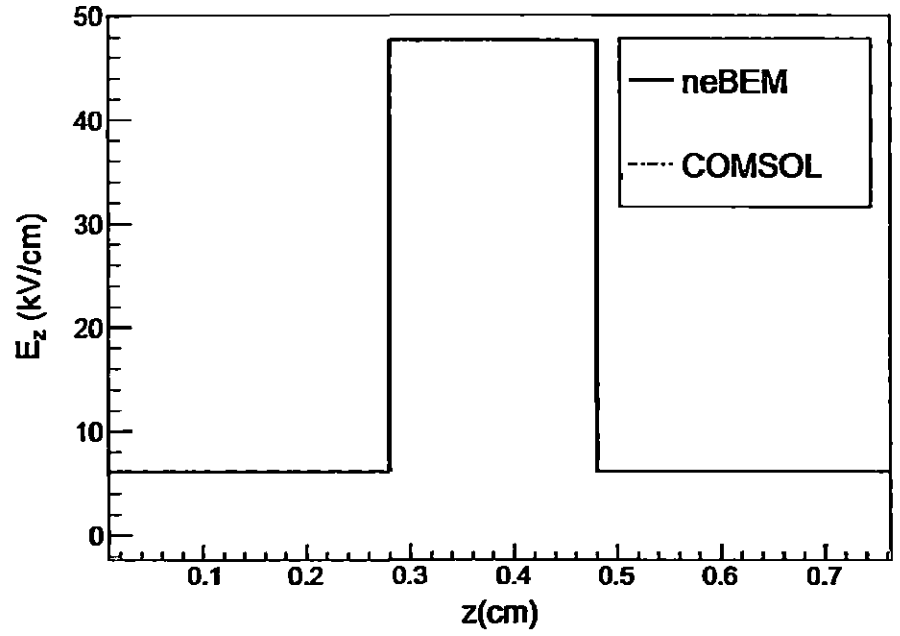

(b)

Figure 4.16: Electric Field on z-direction at (a) 12 kV and (b) 13 kV in a 2 mm gap glass RPC calculated using the COMSOL Multiphysics (red dotted line) and the neBEM solver (black line).

4.3 Charge transport in Gases

The transport of electrons and ions in gaseous detectors which are operated at a particular temperature (T) and pressure (P) will be discussed in this section. The gas obeys the ideal gas equation,

$$n = \frac{P}{k_B T} \tag{4.50}$$

at normal pressure and temperature (P = 1 atm and T = 293 K). Where k_B is the Boltzmann constant and n is the number of molecules per unit volume. n can be used to calculate the mean free path, λ_s by knowing the cross-section σ of a given process,

$$\lambda_s = (n\sigma)^{-1} \tag{4.51}$$

At normal conditions, the energy of the gas molecules depends only on the temperature which corresponds to a mean velocity,

$$v = \sqrt{\frac{3k_B T}{m}} \tag{4.52}$$

4.3.1 Electron transport

As electrons are less massive than ions, they scatter isotropically in a collision with other electrons or gas molecules in the gas chamber. They move with a random velocity, u after an interaction. With the addition of an electric field, the electron picks up an extra velocity which is termed as the drift velocity, $v_d = \frac{eE}{m}\tau$ (see section 2.2.1 of chapter 2). But most of the energy acquired by the particles from the electric field is lost in the next collision through recoil and excitation. Hence there is a balance between the energy from the field and the collision losses which is given by [59]

$$n\lambda\epsilon_E = eEx \tag{4.53}$$

where ϵ_E is the equilibrium energy, λ is the average fractional energy per collision and the number of interactions over a drift distance, x is denoted as $n = \frac{x}{v_d\tau}$ which is the ratio of the time of the drift and the average time, τ between the collisions. The mean time, τ can be expressed in terms of the cross section, σ and the number density, N as,

$$\frac{1}{\tau} = N\sigma u \tag{4.54}$$

The total energy of the drifting electron is expressed as the sum of energy acquired from the electric field and the thermal energy:

$$\epsilon = \frac{1}{mu^2} = \epsilon_E + \frac{3}{2}k_B T \tag{4.55}$$

The contribution from the thermal motion can be neglected in a particle detector since $\epsilon_E >> \frac{3}{2}k_BT$. Now the equilibrium velocities can be written as:

$$v_d^2 = \frac{eE}{mN\sigma}\sqrt{\frac{\lambda}{2}}, \tag{4.56}$$

$$u^2 = \frac{eE}{mN\sigma}\sqrt{\frac{2}{\lambda}} \tag{4.57}$$

For a gas mixture with more than one component, the drift velocities are calculated as the combined effect of cross sections, number densities and fractional energy loss per collision of individual gases.

4.3.2 Ion transport

Ions, because of their large mass and their chemical reactions in the gas medium, travel much slower in an electric field compared to electrons. In one ionizing collision ions get energy like electrons but most of their energy is lost in the successive collisions with other gas molecules. Considering the scattering between a drifting particle of mass, m and a gas molecule of mass, M their drift velocities at low and high electric filed are given by [59]

$$v_{drift} = \left(\frac{1}{m} + \frac{1}{M}\right)^{1/2}\left(\frac{1}{3k_BT}\right)^{1/2}\frac{eE}{N\sigma}(\text{ at low electric field }) \tag{4.58}$$

$$v_{drift} = \left(\frac{eE}{mN\sigma}\right)^{1/2}\left[\frac{m}{M}\left(1+\frac{m}{M}\right)\right]^{1/2}(\text{ at high electric field }) \tag{4.59}$$

From eqn. (4.58) it is clear that at low electric field the drift velocity is proportional to E and mobility is independent of E, whereas at high electric field as given in eqn. (4.59) the drift velocity is proportional to the square root of E and hence mobility decreases inversely with the square root of E. Some of the measured mobilities for certain ions are given in Table. 4.1.

Table 4.1: Mobilities of different ions [71].

Ion notation	Gas	Mobility $(cm^2V^{-1}s^{-1})$
$[CH_4]^+$	A_r	1.87
$[CO_2]^+$	A_r	1.72
$[IsoC_4H_{10}]^+$	A_r	1.56
$[(OCH_3)_2CH_2]^+$	A_r	1.51
$[CH_4]^+$	CH_4	2.26
$[CO_2]^+$	CO_2	1.09
$[IsoC_4H_{10}]^+$	$IsoC_4H_{10}$	0.61
$[(OCH_3)_2CH_2]^+$	$IsoC_4H_{10}$	0.55
$[(OCH_3)_2CH_2]^+$	$(OCH_3)_2CH_2$	0.26

4.3.3 Magboltz

The Magboltz [58] program computes electron transport parameters by numerically integrating the Boltzmann transport equation. By tracking how far the electron propagates, the program can compute the drift velocity, the longitudinal and transverse diffusion coefficients and the Townsend and attachment coefficients in various gases. By including a magnetic field, the program can also calculate the Lorentz angle. A large set of the latest cross-sectional data for numerous gases is included in the code. The gas descriptions are still being improved.

In the Magboltz program, the Boltzmann transport equation is solved for the energy distribution function which is an expansion in Legendre polynomials. The standard solution of the Boltzmann transport equation truncates the energy distribution expansion after the first two terms of the Legendre polynomials, whereas the Magboltz program uses an expansion up to the third Legendre polynomial which improves the computational accuracy of the drift velocity to better than 1 %. Higher terms in the expansion would improve the accuracy further but require a large increase in computation time. But a break down in the accuracy of the predictions of the Magboltz program in some gases at large magnetic field has been observed. This loss of accuracy was caused by some of the approximations used in the Magboltz program and occurs in simulations in large magnetic fields with a gas having a cross-section with a deep Ramsauer minimum. In order to improve the simulation and also guarantee the calculation accuracy to better than 1% for the Lorentz angle the Monte Carlo integration technique was applied to the solution of the transport equations. In the Boltzmann analysis the electron swarm is described by the macroscopic probability distribution function, which arises from a large number of individual electron-atom collisions. In the Monte Carlo simulation, the trajectory of a test electron (or electrons) is followed from collision to collision using random

numbers to determine the outcome of each impact. This technique is independent of the expansions used in describing the electron energy distribution and gives guaranteed convergence to an accuracy which is dependent only on computation time. The Magboltz program requires cross-section data base, field strength and angle and the proportion of different gas mixtures for the Monte Carlo simulation. The cross sections for 54 gases which are taken from experiments are included in the Magboltz program. The various cross sections including inelastic, attachment, ionizing, vibration etc for gases like sulphur hexafluoride , tetra fluoroethane and isobutane are given in Fig.4.17.

4.3.3.1 Magboltz transport algorithm

The Fraser and Mathieson Monte Carlo algorithm [72] is extended by S.F. Biagi [58] in the Magboltz program for calculating charge transport equations by including magnetic field at any angle to the electric field. The angular distribution is calculated by the technique of Longo and Capitelli [73]. The analytic description of the motion of the electron in electric and magnetic field will be discussed in this section. Let the magnetic field, **B** is taken along the X-axis and the electric field, E is at angle, ϕ in the X-Z plane. Now the X and Z components of electric field are $E_x = E\cos\phi$ and $E_z = E\sin\phi$. Let x_0, y_0, z_0 be the initial position and v_{x0}, v_{y0}, v_{z0} be the initial velocity of the electron. The updated position x_1, y_1, z_1 and velocity v_{x1}, v_{y1}, v_{z1} are given by,

$$\begin{aligned}
x_1 &= x_0 + v_x\Delta t + \frac{e}{2m}E_x\Delta t \\
y_1 &= y_0 + \frac{\sin\Omega}{W}\left(v_{y0} - \frac{E_z}{W}\right) + \frac{v_{z0}}{W}(1-\cos\Omega) + \frac{E_z\Delta t}{W} \\
z_1 &= z_0 + \frac{v_{z0}\sin\Omega}{W} - \frac{1}{W}\left(v_{y0} - \frac{E_z}{W}\right)(1-\cos\Omega) \\
v_{x1} &= v_{x0} + \frac{e}{m}E_x\Delta t \\
v_{y1} &= \left(v_{y0} - \frac{E_z}{W}\right)\cos\Omega + v_{z0}\sin\Omega + \frac{E_z}{W} \\
v_{z1} &= v_{z0}\cos\Omega - \left(v_{y0} - \frac{E_z}{W}\right)\sin\Omega
\end{aligned} \tag{4.60}$$

Here, $W = \frac{eB}{m}$ is the cyclotron frequency where e and m are the charge and mass of the electron, $\Omega = W\Delta t$ is the turning angle in the magnetic field in a time Δt. The unknown term time step, Δt can be found using the Null collision technique [74]. After the collision, the co-ordinates are updated with a time Δt and the stepping continues. The diffusion tensor is calculated using the displacement formalism which

is given as [58]

$$D_{ij} = \frac{1}{2N} \sum \left(\frac{1}{\Delta t} \left(X_i - V_i \Delta t \right) \left(X_j - V_j \delta t \right) \right) \tag{4.61}$$

where ij denotes the dimension x, y and z. Here the summation is taken over N number of collisions.

4.3.3.2 Electron transport parameters

The electron transport parameters, the drift velocity, the Townsend and attachment coefficients and the longitudinal and transverse diffusion coefficients depend mostly on the field configuration and also on the composition, density and purity of the individual gas components in the gas mixture. These parameters for various gas mixtures were calculated using the Magboltz program [75] and are shown in Figs 4.18-4.23. The drift velocities for SF_6 and argon based gas mixtures are shown in Fig.4.18. For electric field greater than 20 kV/cm, the drift velocities in case of argon based gas mixtures are slightly higher than for SF_6 based gas mixture. However, at low electric fields the difference is much larger. The transverse diffusion coefficients are shown in Fig.4.19. From the plot, we can observe that the transverse diffusion effect in the lower and higher electric field regions is comparable for the argon and SF_6 based gas mixtures, whereas the diffusion effect is stronger in the region 2 kV/cm to 50 kV/cm of electric field for argon based gas mixtures. The longitudinal diffusion coefficient is shown in Fig. 4.20. Fig.4.21 shows the Townsend coefficient for SF_6 and argon based gas mixtures. It is clear from this plot that the Townsend coefficient of all the gas mixtures increases with increase in the electric field. At RPC working voltages and also at lower electric fields, the SF_6 based gas mixture has comparatively lower value of the Townsend coefficient. However, the value of the Townsend coefficient increases with more percentage of argon in the gas mixture. The attachment coefficient is a very important electron transport parameter since it affects the gas gain of the detector and hence the detector parameters. Fig.4.22 shows the attachment coefficient calculated for two different argon gas mixtures. From the figure, it is evident that the gas mixture with more argon and comparatively lesser percentage of freon has a lower attachment coefficient while the gas mixture with less argon and more freon has a comparatively higher attachment coefficient. This could be the effect of freon (R134A) which is an electron quenching gas. Fig.4.23 shows the attachment coefficient of two SF_6 based gas mixtures. The attachment coefficient is very large at lower electric fields and it decreases with increasing electric field. It is very clear from this plot that with increasing SF_6 concentration in small proportions, the attachment coefficient increases. The reason is that SF_6 is a highly electronegative gas and its presence in the gas mixture even in small quantities works as a strong electron quencher.

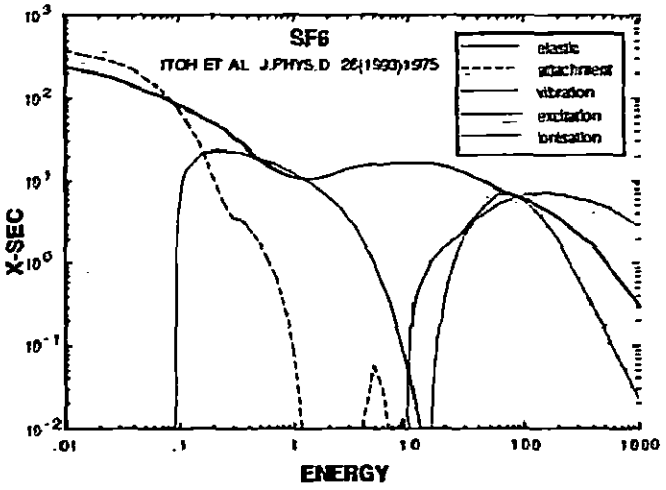

(a)

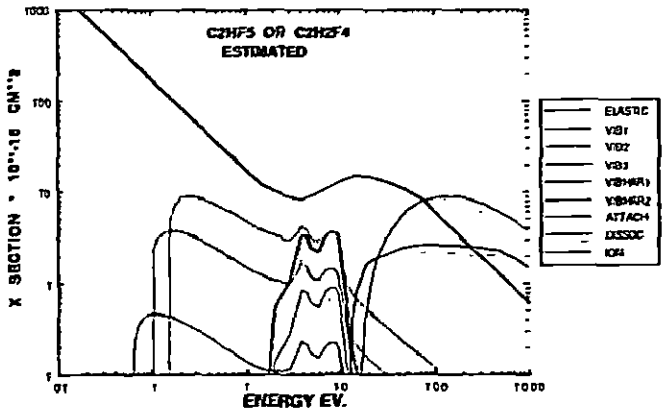

(b)

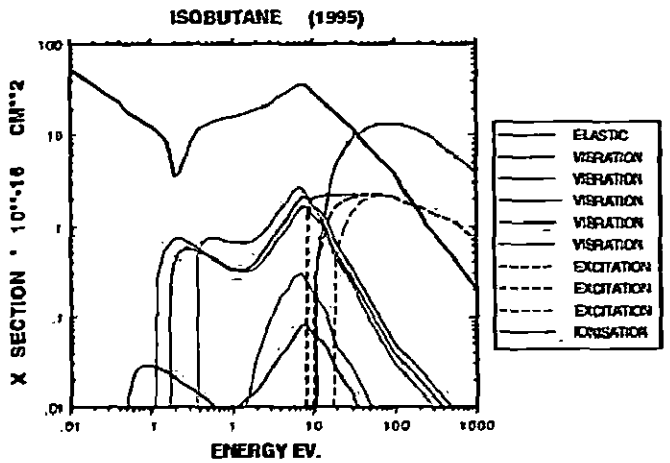

(c)

Figure 4.17: The different scattering cross sections like elastic, attachment, vibration, excitation and ionization cross sections of electrons used by Magboltz 7.1 for different gases (a) sulphur hexafluoride , (b) tetra fluoroethane and (c) isobutane are plotted

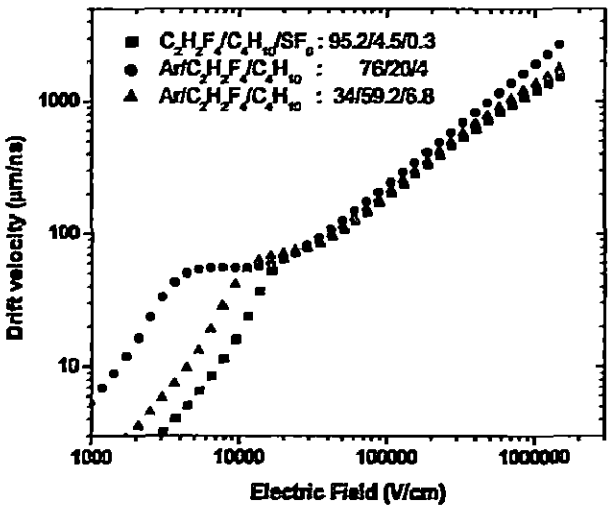

Figure 4.18: Drift velocity for three different gas mixtures calculated by Magboltz.

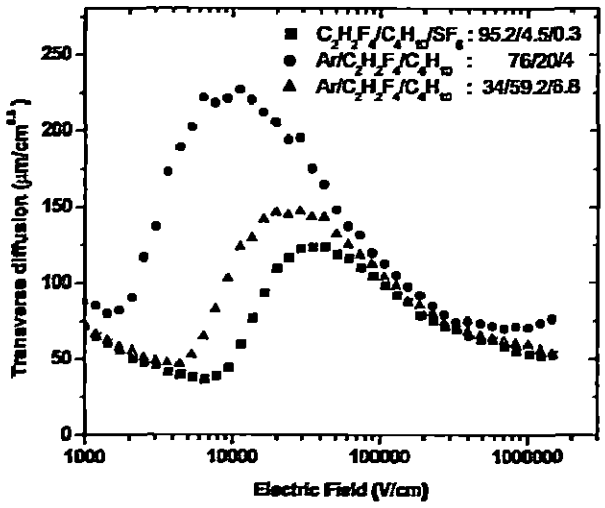

Figure 4.19: Transverse diffusion for three different gas mixtures calculated by Magboltz.

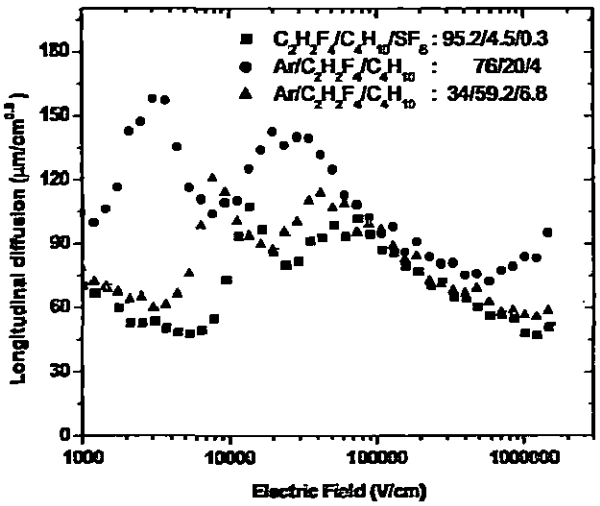

Figure 4.20: Longitudinal diffusion for three different gas mixtures calculated by Magboltz.

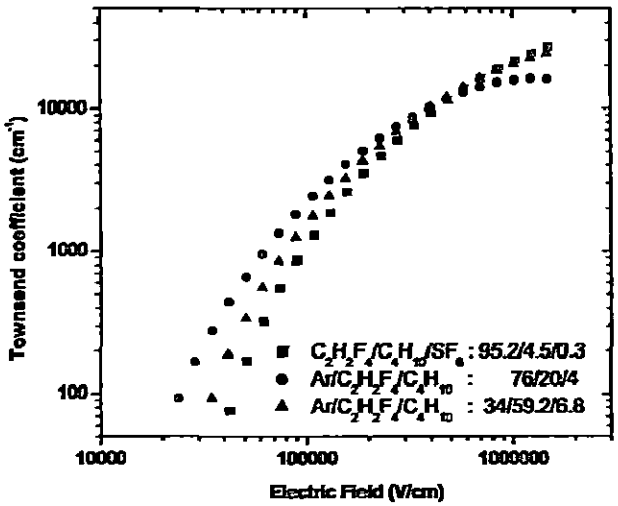

Figure 4.21: Townsend coefficient for three different gas mixtures calculated by Magboltz.

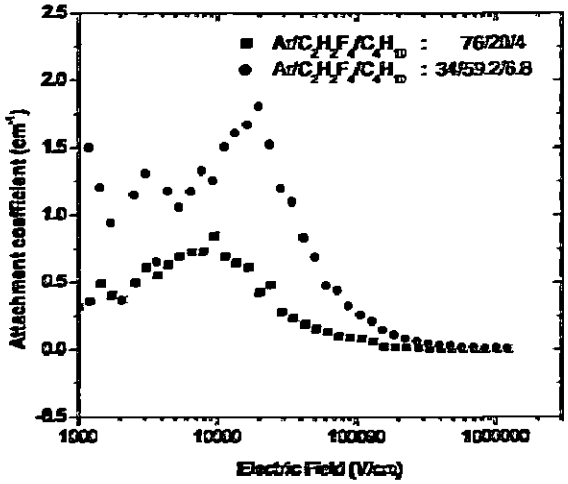

Figure 4.22: Attachment coefficient for three different argon based gas mixtures calculated by Magboltz.

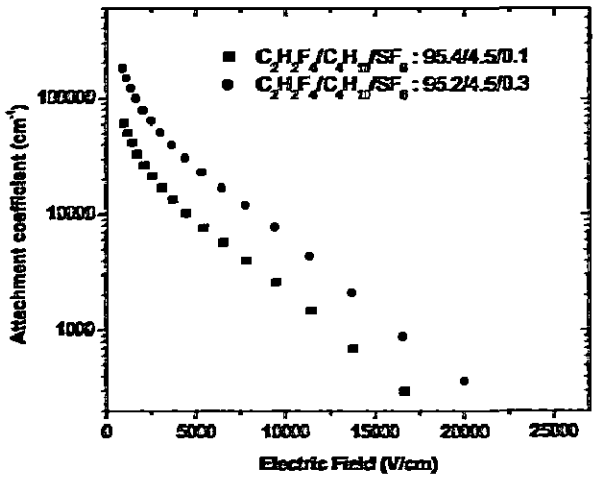

Figure 4.23: Attachment coefficient for two different SF_6 based gas mixtures calculated by Magboltz.

4.4 Summary

In this chapter, we discussed mainly the simulation tools used for carrying out the simulation of physics processes in the Resistive Plate Chamber. The primary ionization is discussed in section 4.1, where the PAI model implemented in the HEED program for the calculation of ionization cross section in various gases is discussed in detail. The Geant4 simulation has also been used to compare the primary ionization parameters like the cluster density and the cluster size distribution with the HEED results. The nearly exact Boundary Element Method (neBEM) solver is used to calculate the electric field inside the RPC which is discussed in section 4.2. The neBEM solver results have been compared with the commercial Finite Element Method package, COMSOL Multiphysics. In section 4.3, the electron transport parameters are calculated with the Magboltz program for both the avalanche and streamer gas mixtures.

CHAPTER 5

COMPARISON OF SIMULATION AND EXPERIMENTAL DATA

We have simulated the RPC parameters with the help of several existing codes, and a Monte-Carlo code developed by us for the present study. The simulation scheme is shown in Fig.5.1. We have considered the following sequence of events while carrying out the simulation. A high energy particle passing through the RPC ionizes the gas medium and clusters are formed along the particle trajectory. The primary cluster density (λ) and the average number of electrons per cluster (μ) have been calculated by the HEED program [24] for a 4 GeV muon. The electrons created by the primary ionization are further accelerated by the electric field, they multiply and induce charge on the RPC pick-up strips. For a realistic RPC geometry, the nearly exact Boundary Element Method (neBEM) solver [57] has been used to calculate the physical and weighting electrical field maps. Although the neBEM can solve 3 dimensional field maps for any given geometry, here we have used it for a 2 dimensional map since during the experiment the trigger has been so arranged that particle trajectories only in the vertical direction are considered in the measurements. Under the influence of electric field, accelerated charged particles undergo secondary ionization by colliding with the nearby gas molecules. This process continues and the avalanche developed proceeds towards the anode. The electron transport parameters, including diffusion coefficients, are calculated by the Magboltz program [75].

Finally, the Monte-Carlo (MC) code (to be described later) computes the induced charge spectra using all the above information. In this chapter, we will also study the efficiency and timing of RPC using the experimental and simulated results.

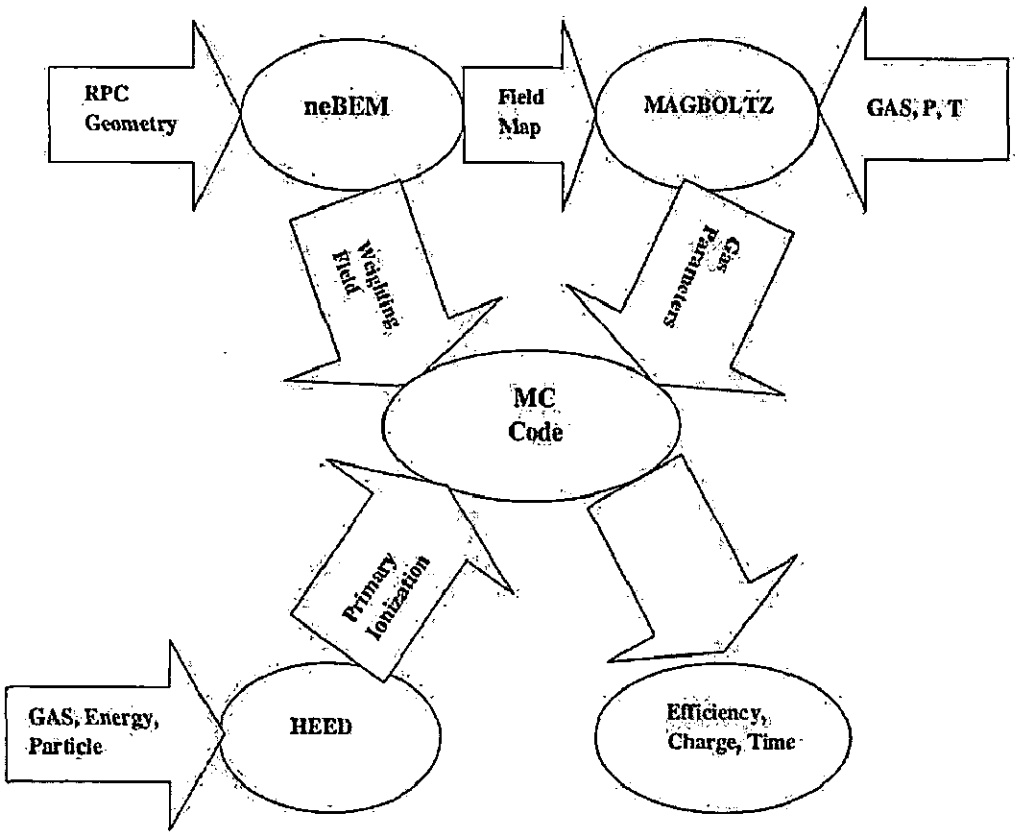

Figure 5.1: Simulation Scheme.

5.1 Electric Field and circuit representation

Using the RPC equivalent circuit shown in Fig.5.2, voltage drop across the plates has been calculated after estimating the glass resistance from the VI curve (Fig.5.3). It has been found that a voltage drop of around 314 V occurs across the glass electrodes when a high voltage of 9.8 kV is applied on the RPC electrodes in the experiment. Thus, actual voltage appearing across the gas gap has been calculated to be, $V_{gap} = HV - IR_{glass}$. From the above, the electric field across the gas gap is around 4.7 kV/mm. By carrying out a small numerical experiment, we found that this value of the electric field can be obtained in simulation when we apply a high voltage of 13 kV across the RPC electrodes (see, Fig.5.4). Besides estimating the physical electric field in the RPC, the neBEM solver has also been used to estimate the weighting field (E_W) as shown in Fig.5.5.

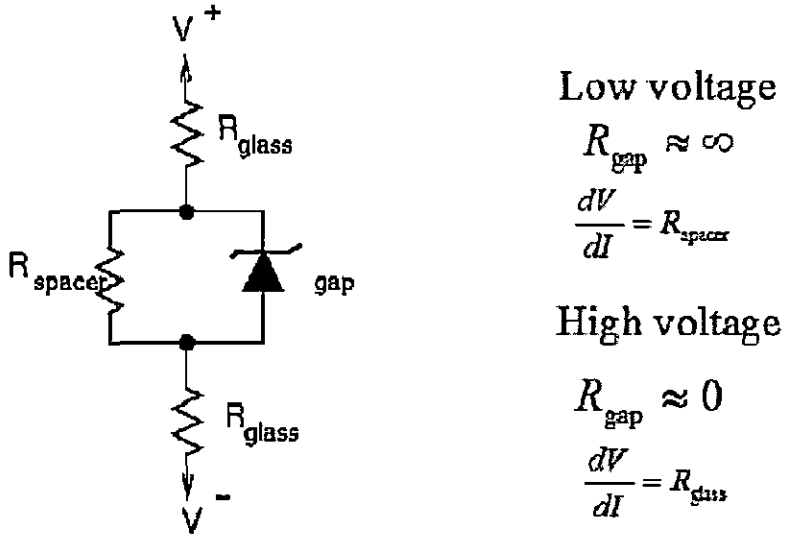

Figure 5.2: RPC equivalent electrical circuit.

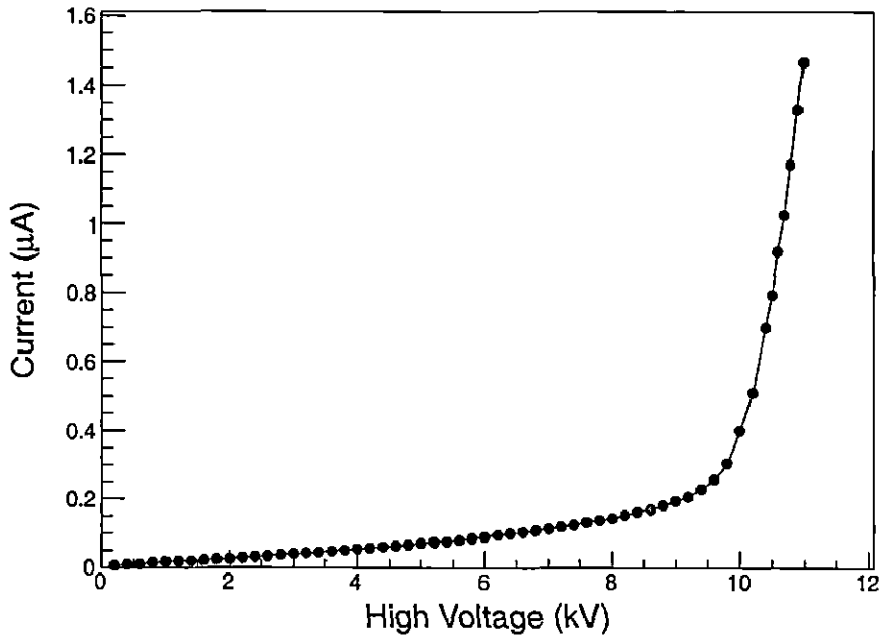

Figure 5.3: V-I characteristics of the RPC.

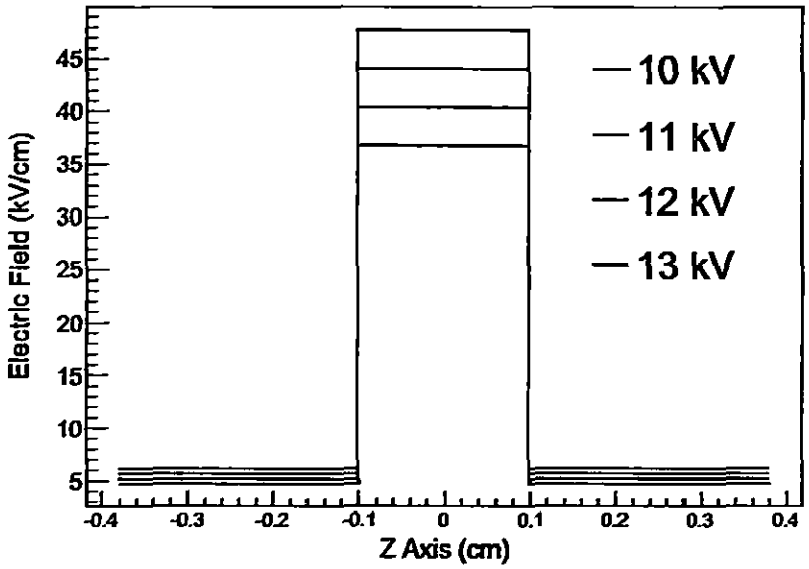

Figure 5.4: Variation of Electric Field along z-direction

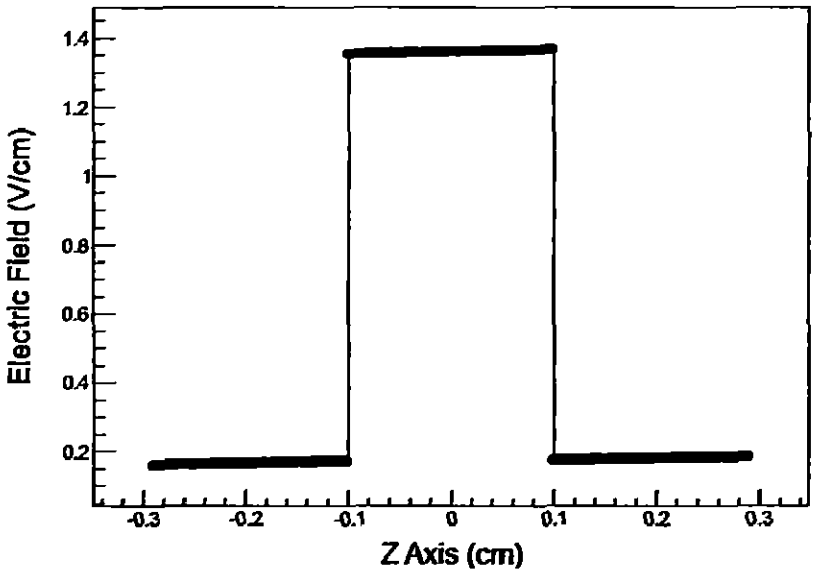

Figure 5.5: Variation of Weighting Field along z-direction.

5.2 Monte Carlo Model

The simulation model used by Abbrescia et al [76] and Ahn et al [77] first considers an ionizing particle passing through the detector (see diagram, Fig. 5.6).

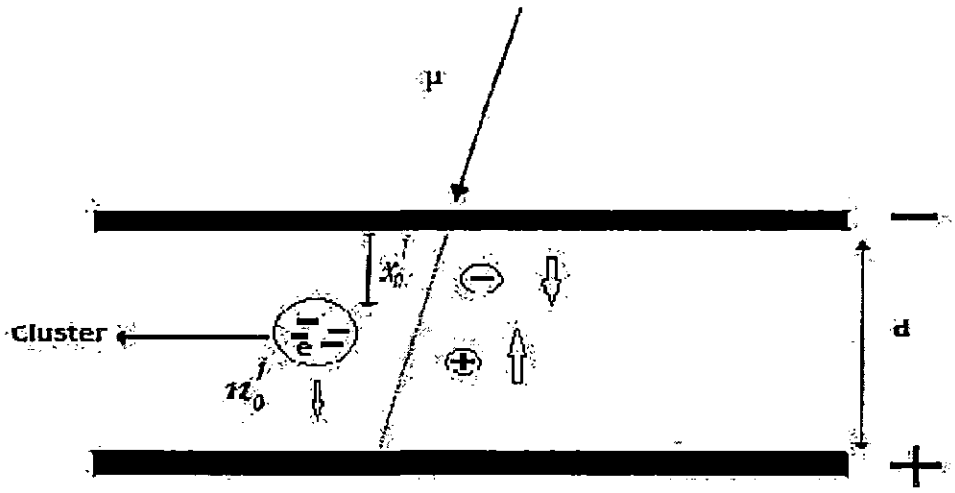

Figure 5.6: Schematic diagram of an Ionizing particle crossing the detector.

The probability, P_{cl}, that k clusters are generated in the gap is given by the Poisson distribution,

$$P_{cl}(n_{cl} = k) = \frac{(d\lambda_{eff})^k}{k!} e^{-d\lambda_{eff}} \tag{5.1}$$

where,

$$\lambda_{eff} = \frac{\lambda}{\cos\phi}$$

Here, ϕ is the azimuthal angle of the incident particle and d is the gap width. Here we are assuming cosmic muons coming in the vertical direction and hence we take ϕ as zero, so λ_{eff} will reduce to λ. λ is the primary cluster density which is calculated from the HEED program as we discussed in section 4.1.3 of chapter 4 of this thesis. The probability distribution $P_p^j(x)$ of the initial position x_0^j of the jth cluster is given by the Poisson statistics

$$P_p^j(x_0^j = x) = \frac{\lambda_{eff}}{(j-1)!}(x\lambda_{eff})^{j-1} e^{-x\lambda_{eff}}, 0 < x < d. \tag{5.2}$$

The total charge q at position x is

$$q(x) = \sum_{j=1}^{n_{clust}} q_e n_0^j M_j e^{(\alpha-\eta)(x-x_0^j)} \tag{5.3}$$

Here α is the Townsend coefficient and η is the attachment coefficient. Fig.5.7 and Fig.5.8 show the attachment and Townsend coefficient for different gas mixtures. Here n_0^j is the number of primary electrons in the jth cluster which obeys the Poisson distribution,

$$P_{n_0^j}(n) = \frac{\mu^n}{n!} exp(-\mu) \tag{5.4}$$

Here μ is the mean number of primary electrons that we calculate from the HEED program. The effective Townsend coefficient is $\alpha - \eta$ and M_j accounts for the stochastic fluctuations of the exponential growth. The fluctuation term is incorporated by taking a random number from the following Polya distribution [78] which is valid for high values of reduced electric field, E/p.

$$P_P(n_{av} = n) = \left[\frac{n}{N}(1+\theta)\right]^{\theta} exp\left[-\frac{n}{N}(1+\theta)\right] \tag{5.5}$$

where,

$$N = n_0 e^{(\alpha-\eta)(d-x_0)}$$

and θ is taken as 0.5 [78]. The induced current $i_{ind}(t)$ on the external pick-up electrodes is calculated from the Ramo theorem [79].

$$i_{ind}(t) = -v_d . E_W q_e e^{(\alpha-\eta)v_d \Delta t} \sum_{j=1}^{n_{cl}} n_0^j M_j \tag{5.6}$$

where E_W is the weighting field and this parameter is calculated using the neBEM solver by putting a weighting potential, $V_W = 1V$ on the RPC pick-up electrode. Induced charge is obtained by the direct integration of eqn. (5.6).

$$q_{ind} = \frac{q_e}{(\alpha-\eta)} \frac{E_W}{V_W} \sum_{j=1}^{n_{cl}} n_0^j M_j \left[e^{(\alpha-\eta)(d-x_0^j)} - 1\right] \tag{5.7}$$

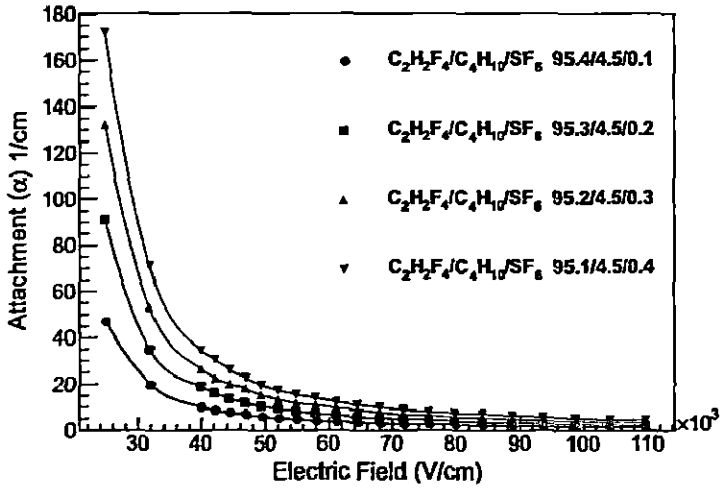

Figure 5.7: Attachment coefficient (α) Vs Electric Field for different SF_6 percentages in the gas mixture.

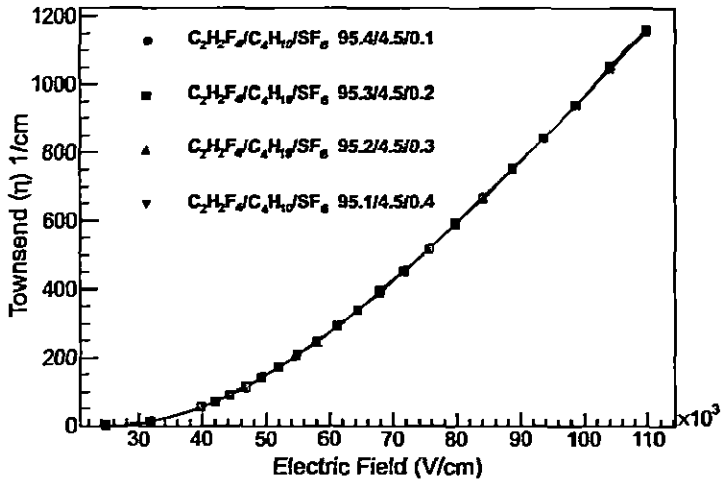

Figure 5.8: Townsend coefficient (η) Vs Electric Field for different SF_6 percentages in the gas mixture.

5.3 Charge Spectra

The Monte Carlo code that we developed is based on the model described in the last section. It considers the following sequence of events. A muon of 4 GeV energy

passes the RPC in the vertical direction. It ionizes the gas in the detector and clusters are formed. The mean number of electrons per cluster (μ) and the primary cluster density (λ) as calculated from the HEED program are found to be 2.06 and 7.6 mm^{-1} respectively for a 4 GeV muon. We distribute the primary clusters in the gas gap according to the Poisson distribution (see, eq. (5.4)) and allow each electron to drift in the electric field to the anode plate. The drifting electrons produce avalanches and the growth of these avalanches are stopped whenever the number of electrons in an avalanche reaches 10^8 (Raether limit). The electrons are drifted in a step size one order of magnitude less than their mean free path. To get the simulated charge spectrum, the simulated charge obtained from eq. (5.7) is multiplied by the pre-amplifier gain of 80 (see Fig. 3.8). In Fig. 5.9, the simulated charge spectra for the gas mixture, $C_2H_2F_4/C_4H_{10}/SF_6$ at four different proportions of SF_6 (0.1%, 0.2%, 0.3% and 0.4%) are given. In Figs. 5.10 and 5.11, we have compared the simulated charge spectra with the measured spectra for different concentrations of SF_6. In these figures, statistics of the simulated charge spectra are adjusted to compare with the statistics of the experimental charge spectra. It can be seen from the figures that the trends observed in both the measured and simulated charge spectra are similar. As the concentration of SF_6 is increased in the RPC gas mixture, the total charge induced reduces. In addition, the spectra gets sharper in nature with the left-shifted peaks indicating lesser events with large charge induction.

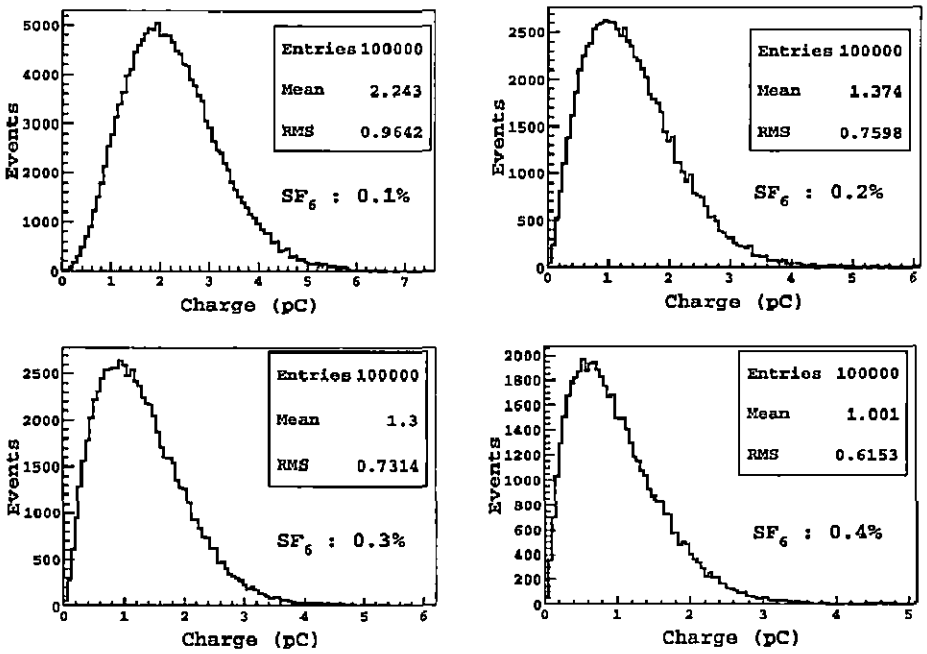

Figure 5.9: Simulated charge spectra for different concentrations of SF_6.

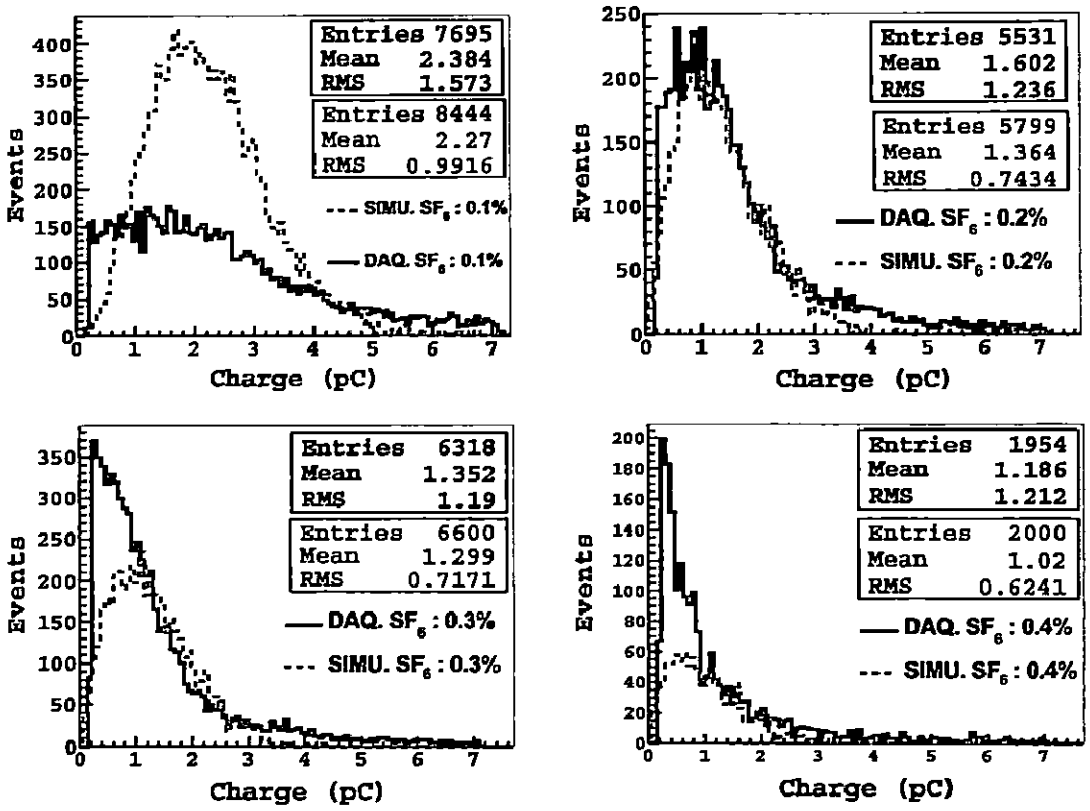

Figure 5.10: Comparison of measured (DAQ) and simulated charge spectra for different concentrations of SF_6.

In the following Table 5.1, we present the variation of charge induced on the pick-up electrodes due to small variations in SF_6 concentration in the RPC gas mixture. It can be seen that following a decrease from 0.4 to 0.1 per cent of SF_6, the measured induced charge increases from 1.18 pC to 2.38 pC in DAQ and from 0.79 pC to 1.83 pC in CRO. The simulated charges also increase from 1.0 pC to 2.24 pC. There are some approximations that we have used in the simulation, like the energy of the incoming muon is 4 GeV. However, the atmospheric muons with a wide energy spectrum pass through the detector. But from Fig. 4.6, given in the section 4.1.5 of this thesis, we can see that at higher energies, the cluster density is almost independent of the muon momentum. In Table 5.1, two sets of experimental measurements have been included. There are two separate runs for DAQ and CRO. It is difficult to take long runs at a time on CRO because of storage limitations and hence we have low statistics for CRO. The similar number of events are generated for simulations. The statistics in the experimental data is low and different so two different sets of simulated spectra are used to compare these results. We plan to further improve the experimental setup and method, besides aiming for higher statistics for a better

agreement between the experimental data and simulated results. Since SF_6 is an expensive gas, the present study can help in optimizing the amount of SF_6 to be used in real experiments.

SF_6	DAQ		Simulated		CRO		Simulated		Simulated	
(%)	Mean	Events	Mean	Events	Mean	Events	Mean	Events	Mean	Events
0.1	2.38	7695	2.27	8444	1.83	2158	2.28	2500	2.24	100000
0.2	1.60	5531	1.36	5799	1.37	2115	1.37	2500	1.37	100000
0.3	1.35	6318	1.30	6600	1.08	2287	1.30	2500	1.30	100000
0.4	1.18	1954	1.02	2000	0.79	2182	1.00	2500	1.01	100000

Table 5.1: Summary of measured and simulated charge (in pC) spectra.

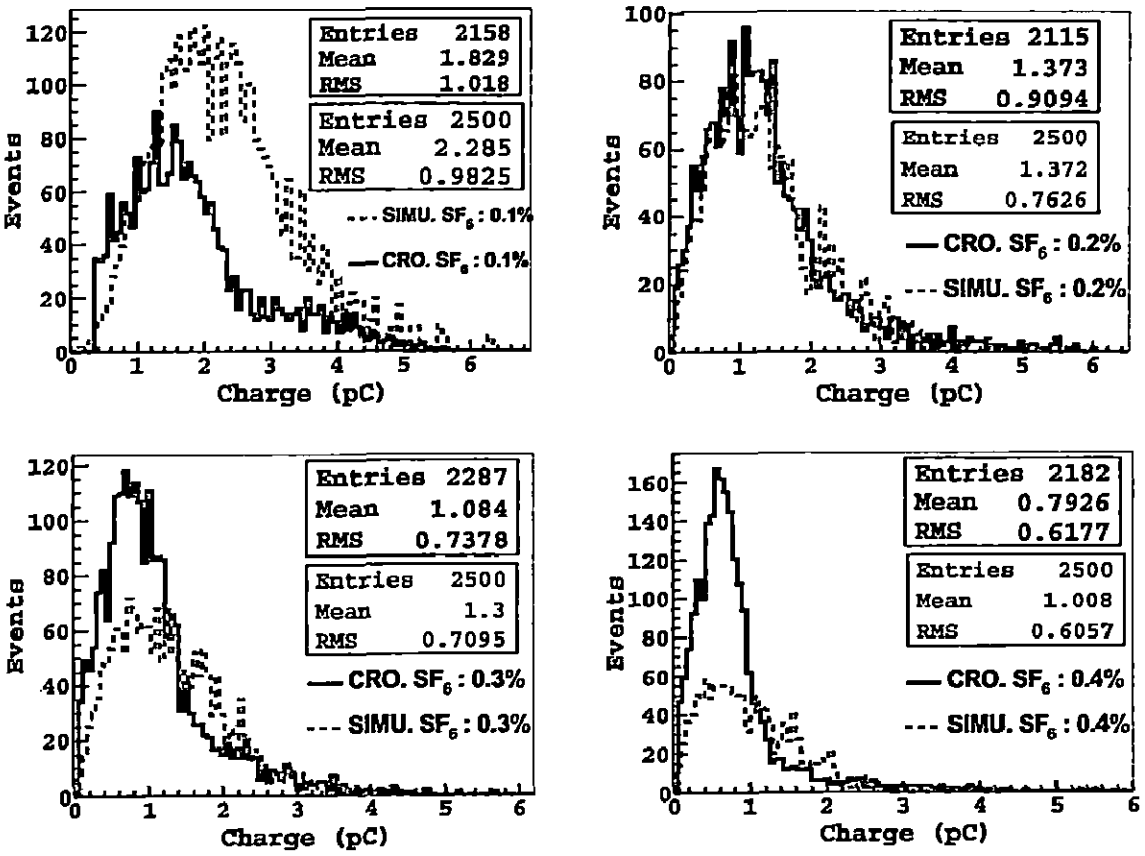

Figure 5.11: Comparison of measured (CRO) and simulated charge spectra for different concentrations of SF_6.

5.4 Efficiency

In this section, we calculate the efficiency of the RPC using the formulation given by W. Riegler et al [80] and compare the result with the experiment. According to this formulation an RPC is said to be efficient if the first cluster develops into an avalanche that exceeds the charge threshold, Q_t or the first cluster is attached and the second cluster develops into an avalanche that exceeds the charge threshold, Q_t or the first and second clusters are attached and the third cluster develops into an avalanche that exceeds the charge threshold and so on. Further, to calculate efficiency we assume that the cluster contains only one electron and we neglect the avalanche fluctuation. In that case, the expression for the induced charge (eqn. (5.7)) reduces to the following expression,

$$q_{ind}(x) = \frac{q_e}{(\alpha-\eta)}\frac{E_W}{V_W}\left[e^{(\alpha-\eta)(d-x)} - 1\right] \tag{5.8}$$

For the first cluster at position x, the charge threshold condition corresponds to the length $x<x_0$,

$$x_0 = d - \frac{1}{(\alpha-\eta)}\ln\left(1 + \frac{V_W}{E_W}\frac{(\alpha-\eta)}{q_e}Q_t\right) \tag{5.9}$$

In case the first cluster is not attached, the probability of the first cluster obeying the threshold condition is,

$$P_1 = \left(1 - \frac{\eta}{\alpha}\right)\int_0^{x_0}\frac{1}{\lambda}e^{-\frac{x}{\lambda}}dx \tag{5.10}$$

In case the first cluster is attached but the second cluster is not attached, the probability of the second cluster obeying the threshold condition is,

$$P_2 = \int_0^{x_0}\int_0^{x_2}\frac{\eta}{\alpha}\frac{1}{\lambda}e^{-\frac{x_1}{\lambda}}\frac{1}{\lambda}e^{-\frac{x_2-x_1}{\lambda}}dx_1dx_2 \tag{5.11}$$

Now we can write the probability for obeying the threshold condition in case, the n^{th} cluster is not attached and all the n-1 clusters before this are attached,

$$P_n = \left(\frac{\eta}{\alpha}\right)^{n-1}\left(1 - \frac{\eta}{\alpha}\right)\left(1 - H\left(\frac{x_0}{\lambda}, n\right)\right) \tag{5.12}$$

where,

$$H\left(\frac{x_0}{\lambda}, n\right) = e^{-\frac{x_0}{\lambda}}\sum_{j=0}^{n-1}\frac{\left(\frac{x_0}{\lambda}\right)^j}{j!}$$

The expression for efficiency can now be written as,

$$\epsilon = \sum_{n=1}^{\infty} P_n = 1 - e^{-(1-\frac{\eta}{\alpha})\frac{d}{\lambda}} \left(1 + \frac{V_W}{E_W}\frac{(\alpha-\eta)}{q_e} Q_t\right)^{\frac{1}{\alpha\lambda}} \tag{5.13}$$

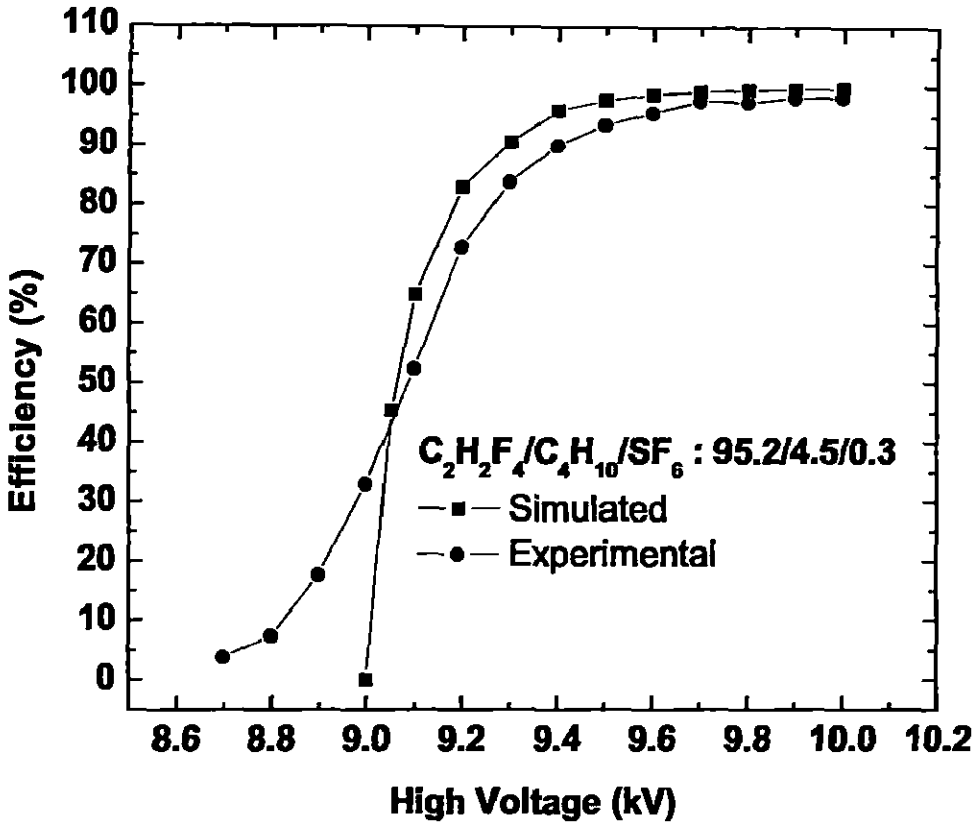

Figure 5.12: Experimental efficiency compared with simulated efficiency for gas the gas mixture $C_2H_2F_4/C_4H_{10}/SF_6$ in the proportion 95.2/4.5/0.3.

The Experimental efficiency of the RPC is defined as the ratio of number of cosmic muon triggers recorded in the RPC to the actual number of muon trigger signals generated by the cosmic muon telescopes. We set the threshold voltage as 20 mV. The operating voltage of the RPC is selected in the region where we get maximum efficiency. Fig. 5.12 shows the efficiency plateau [20] measured for the gas mixture, $C_2H_2F_4/C_4H_{10}/SF_6$ in the proportion 95.2/4.5/0.3 at different high voltages. The efficiency plateau shows that above the voltage, 9.5 kV the efficiency

is constant and so we get a wider operating range for the RPC. We simulated the RPC efficiency obtained experimentally using the above mentioned formulation. The simulated results are also shown in Fig. (5.12). As can be seen from the figure, the experimental and simulated values of efficiency agree well above 9.5 kV. In the region below 9.5 kV, the simulated efficiency sharply decreases to zero at 9.0 kV, whereas the experimental efficiency decreases comparatively slowly to zero at 8.6 kV. Fig. 5.13 shows the simulated efficiency calculated for different gas mixtures. SF_6 is added in small quantities (0.1%, 0.2%, 0.3% and 0.4%) to the gas mixture, $C_2H_2F_4/C_4H_{10}$. Here we considered the charge threshold as 80 fC. From Fig. 5.13, it is clear that the efficiency curves are shifted to the high voltage region as we increase the SF_6 concentration. A shift of around 100 V is observed for every 0.1% increase of SF_6 in the gas mixture.

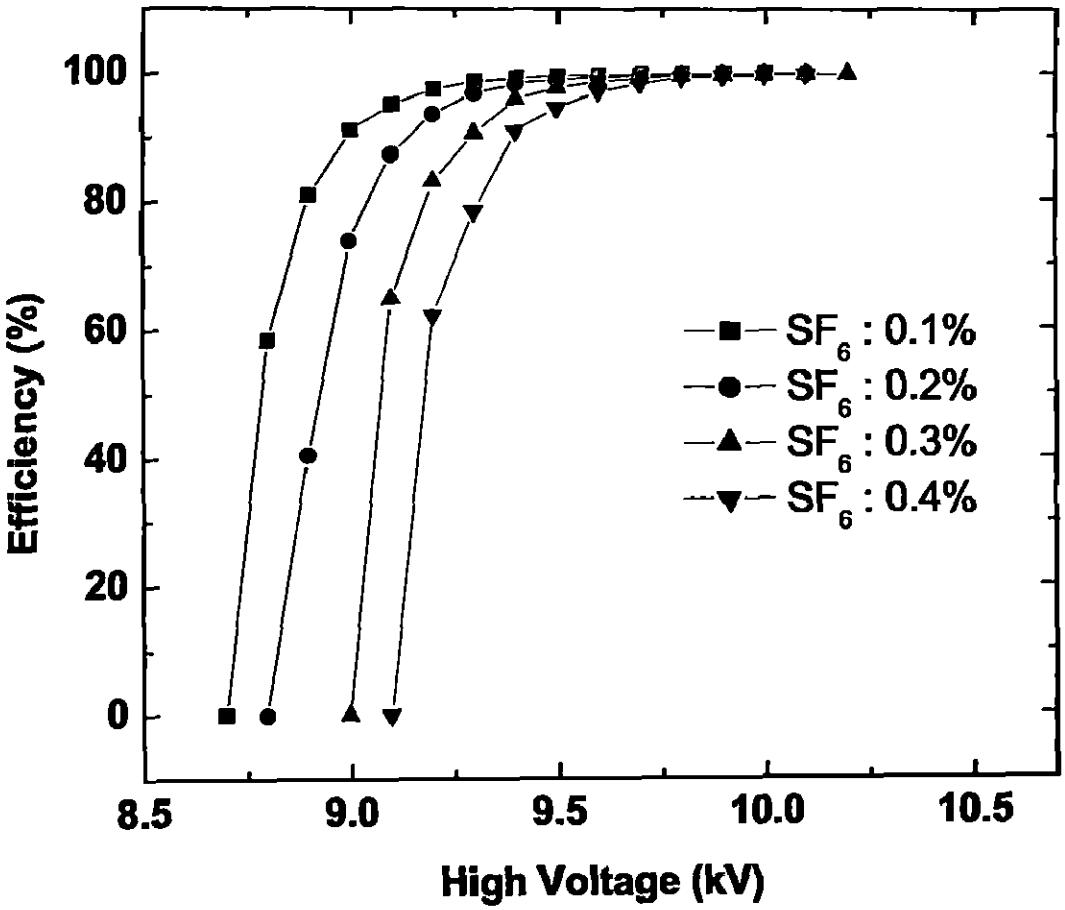

Figure 5.13: Simulated efficiency of different SF_6 concentrations.

5.5 Timing

The time response function can be defined as the probability that the number of electrons in the gas gap crosses a threshold number of electrons (n) between time t and $t + dt$. Let $g(m)$ be the probability to produce m electrons when a charged particle passes through the detector and $h(m, n, t)dt$ be the probability that an avalanche starting with m electrons crosses a threshold of n electrons in the time interval, dt. The RPC time response function is given by [81],

$$\rho(n,t) = \frac{1}{a_0} \sum_{0}^{\infty} g(m)h(m,n,t) \tag{5.14}$$

The analytic expressions for the time response function for a charged particle passing through the RPC gas gap have been derived by W. Riegler [81] for the following cases (i) single electron per cluster with no attachment, (ii) single electron cluster with attachment and (iii) a realistic HEED or $1/n^2$ cluster size distribution. The HEED cluster size distribution and the primary electron distribution calculated for a 2 mm gap RPC are shown in section 4.1.5 in the fourth chapter of this thesis. Assuming, (i) an average number of n_0 efficient clusters which fluctuate according to the Poisson distribution, (ii) a cluster size distribution $f(m)$ with Z-transform $F(z)$ with a radius of convergence r_F, (iii) avalanche multiplication according to Legler's avalanche model and (iv) a threshold of n electrons, the time response function for an RPC is given by [81],

$$\rho(n,t) = \frac{1}{2\pi i}\oint \frac{e^{n_0F(z)-1}}{e^{n_0}-e^{n_0F(1/k)}}\frac{(1-k^2)nS}{(1-kz)^2}e^{-St-n\frac{(1-k)(1-z)}{1-kz}}e^{-St}dz \tag{5.15}$$

Here $S=(\alpha-\eta)v_d$ and $k=\alpha/\eta$. The integration in eqn (5.15) is over a circle with $r_F<r<1/k$ (here, $r_F=0$). Substituting $z=re^{i\phi}$, so $dz=ire^{i\phi}d\phi$ and integrating over ϕ from $-\pi$ to π, we can evaluate the expression ((5.15)), numerically as,

$$\rho(n,t) = \frac{1}{2\pi}\int_{-\pi}^{\pi}\frac{G(re^{i\phi})}{1(1-G(1/k)}\frac{(1-k)^2}{(1-kre^{i\phi})^2}Sne^{i\phi-St-n\frac{(1-k)(1-re^{i\phi})}{1-kre^{i\phi}}}e^{-St}d\phi \tag{5.16}$$

For a realistic HEED cluster distribution, the function $G(z)$ summed over N electrons can be written as,

$$G(z) = \sum_{m=0}^{N}\frac{p_m}{z^m} \tag{5.17}$$

Where p_m is the cluster size probability distribution calculated from the HEED program. Time resolution comes from the avalanche fluctuation and the fluctuation in the number of primary electrons. Let $\bar{t}$ be the average threshold crossing time for m primary electrons which has been calculated by [81]

$$\bar{t}(m) = \frac{1}{S}\left[lnn+\gamma+ln(1-k)-\frac{1}{1-k^m}\sum_{j=1}^{m-1}\frac{1}{j}\left[(1+k^m)-(k^j+k^{m-j})\right]\right] \tag{5.18}$$

and the variance of the threshold crossing time has also been calculated as,

$$\sigma^2(m) = \frac{1}{S^2}\left[\frac{\pi^2}{6}+\frac{2}{1-k^m}\sum_{j=1}^{m-1}\sum_{r=1}^{j-1}\left[\frac{1}{jr}\left(1-k^{m-j}+k^j-k^m\right)-\frac{k^r}{r(j-r)}\left(1-k^{m-j}\right)\right]\right.$$
$$+\frac{1}{(1-k^m)^2}\sum_{j=1}^{m-1}\sum_{r=1}^{m-1}\frac{1}{jr}\left[2(1+k^m)(k^j+k^{m-j})-(1+k^m)^2\right.$$
$$\left.\left.-(k^j+k^{m-j})(k^r+k^{m-r})\right]\right] \tag{5.19}$$

Now the first and second moment of the time response function in terms of $g(m)$ are

$$\bar{t} = \sum_{m=1}^{\infty} g(m)\bar{t}(m) \tag{5.20}$$

$$\bar{t^2} = \sum_{m=1}^{\infty} g(m)\left(\bar{t}^2(m) + \sigma^2(m)\right) \tag{5.21}$$

and so the variance is,

$$\sigma^2 = \bar{t^2} - \bar{t}^2 \tag{5.22}$$

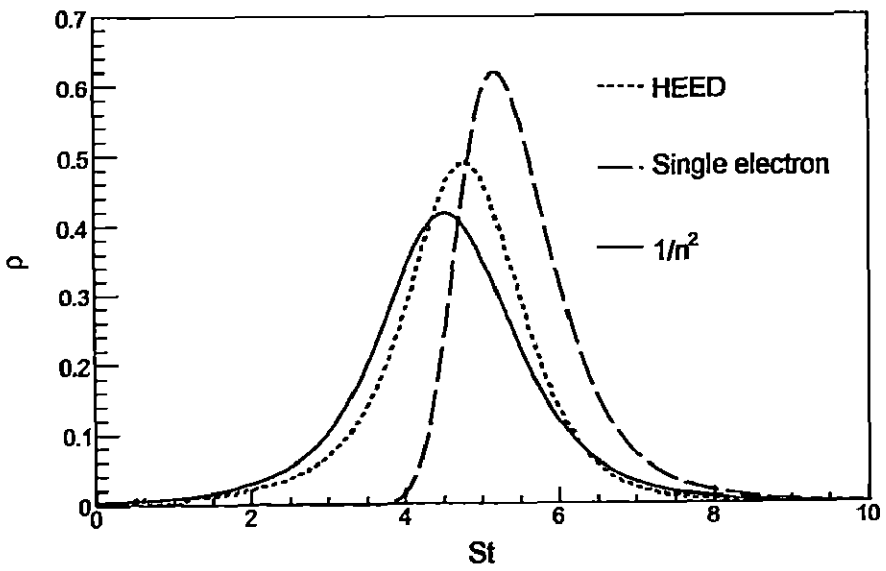

Figure 5.14: Time response function for HEED, $1/n^2$ and single electron cluster distributions for $k = 0$ and $n_0 = 5$ [81].

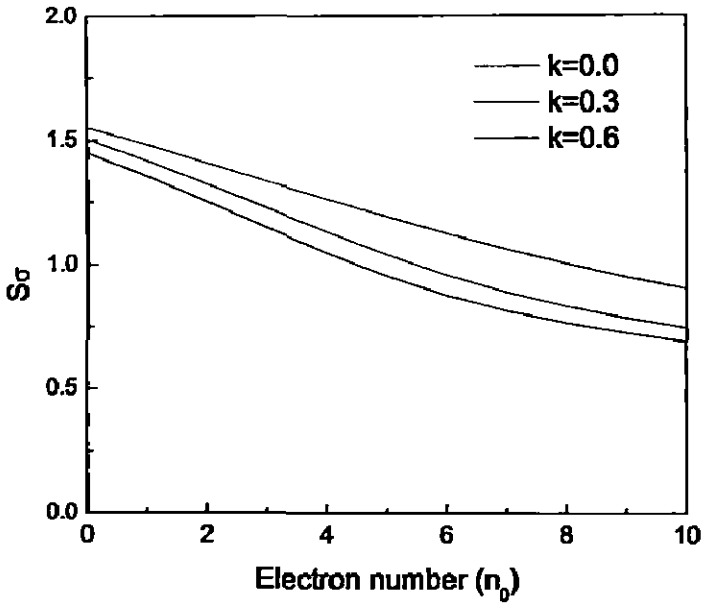

Figure 5.15: Time Resolution calculated using HEED cluster distributions for k = 0, k = 0.3 and k = 0.6 [81].

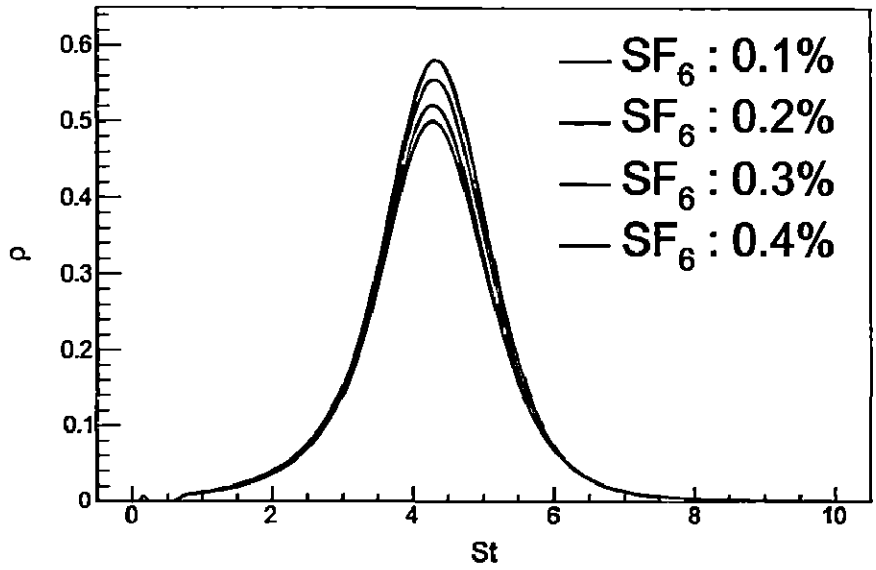

Figure 5.16: Time response function for different gas mixtures in 2 mm gap RPCs, n = 1000 and $n_0 = 5$.

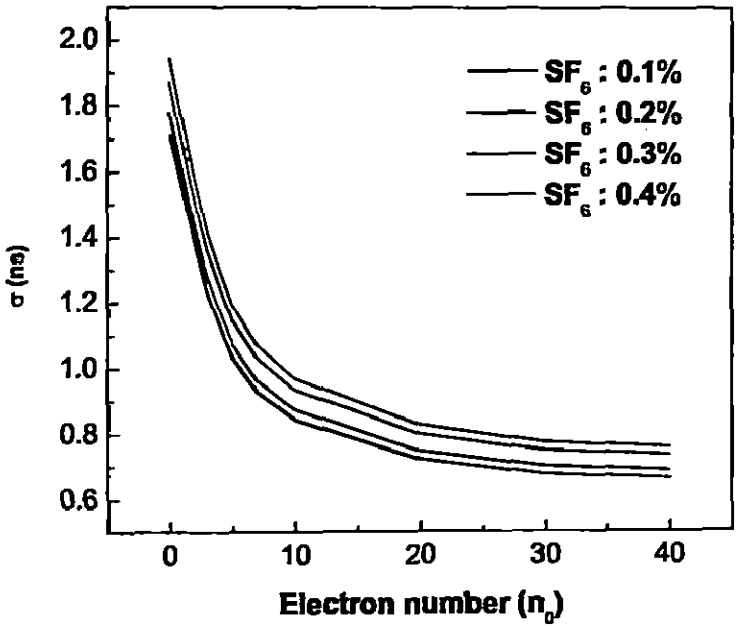

Figure 5.17: Time Resolution for different gas mixtures.

To validate our code, we reproduced the time response function for different cases (Fig. 5.14) and the time resolution for different values of k using the HEED cluster distributions (5.15) as calculated earlier by W. Reigler [81]. We have used the expressions for RPC time resolution given in references [80,81] to calculate the time resolution as a function of SF_6 percentage in the given gas mixture for a single electron and a realistic HEED cluster distribution. In Fig. 5.16, we show the time response function for different combinations of SF_6, calculated using our code. We can see that, the height of the time response function has inverse relationship with the SF_6 percentage in the gas mixture. This is because for low SF_6 percentage more electrons are available that grow into an avalanche and the probability of crossing the threshold in a given time interval is high. Adding more highly electronegative SF_6 to the gas mixture will quench the electrons produced in the gas gap and hence the probability of electrons to cross the threshold in a given time interval will be less. The variation of time resolution with the number of primary electrons for different concentrations of SF_6 is given in Fig.5.17. The figure shows that the time resolution become better with increase in the number of primary electrons and with increase in the SF_6 percentage the time resolution curve shifts to lower values. The simulated and experimental results are given in Fig. 5.18, Fig. 5.19 and Fig. 5.20. From these figures, it is clear that the simulated and experimental results follow the same trend.

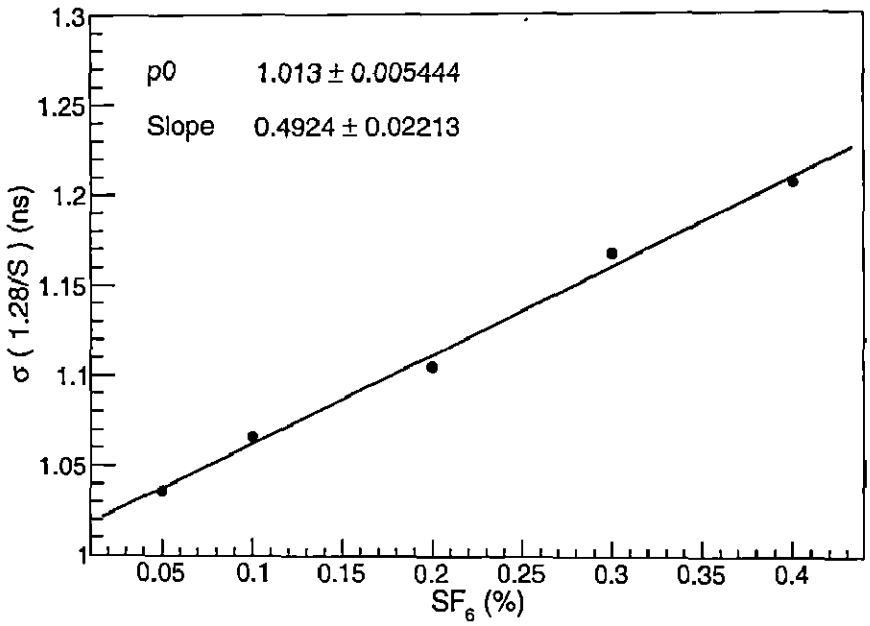

Figure 5.18: simulated time resolution for different SF_6 concentrations for a single electron.

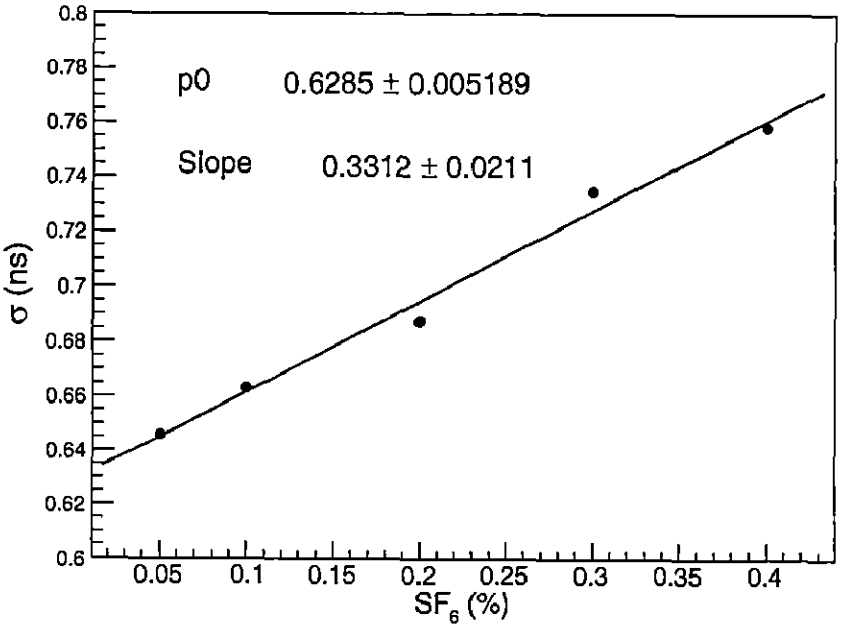

Figure 5.19: simulated time resolution for different SF_6 concentrations for HEED cluster distribution.

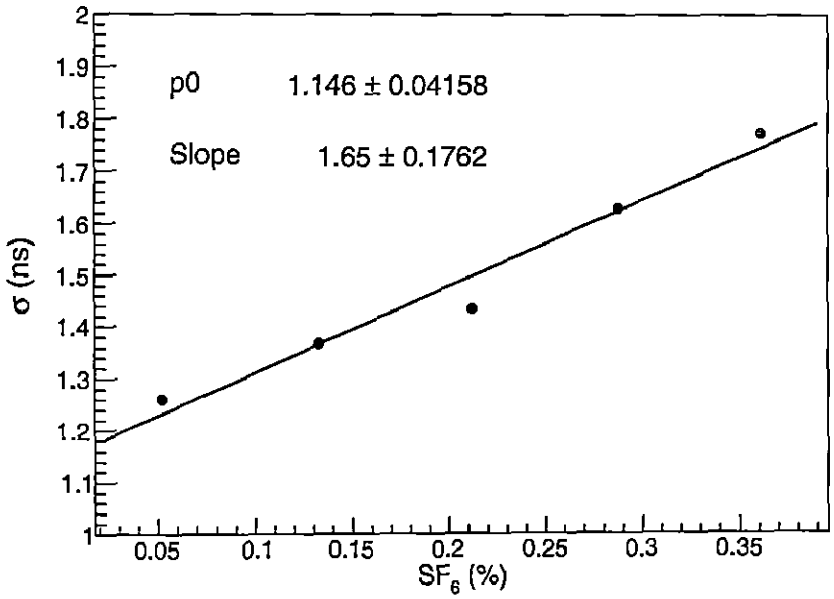

Figure 5.20: Experimental time resolution (present work) [33] for different SF_6 concentrations.

The time resolution becomes better with decreasing SF_6 concentration though the slopes of the simulated and experimental curves given in Figs.5.18, 5.19 and 5.20 are different. We can see from the experimental setup (Fig. 3.17) discussed in chapter 3, the stop signal to the TDC from the RPC is coming through preamplifier, FIFO and Front End Electronics (FEE). The pick-up strips, transmission cables and FEE all contribute to the time jitter of the timing signal. We observed an electronic time jitter of around 100 ps in our system. This might be the reason for the difference in the simulated and experimental results on time resolution, given in Figs.5.19 and 5.20.

5.6 Conclusion and future outlook

In this thesis, we have compared various RPC parameters like the efficiency, timing and the charge spectra measured for a 2 mm gap glass RPC operated in the avalanche mode with numerically simulated values. The timing studies of the RPC with the simulated and experimental data clearly indicate the effect of SF_6 in the RPC gas mixture where we can see that the time resolution becomes worse while increasing the SF_6 concentration in the gas mixture. From the experimental and simulated data of efficiency, we can see that the RPCs can be operated up to the knee of their efficiency plateau. Also the simulated efficiencies for different SF_6 concentrations show that the RPC with a gas mixture having higher SF_6 percentage needs comparatively

higher high voltage to reach the plateau region. This is due to the electronegative nature of SF_6 gas which attaches most of the electrons in the gas mixture and so the RPC requires higher voltage for creating avalanches and to make an event efficient. Our goal has been to study the effect of varying SF_6 concentration in a RPC gas mixture. Good agreement between the measured and simulated charge spectra has clearly indicate that the induced charge on the RPC pick-up electrodes decreases significantly with very small increase of SF_6 in the gas mixture. In Table 5.1, two sets of experimental measurements have been included. The statistics in the experimental data is low and different so two different sets of simulated spectra are used to compare these results. We plan to further improve the experimental setup and method, besides aiming for higher statistics for a better agreement between the experimental data and the simulated results. Since SF_6 is an expensive gas, the present study can help in optimizing the amount of SF_6 to be used in real experiments. The simulation that we carried out for the present work goes only upto signal induction on the pickup panels. It will be always nice to simulate the signal transmission on the strip, termination issues and electronics (particularly the preamplifier) response so that we will get a more realistic picture. Then the values can be better compared with the measurements. This can be made possible by extending the simulation study to circuit simulation. We are aiming to improve our study by incorporating the other physical effects of the detector and electronics in the RPC modeling by including the circuit simulation into the picture. We also plan to extend the study in order to encompass a reasonable parameter space that can help in identifying an optimum gas mixture. It is also expected that such a study will be able to explain the differences observed between the measured and simulated values in the present study.

BIBLIOGRAPHY

[1] E. Fermi **Zeit.f.Phys**, **88**, pp. 3161–177, 1934. 3

[2] F. Reines and C. Cowan, "Detection of the free neutrino," **Phys.Rev.**, **92**, pp. 830–831. 3

[3] F. Reines, C. Cowan, F. Harrison, A. McGuire, and H. Kruse, "Detection of the free anti-neutrino," **Phys.Rev.**, **117**, pp. 159–173. 3

[4] G. Danby, J. Gaillard, K. A. Goulianos, L. Lederman, N. B. Mistry, *et al.*, "Observation of High-Energy Neutrino Reactions and the Existence of Two Kinds of Neutrinos," **Phys.Rev.Lett.**, **9**, pp. 36–44. 3

[5] K. Kodama *et al.*, "Observation of tau neutrino interactions," **Phys.Lett.**, **B504**, pp. 218–224. 3

[6] J. N. Bahcall, "Solar models and solar neutrinos: Current status," **Phys.Scripta**, **T121**, pp. 46–50. 7

[7] J. N. Bahcall, A. M. Serenelli, and S. Basu, "New solar opacities, abundances, helioseismology, and neutrino fluxes," **Astrophys.J.**, **621**, pp. L85–L88. 7

[8] K. Scholberg, "Atmospheric neutrinos at Super-Kamiokande," 1999. vii, 7

[9] Z. Maki, M. Nakagawa, and S. Sakata, "Remarks on the unified model of elementary particles," **Prog.Theor.Phys.**, **28**, pp. 870–880. 8

[10] C. Giunti and K. C. Wook, **Fundamentals of Neutrino Physics and Astrophysics**. Oxford: Oxford Univ., 2007. 9

[11] F. An *et al.*, "Observation of electron-antineutrino disappearance at Daya Bay," **Phys.Rev.Lett.**, **108**, p. 171803. 12

[12] Majumdar2009719, "Observation of Reactor Electron Antineutrino Disappearance in the RENO Experiment," **Phys.Rev.Lett.**, **108**, p. 191802. 13

[13] Y. Abe *et al.*, "Indication for the disappearance of reactor electron antineutrinos in the Double Chooz experiment," **Phys.Rev.Lett.**, **108**, p. 131801. 13

[14] D. Forero, M. Tortola, and J. Valle, "Global status of neutrino oscillation parameters after Neutrino-2012," **Phys.Rev.**, **D86**, p. 073012. 13, 14

[15] "Detection of muons produced by cosmic ray neutrinos deep underground," **Physics Letters**, **18**, no. 2, pp. 196 – 199, 1965. 13

[16] **INO Collaboration.** Detailed Project Report I. vii, 13, 15

[17] T. Tabarelli de Fatis, "Prospects of measuring $\sin^2 2\theta_{13}$ and the sign of δm^2 with a massive magnetized detector for atmospheric neutrinos," **Eur.Phys.J.**, **C24**, pp. 43–50. 15

[18] S. Palomares-Ruiz and S. Petcov, "Three-neutrino oscillations of atmospheric neutrinos, θ_{13}, neutrino mass hierarchy and iron magnetized detectors," **Nucl.Phys.**, **B712**, pp. 392–410. 15

[19] D. Indumathi and M. Murthy, "A Question of hierarchy: Matter effects with atmospheric neutrinos and anti-neutrinos," **Phys.Rev.**, **D71**, p. 013001. 16

[20] B. Satyanarayana, **Design and Characterisation Studeies of Resistive Plate Chambers.** PhD thesis, Department of Physis, IIT Bombay, India, 2009. xi, 16, 17, 31, 36, 45, 60, 116

[21] R. Ferreira-Marques, J. Pinho, N. Carolino, A. Policarpo, and P. Fonte, "High Resolution RPCs for Large TOF Systems," 19

[22] S. Tavernier, **Experimental techniques in nuclear and particle physics.** Berlin: Springer, 2009. xi, 20, 29

[23] W. R. Leo, **Techniques for nuclear and particle physics experiments: a how-to approach; 2nd ed.** Berlin: Springer, 1994. 23, 24

[24] I. Smirnov, "Heed version 1.01: Detailed simulation of the initial ionization in gases," Mar 1997. 28, 105

[25] R. Santonico and R. Cardarelli, "DEVELOPMENT OF RESISTIVE PLATE COUNTERS," **Nucl.Instrum.Meth.**, **187**, pp. 377–380. 31

[26] Y. Pestov, "STATUS AND FUTURE DEVELOPMENTS OF SPARK COUNTERS WITH A LOCALIZED DISCHARGE. (TALK)," **Nucl.Instrum.Meth.**, **196**, pp. 45–47. 31

[27] Y. Pestov, "THE STATUS OF SPARK COUNTERS WITH A LOCALIZED DISCHARGE," **Nucl.Instrum.Meth. A**, **265**, pp. 150–156. 31

[28] C. Lippmann, R. Stock, and W. Riegler, **Detector Physics of Resistive Plate Chambers.** PhD thesis, Frankfurt U., Frankfurt, 2003. Presented on 01 Jul 2003. 33, 34

[29] P. Camarri, R. Cardarelli, A. Di Ciaccio, and R. Santonico, "Streamer suppression with SF_6 in RPCs operated in avalanche mode," **Nucl. Instr. and Meth. A, 414**, pp. 317–324. 35

[30] G. Aielli, P. Camarri, R. Cardarelli, A. Di Ciaccio, L. Di Stante, *et al.*, "SF-6 quenched gas mixtures for streamer mode operation of RPCs at very low voltages," **Nucl. Instr. and Meth. A, 493**, pp. 137–145. 35

[31] K. Abe, F. Handa, I. Higuchi, Y. Hoshi, N. Kawamura, *et al.*, "Performance of glass RPC operated in streamer mode with SF-6 gas mixture," **Nucl. Instr. and Meth. A, 455**, pp. 397–404. 35

[32] A. Behere, M. Bhatia, V. Chandratre, V. Datar, P. Mukhopadhyay, S. Jena, Y. Viyogi, S. Bhattacharya, S. Saha, S. Bhide, S. Kalmani, N. Mondal, P. Nagaraj, B. Nagesh, S. K. Rao, L. Reddy, M. Saraf, B. Satyanarayana, R. Shinde, S. Upadhya, P. Verma, S. Biswas, S. Chattopadhyay, and P. Sarma, "Ino prototype detector and data acquisition system," **Nucl. Instr. and Meth. A, 602**, no. 3, pp. 784 – 787, 2009. 37

[33] M. Bhuyan, V. Datar, S. Kalmani, S. Lahamge, S. Mohammed, N. Mondal, P. Nagaraj, A. Redij, D. Samuel, M. Saraf, B. Satyanarayana, R. Shinde, and P. Verma, "Development of 2m x 2m size glass rpcs for ino," **Nucl. Instr. and Meth. A, 661, Supplement 1**, no. 0, pp. S64 – S67, 2012. x, 37, 60, 124

[34] M. Bhuyan, V. Datar, S. Kalmani, S. Lahamge, N. Mondal, P. Nagaraj, S. Pal, L. Reddy, A. Redij, D. Samuel, M. Saraf, B. Satyanarayana, R. Shinde, and P. Verma, "Cosmic ray test of ino rpc stack," **Nucl. Instr. and Meth. A, 661, Supplement 1**, no. 0, pp. S68 – S72, 2012. 43

[35] M. Bhuyan, V. Chandratre, S. Dasgupta, V. Datar, S. Kalmani, S. Lahamge, N. Mondal, P. Nagaraj, S. Pal, S. Rao, A. Redij, D. Samuel, M. Saraf, B. Satyanarayana, R. Shinde, and S. Upadhya, "Vme-based data acquisition system for the india-based neutrino observatory prototype detector," **Nucl. Instr. and Meth. A, 661, Supplement 1**, no. 0, pp. S73 – S76, 2012. 45

[36] A. Behere, M. Bhuyan, V. Chandratre, S. Dasgupta, V. Datar, S. Kalmani, S. Lahamge, N. Mondal, P. Mukhopadhyay, P. Nagaraj, B. Nagesh, S. Pal, S. K. Rao, D. Samuel, M. Saraf, B. Satyanarayana, R. Shastrakar, R. Shinde, K. Sudheer, S. Upadhya, and P. Verma, "Electronics and data acquisition system for the ical prototype detector of india-based neutrino observatory," **Nucl. Instr. and Meth. A, 701**, no. 0, pp. 153 – 163, 2013. viii, 45

[37] CAEN, "V2718 technical information manual." `"http://www.caen.it/csite/"`. 47

[38] CAEN, "V830 technical information manual." `"http://www.caen.it/csite/"`. 47

[39] CAEN, "V1190a technical information manual." `"http://www.caen.it/csite/"`. 48

[40] G. Majumder, S. Mohammed, N. Mondal, S. Pal, D. Samuel, and B. Satyanarayana, "Velocity measurement of cosmic muons using the india-based neutrino observatory prototype detector," **Nucl. Instr. and Meth. A, 661, Supplement 1**, no. 0, pp. S77 – S81, 2012. 48

[41] CAEN, "V792 technical information manual." "http://www.caen.it/csite/". viii, 48

[42] S. Kalmani, N. Mondal, B. Satyanarayana, P. Verma, and A. Joshi, "On-line gas mixing and multi-channel distribution system," **Nucl. Instr. and Meth. A, 602**, no. 3, pp. 845 – 849, 2009. 49

[43] **Manufactured by M/s Tylan Corp., Torrance, CA, USA.** 52

[44] **http://en.wikipedia.org/wiki/Hagen-Poiseuille'equation.** 53

[45] **Manufactured by M/s Dow Corning, Valencia, CA, USA.** 53

[46] M. Salim, R. Hasan, N. Majumdar, S. Mukhopadhayay, and B. Satyanarayana, "Experimental and numerical studies on the effect of sf_6 in a glass rpc," **Journal of Instrumentation, 7**, no. 11, p. P11019. 59

[47] ROOT, "A data analysis framework." "http://root.cern.ch/drupal". 59

[48] T. Sjostrand, S. Mrenna, and P. Z. Skands, "PYTHIA 6.4 Physics and Manual," **JHEP, 0605**, p. 026. 63

[49] X.-N. Wang and M. Gyulassy, "HIJING: A Monte Carlo model for multiple jet production in p p, p A and A A collisions," **Phys.Rev., D44**, pp. 3501–3516. 63

[50] M. Gyulassy and X.-N. Wang, "HIJING 1.0: A Monte Carlo program for parton and particle production in high-energy hadronic and nuclear collisions," **Comput.Phys.Commun., 83**, p. 307. 63

[51] C. Andreopoulos, "The GENIE neutrino Monte Carlo generator," **Acta Phys.Polon., B40**, pp. 2461–2475, 2009. 63

[52] S. Agostinelli *et al.*, "GEANT4 A Simulation toolkit," **Nucl. Instr. and Meth. A, 506**, pp. 250–303. 63

[53] I. Smirnov, "Modeling of ionization produced by fast charged particles in gases," **Nucl. Instr. and Meth. A, 554**, no. 13, pp. 474 – 493, 2005. 64, 69, 73

[54] W. Allison and J. Cobb, "Relativistic Charged Particle Identification by Energy Loss," **Ann.Rev.Nucl.Part.Sci., 30**, pp. 253–298, 1980. 64, 65, 66, 69

[55] N. Majumdar and S. Mukhopadhyay, "Simulation of three-dimensional electrostatic field configuration in wire chambers: A novel approach," **Nucl. Instr. and Meth. A, 566**, no. 2, pp. 489 – 494, 2006. 64, 82, 83

[56] N. Majumdar, S. Mukhopadhyay, and S. Bhattacharya, "Computation of 3d electrostatic weighting field in resistive plate chambers," **Nucl. Instr. and Meth. A, 595**, no. 2, pp. 346 – 352, 2008. 64, 82, 83

[57] N. Majumdar, S. Mukhopadhyay, and S. Bhattacharya, "Three-dimensional electrostatic field simulation of a resistive plate chamber," **Nucl. Instr. and Meth. A, 602**, no. 3, pp. 719 – 722, 2009. 105

[58] S. Biagi, "Monte carlo simulation of electron drift and diffusion in counting gases under the influence of electric and magnetic fields," **Nucl. Instr. and Meth. A, 421**, no. 12, pp. 234 – 240, 1999. 64, 96, 97, 98

[59] W. Blum, W. Riegler, and L. Rolandi, **Particle Detection with drift Chambers; 2nd ed.** Berlin: Springer, 2008. 64, 67, 68, 94, 95

[60] L. D. Landau, **Electrodynamics of continuous media.** Oxford England: Butterworth-Heinemann, 1984. 64

[61] H. Schindler and C. Fabjan, **Microscopic Simulation of Particle Detectors.** PhD thesis, Vienna, Tech. U., 2012. Presented 13 Dec 2012. 65

[62] Photoabsorption-database. "http://dpc.nifs.ac.jp/photoab/d_list.html". viii, 69

[63] S. A. et.al, "Geant4a simulation toolkit," **Nucl. Instr. and Meth. A, 506**, no. 3, pp. 250 – 303, 2003. 70

[64] Geant4, "Geant4 user's documents: Introduction to geant4." "http://geant4.web.cern.ch/geant4/support/introductionToGeant4.shtml/". 70

[65] Geant4. "https://twiki.cern.ch/twiki/bin/view/Geant4/". 72

[66] J. Bar, J. Sempau, J. Fernndez-Varea, and F. Salvat, "Penelope: An algorithm for monte carlo simulation of the penetration and energy loss of electrons and positrons in matter," **Nucl. Instr. and Meth. B: Beam Interactions with Materials and Atoms, 100**, no. 1, pp. 31 – 46, 1995. 72

[67] J. Sempau, J. Fernndez-Varea, E. Acosta, and F. Salvat, "Experimental benchmarks of the monte carlo code penelope," **Nucl. Instr. and Meth. B: Beam Interactions with Materials and Atoms, 207**, no. 2, pp. 107 – 123, 2003. 72

[68] **http://geant4.web.cern.ch/geant4/UserDocumentation/UsersGuides, 118-121.** 73

[69] T. Heubrandtner, B. Schnizer, and H. Schpf, "A simple theory for signals induced by a point charge moving in a resistive plate chamber," **Nucl. Instr. and Meth. A, 419**, no. 23, pp. 721 – 725, 1998. 78

[70] "Comsol multiphysics." "http://www.comsol.co.in/". 85

[71] G. C. G. Schultz and F. Sauli, "Mobilities of positive ions in some gas mixtures used in proportional and drift chambers," **Rev. Phys. Appl. (France), 12**, p. 67. xi, 96

[72] G. Fraser and E. Mathieson, "Monte carlo calculation of electron transport coefficients in counting gas mixtures: I. argon-methane mixtures," **Nucl. Instr. and Meth. A, 247**, no. 3, pp. 544 – 565, 1986. 97

[73] S. Longo and M. Capitelli, "A simple approach to treat anisotropic elastic collisions in monte carlo calculations of the electron energy distribution function in cold plasmas," **Plasma Chemistry and Plasma Processing, 14**, no. 1, pp. 1–13, 1994. 97

[74] H. R. Skullerud, "The stochastic computer simulation of ion motion in a gas subjected to a constant electric field," **Journal of Physics D: Applied Physics, 1**, no. 11, p. 1567. 97

[75] S. Biagi, "Magobltz, program to compute electron transport parameters." "http://magboltz.web.cern.ch/magboltz/". 98, 105

[76] M. Abbrescia *et al.*, "The simulation of resistive plate chambers in avalanche mode: charge spectra and efficiency," **Nucl. Instr. and Meth. A, 431**. 109

[77] S. Ahn *et al.*, "Perfomance and simulation of a double-gap resistive plate chamber in the avalanche mode," **J. Korean Phys. Soc., 45**. 109

[78] H. Genz, "Single electron detection in proportional gas counters," **Nucl. Instr. and Meth. A, 112**. 110

[79] S. Ramo, "Currents induced by electron motion," **Proceedings of IRE, 27**. 110

[80] W. Riegler, C. Lippmann, and R. Veenhof, "Detector physics and simulation of resistive plate chambers," **Nucl. Instr. and Meth. A, 500**, no. 13, pp. 144 – 162, 2003. 115, 122

[81] W. Riegler, "Time response functions and avalanche fluctuations in resistive plate chambers," **Nucl. Instr. and Meth. A, 602**, no. 2, pp. 377 – 390, 2009. x, 118, 119, 120, 121, 122